Development of steel-concrete interface model for structural elements

Can Turgut

Université Paris Nanterre

200 av. de la République
92001 Nanterre Cedex
www.parisnanterre.fr

Membre de l'université Paris Lumières
Membre de l'université Paris Lumières

École doctorale 139 :
Connaissance, langage, modélisation
Laboratoire Energétique Mécanique Electromagnétisme

Can TURGUT

Prise en compte de la liaison acier béton dans le comportement d'éléments de structure en béton armé

Thèse présentée et soutenue publiquement le ***14/12/2018***
en vue de l'obtention du doctorat de Mécanique, Génie Mécanique, Génie Civil de l'Université Paris Nanterre
sous la direction de
M. Luc DAVENNE (Professeur des Universités, Université Paris Nanterre)
et de M. Ludovic JASON (Ingénieur de recherche, HDR, CEA)

Jury :

Rapporteur :	Mme Géraldine CASAUX-GINESTET	Maître de Conférences HDR, INSA de Toulouse
Rapporteur :	M. Panagiotis KOTRONIS	Professeur des Universités, Ecole Centrale de Nantes
Président :	Frédéric RAGUENEAU	Professeur des Universités, ENS Paris Saclay
Membre du jury :	Christophe FOND	Professeur des Universités, Université de Strasbourg

This book is cordially and sincerely dedicated to

my aunt Fatma Şükran TURGUT

who was a great source of inspiration and motivation.

Acknowledgement

I would like to extend my sincere gratitude and cordial thanks to Mr. Alex PIRARD and Mr. Anthony MERLET for all their gracious support and follow-up during my PhD period.

I also would like to declare my deeply grateful thanks to ENGIE Company and CEA Saclay Research Center for giving me the opportunity to achieve my PhD degree in France.

I would like to address my deepest and most special thanks to my doctoral supervisor, Pr. Luc DAVENNE and likewise my co-adviser Dr.HDR Ludovic JASON for their patient guidance, encouragement, stimulating discussions and invaluable advices that they have provided during my PhD period in every aspect. I must also confess that, working and interacting with these erudite people, and even alone observing them, expanded not only my knowledge but also my perspective of life. It was a real pleasure and course of life for me to endeavor with them.

I also would like to express my greatest appreciation to all the jury members, Dr.HDR Géraldine CASAUX-GINESTET, Pr. Panagiotis KOTRONIS, Pr. Frédéric RAGUENEAU and Pr. Christophe FOND for their valuable time, patience and evaluation of my PhD thesis.

I want to convey in addition my deepest thanks and gratitude to our chef of the laboratory from LM2S/CEA, Dr. Serge PASCAL, for all his favor and support in every respect during my PhD, his understanding, his guidance, his attention, valuable advices and follow-up during the PhD process. Thank you so much.

I would like to thank Dr. François DI PAOLA for teaching and helping me all about the finite element coding. Additionally, I would like to thank him once again for taking time of his busy schedule to listen me patiently and answer all my questions, proposing wise solutions every time I consulted him.

I am also thankful to all LM2S Laboratory members in CEA. I spent most of my time among them during my PhD and every moment was a good opportunity for me to learn new things, broaden my knowledge and evolve myself.

I would like to thank sincerely to my dear friend Nuri BEYDOĞAN to take his valuable time to comfort me in my hard times during my PhD and his valuable advices and ideas about the template and the format of a proper thesis.

I would also like to place on the record, my sense of gratitude to one and all, who directly or indirectly, have lent their hand in this venture.

I would specifically place my gratitude and love to my father Mehmet for all his continuous support, his encouragement, his valuable advices and unconditional love throughout my life. Without your guidance in my life, I would have been lost.

Finally, my deepest gratitude to my caring, loving and supportive family: my mother Zühal, my grandmother Naciye, my little brother Oğuz and my fiancé Ayşegül. It was a great comfort and relief to know that you are always there for me. Particularly, I am not able to express my indebtedness to my lovely aunt Fatma, whom raised me and made me what I am today. This thesis is dedicated to you!

Abstract

In numerical applications of reinforced concrete structures, the steel-concrete interface behavior has a vital importance when the cracking properties are investigated. A finite element approach for the steel-concrete interface to be used in large-scale simulations was proposed by (Torre-Casanova 2013) and (Mang 2016). It enables to calculate the slip between the steel and concrete in the tangential direction of the interface element representation. The aim is here to improve the initial bond-slip model to be more efficient and more representative.

The document is divided into three parts:

- **The existing bond-slip model is evaluated**. The bond-slip model is then improved by considering transversal and irreversible bond behaviors under alternative loads. The new bond-slip model is validated with several numerical applications.
- **Confinement effect is implemented in the bond-slip model** to capture the effect of external lateral pressure. According to the performed numerical applications, it is demonstrated how the active confinement can play a role, through the steel-concrete bond, during monotonic and cyclic loading cases
- **Dowel action is finally investigated with the new bond-slip model.** Two different experimental campaigns (Push-off tests and four-point bending tests) are reproduced with different reinforcement (1D truss and beam) and interface (new bonds-slip and perfect bond) models. The results show that the proposed simulation strategy including the bond slip model enables to reproduce experimental results by predicting global (force-displacement relation) and local behaviors (crack properties) of the reinforced concrete structures under shear loading better than the perfect bond assumption which is commonly used in the industrial applications.

Keywords: Steel-concrete interface, bond-slip model, irreversible bond behavior, active confinement effect on the bond, dowel action.

Résumé

Le comportement de l'interface acier-béton a une grande importance lorsque la fissuration des structures en béton armé est étudiée. Une approche par éléments finis a été proposée par (Torre-Casanova 2013) et (Mang 2016) pour représenter l'interface acier-béton dans les simulations de structures à grandes dimensions Le modèle proposé permet de calculer le glissement tangentiel entre l'acier et le béton. L'objectif de cette étude est d'améliorer ce modèle initial pour le rendre plus efficace et plus représentatif.

Le document est découpé en trois parties :

- **Le modèle initial de liaison est évalué.** Puis amélioré tant en chargement monotone qu'alterné. Le nouveau modèle est validé par plusieurs applications numériques.
- **L'effet de confinement est implémenté dans le modèle de liaison acier-béton.** L'effet sur le comportement structural du confinement actif est étudié en utilisant le nouveau modèle. A partir des simulations proposées, il est montré, par l'utilisation du nouveau modèle, que l'effet de confinement actif peut jouer un rôle sur les comportements monotones que cyclique.
- **L'effet goujon est étudié avec le nouveau modèle liaison acier-béton.** Deux campagnes expérimentales différentes sont simulées avec différents modelés de renforts (1D barre et poutre) et d'interface (liaison acier-béton et liaison parfaite). Les résultats montrent que le nouveau modèle de liaison acier-béton permet de mieux reproduire les résultats expérimentaux par rapport au modèle de liaison parfaite aux échelles globale et locale.

Mots clé : Liaison acier-béton, comportement de liaison irréversible, confinement actif, effet goujon.

Table of Contents

List of Figures

List of Tables

Introduction

Reinforced concrete is a composite material made of concrete and steel. The applications of reinforced concrete structures are very variable, for example beams, bridges, walls, pillars, nuclear power plant containment buildings etc. Steel and concrete have very different properties, implying a particularly complex behavior for reinforced concrete. Concrete has a high compressive strength and a low tensile strength. Cracking generally occurs in a reinforced concrete structure when the tensile limit is exceeded in concrete. In many civil engineering applications, steel is used to compensate the low tensile strength of the concrete. The combination of these two materials creates a resistant structure which can be used in very varying construction branches. Yet they are complex materials and require detailed consideration. Under the certain amount of loading, the cracks may initiate in the form of micro cracks and then propagate. If the loading reaches a certain limit, macro cracks can appear and develop until the structure breaks. The stress transfer between these two materials is extremely important to analyze cracking behavior which may lead the structural failure. The stress transfer between steel and concrete occurs through the interface between them. For example, when a crack occurs, the stresses on the surrounding concrete becomes zero and the load is completely taken by the steel at the crack location. Then, the forces are gradually transferred from the steel to the concrete. This transfer zone has a significant impact on the characterization of cracking and is directly influenced by the characteristics of the steel-concrete interface. Taking into account the steel-concrete interface characteristics is therefore a key element for a correct prediction of cracking in reinforced concrete structures.

In industrial numerical applications, the most commonly used approach is the perfect bond model which is based on the same displacement between the steel and concrete. However, this perfect bond hypothesis doesn’t consider the complex phenomena at the steel-concrete interface like significant disorders, repartition, propagation and the distribution of the cracks, which is directly related to the steel-concrete interface. In literature, several numerical methods ((Ngo and Scordelis 1967), (Reinhardt, Blaauwendraad and Vos 1984), (Clément 1987) etc.) are proposed in order to define concrete-steel bond behavior, but unfortunately these methods have many difficulties in computation of complex structures in 3D especially when large scale industrial applications are considered.

(Torre-Casanova 2013) and (Mang 2016) proposed an alternative approach for the simulation of the steel-concrete bond behavior which was adapted for large scale simulations. Taking into account mechanical interactions between concrete (generally in 3D) and steel reinforcement (represented by 1D elements), this model improves the cracking description during the active cracking phase (beginning of crack apparition) and influences the local behavior of the structure especially around the steel reinforcement. A new finite element was subsequently developed and implemented in the finite element code (Cast3M 2017) focusing on the tangential behavior of the bond.

Motivation of the research

The behavior of reinforced concrete structures can be extremely complex in the case of representing cracking process numerically. The composite characteristics of reinforced concrete structure should be finely presented especially at the steel-concrete interface. A consideration of a proper methodology for the steel-concrete interface is thus necessary for the industrial applications where the crack properties are highly significant. It is especially the case for structures in which the tightness is a key functionality, as the potential leakage rate is a direct function of the crack properties.

Objectives

The main objective of this research is to develop further the methodology that has been previously developed to be applied on industrial structures with an acceptable computational cost and representative of the bond-slip mechanisms. The general objectives of the study can be summarized as following:

- Dowel action is one of the shear stress transfer mechanisms in reinforced concrete structures which occurs at the crack location. The investigation of this phenomena with the bond-slip may be useful since the proposed model represents the cracking behavior in a detailed way. In order to do so, initially, the normal directional behavior of the bond-slip model should be investigated. The proper validation of the model in normal and tangential directions are thus necessary.
- Irreversible behavior of the bond is implemented in the bond-slip model and tested with limited number of applications by (Mang 2016). Yet, the application of irreversible

bond-slip model on different types of numerical tests is necessary for the complete validation of the model.

- In literature, several authors like (Hadi 2008), (Karatas, Turk and Ulucan 2010), (Yang, et al. 2015) etc. have pointed out the importance of the active and passive confinement on the steel-concrete bond properties by some experimental and numerical studies. In addition, the active and passive confinement effect on the bond strength is investigated by (Torre-Casanova, Jason, et al. 2013) with an experimental campaign. The authors (Torre-Casanova, Jason, et al. 2013) have proposed empirical formulations to determine the splitting to pull-out failure (passive confinement effect on the bond strength). Investigation of external pressure effect (active confinement) on the bond is thus necessary to conclude this study.
- In order to understand the significance of the bond-slip model to represent the dowel action numerically, a proper comparison is also necessary with other bond models (like perfect bond hypothesis) by reproducing different experimental campaigns. However, before performing these kinds of analysis, the proper models for steel and concrete should be investigated carefully to represent shear behavior of the reinforced concrete structures.

Based on the objectives presented above, the general consents of this thesis are established.

Methodology

This study can be summarized under four major topics:

First chapter is dedicated to the state of the art. The steel-concrete interaction in reinforced concrete structures is generally explained and the importance of an interfacial behavior for the crack properties is expressed. Then, numerical representation of the steel-concrete bond is presented by defining several existing numerical models. A background information is provided on the monotonic and cyclic bond behaviors. Then, the confinement influence on the steel-concrete bond is briefly clarified for different confinement types. Eventually, dowel action and its importance to the shear resistance is explained.

Second chapter is dedicated to the introduction and evaluation of the existing bond-slip model. Firstly, detected anomalies are presented, then the adapted new methodologies are explained

to overcome the presented anomalies. Afterwards, several numerical tests are detailed to evaluate the adopted methodologies.

The third chapter is dedicated to the implementation of the confinement effect inside the bond-slip model. Initially, the proposed formulas are described to consider the confinement effect within the bond properties. Then, the implementation of the confinement effect to the bond-slip model is explained in details. The implementation is validated by reproducing several experimental pull-out campaigns. Again, the effect of active confinement is investigated with the new bond-slip model on a tie-rod under different type of loads (monotonic and cyclic).

The fourth chapter is dedicated to the investigation of the dowel action in reinforced concrete structures with the new bond-slip model. In order to represent the shear behavior, two different experimental campaigns (push-off tests and bending tests) are reproduced by different bond and reinforcement models.

Chapter-1:
State of the Art

1. Introduction

This study aims to improve the integration of the steel-concrete bond for modeling reinforced concrete structures. In the context, existing bond-slip model (Casanova, Jason and Davenne 2012) is firstly investigated and then improved by considering different phenomenon like transversal and irreversible bond behavior, dowel action, confinement effect, etc. This Chapter is created to give a background information about the whole study before going into the details of the implementation and the analysis related with the bond-slip model.

This Chapter highlights a general information mainly in four areas:

- Steel-concrete interaction: the importance and effect of steel-concrete interface in the numerical applications and its characterization are explained.
- Numerical representation of the steel-concrete bond: several existing interface models in literature are explained specifically focusing on the bond-slip behavior.
- Steel-concrete bond law: monotonic and irreversible (under cyclic loadings) bond behavior of the steel-concrete bond are exposed. Moreover, active and passive confinement effect and their influence on the steel-concrete bond behavior are explained in detail.
- Dowel action: the shear transfer in reinforced concrete structures is explored mainly by focusing on the dowel action phenomenon. Characterization, analytical and numerical representation of the dowel action are explained in a detailed way.

2. Steel-Concrete Interface

Reinforced concrete structures formed of steel and concrete make a great combination to resist loading. The tension load acting on reinforced concrete structure is mainly taken up by reinforcement inside the concrete while the compression load is absorbed by the concrete itself, which provides the strength. Nowadays, these types of combinations are widely used in

construction industry. Since both materials have very different features from each other, understanding of their interaction is quite essential to analyze the behavior of the reinforced concrete structures, especially when the cracking properties are concerned for investigation.

2.1. Role of Steel-Concrete Bond

Bond behavior is important to take into account as cracking behavior in reinforced concrete structures (number, initiation, location, propagation etc.) is generally influenced by the stress distribution along the interface between steel and concrete. A structural element composed of an embedded reinforced bar in a concrete block is considered by (Torre-Casanova 2013) in order to illustrate the bond behavior. Figure 1.1 represents the reinforced structure on which displacement is imposed at the ends of the reinforcement. The only force applied on the concrete block is transferred by the steel bar. Therefore, only the interface between concrete and steel is responsible for the loading of concrete and therefor for the initiation and propagation of the cracks.

Figure 1.1 Principles of the tie-beam test (Torre-Casanova 2013).

When the load is applied at both ends of the steel bar, the stress is firstly transferred from steel through the interface to concrete and then distributed between them. This is mainly the reason for the stress free concrete ends since the load (or displacement) is applied on the steel bar. In the initial state where cracks are not yet observed (un-crack state), which is presented in Figure 1.2a, the stress along the steel and the concrete is homogenously distributed between the points A and B until the stress increases up to the concrete tensile strength. When the stress reaches the concrete tensile strength, a first crack occurrence is observed in the concrete. At the exact crack location, the applied load passes only through the steel and gradually transfers to concrete at both sides of the crack (Figure 1.2b). If the load applied on the steel increases, a second crack occurs at in the concrete. While the applied load keeps on increasing, this process repeats itself at different locations in the concrete. This phase is called cracking stage. When the distances between the cracks are too small to allow the concrete to reach its tensile strength again, there can no longer be cracks. This final part is called stabilized cracking phase (Figure 1.2c). At this

stage the majority of the forces are compensating by the steel bar itself. The value e_{min} represents the minimum distance between the two successive cracks and can be given for example by the following Eq. 1.1 (Eurocode 2 2007):

$$e_{min} = \frac{d_s S_c f_t}{4 S_s \tau_u} \tag{1.1}$$

where, d_s is the diameter of the steel bar, f_t is the tensile strength of the concrete, τ_u is the ultimate bond strength, S_s and S_c are the cross sections of steel and concrete respectively.

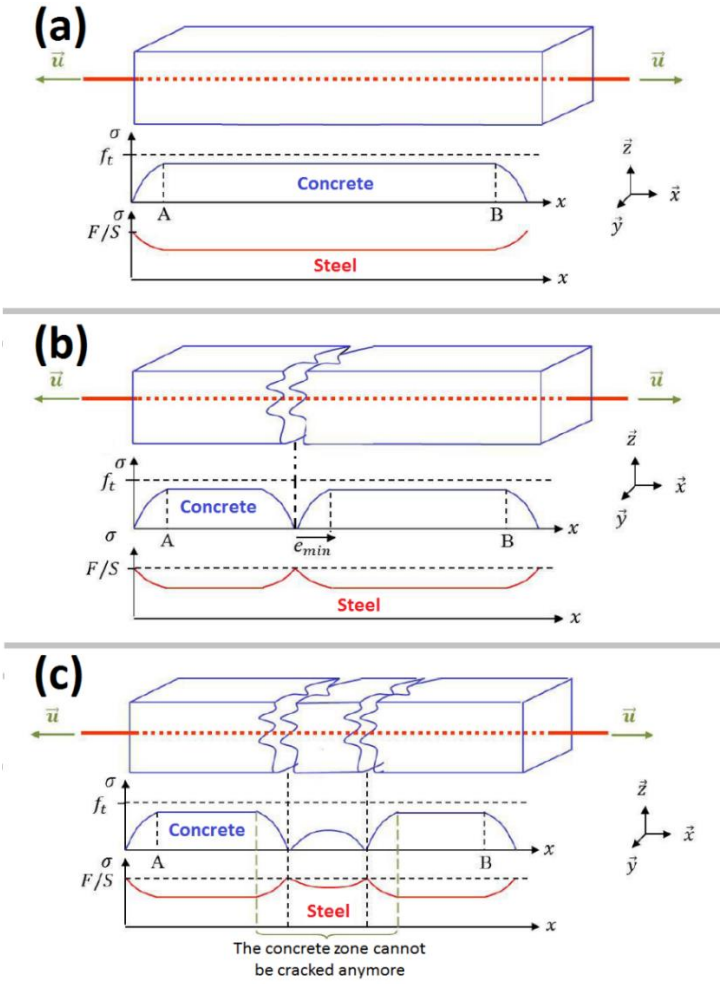

Figure 1.2 Stress distribution in the steel and concrete during (a) un-cracked phase, (b) cracking phase, (c) stable cracking phase (Torre-Casanova 2013).

All the phases explained above are governed by the interactions between the steel and concrete along the interface. As a conclusion, the cracking properties (number, initiation, location, propagation etc.) in reinforced concrete materials not only depends on the geometric and material properties of the steel and concrete, but also depend on the bonding properties between them.

2.2. Characterization of Steel-Concrete Bond

The most commonly adopted test to examine the bond strength of reinforced concrete structures in detail is the pull-out test. One of the first studies on the steel-concrete bond behavior is performed by (Abrams 1913) whom performed about 1500 pull-out tests in displacement control on different test specimens (Figure 1.3). Later on, many different pull-out tests are performed by several authors (e.g. (Slater, Richart and Scofield 1920), (Morita and Kaku 1974), (Eligehausen, Popov and Bertero 1983)) in order to determine the bond stress-bond slip relation in reinforced concrete materials.

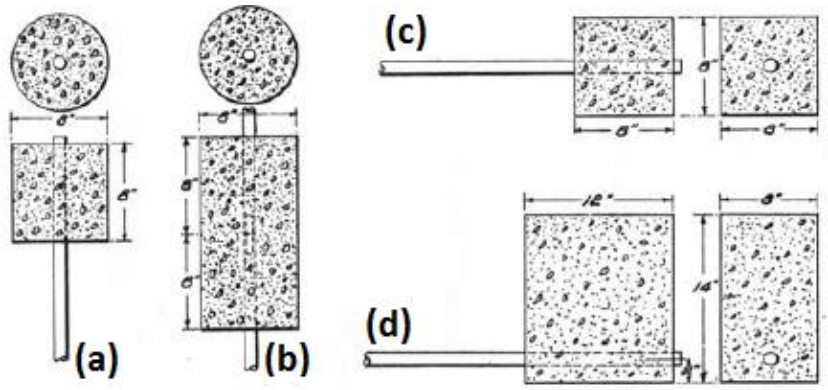

Figure 1.3 Different types of pull-out specimens (Abrams 1913).

The bond stress τ can be easily determined by dividing the force by the area of the steel bar embedded inside the concrete as in the Eq. 1.2 (Hadi 2008):

$$\tau = \frac{A_s \Delta f_s}{\pi d_s x} = \frac{d_s \Delta f_s}{4x} \qquad (1.2)$$

where τ is the bond stress along the length x, Δf_s is the variation of normal stress in the steel bar for the length x, A_s is the cross section and d_s is the diameter of reinforcement.

This formulation can be simplified with uniform stress distribution assumption along the steel bar written as following (Torre-Casanova, Jason, et al. 2013), (Sulaiman, Ma, et al. 2017):

$$\tau = \frac{F}{\pi d_s L_d} \qquad (1.3)$$

where F is the force applied on the reinforcement and L_d is the embedment length of the steel bar.

Based on the pull-out test and obtained stress-slip curves, three main types of load transfer mechanisms are detected between the steel and concrete cover according to the authors like (Tepfers 1973), (Park and Paulay 1975), (Eligehausen, Popov and Bertero 1983) etc. (Figure 1.4). These are

- Adhesion,
- Micro-interlocking,
- Friction.

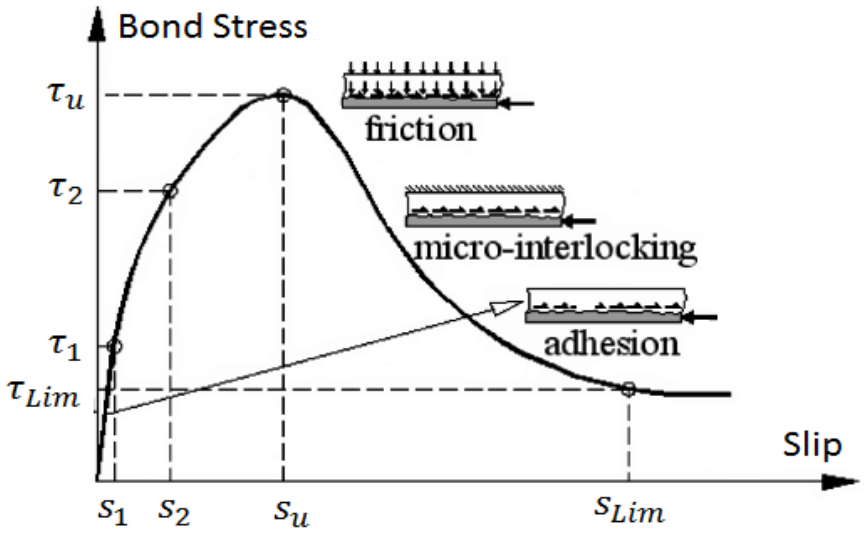

Figure 1.4 Stress vs. slip behavior and idealized shear transfer mechanism in steel-concrete interface (De Nardin and El Debs 2007).

Adhesive resistance (adhesion) is the bonding constrains between the steel and concrete due to the chemical nature of the materials and static friction which develops before the relative movement begins between the two materials. This chemical bond is presented in the first part of the bond-slip curve which is presented between 0 and τ_1 in Figure 1.4. The peak load of this region (τ_1) depends mainly on the steel bar's surface quality (De Nardin and El Debs 2007). The chemical adhesion is active mainly at early stages of the loading and corresponds only a small part of the bond strength (Johansson 2003).

Micro-interlocking mechanism between steel and concrete takes part after chemical adhesion due to increasing load and depends on mechanical characteristics of the interface. These mechanical characteristics of the steel and surrounding concrete due to the steel geometry, steel surface irregularities, concrete properties and concrete surface roughness may cause resistance against the applied load which increases the bond strength. (Tepfers 1973), (Morita and Kaku 1974), (Park and Paulay 1975) etc. indicate that this mechanism has an important effect only if the ribbed reinforcement is considered. Micro-interlocking is considered mainly between the regions s_1 and s_{lim} in Figure 1.4. However, the concrete cover prevents the total separation

between steel bar and concrete with the occurrence of normal stresses which may resist slip, it is rather difficult the separate the micro-cracking and pure friction mechanisms during the loading process (De Nardin and El Debs 2007).

Friction mechanism occurs as soon as relative movement between two materials (steel and concrete) take place. The friction is due normal stresses that develop between steel and concrete and depends on the surface properties of steel and covering concrete. The pure friction between steel and concrete takes part after s_{lim} according to Figure 1.4. This phase is often referred as macro-cracking phase (De Nardin and El Debs 2007).

3. Numerical Representation of the Steel-Concrete Bond

In industrial numerical applications, the perfect bond assumption is commonly used since it is easily applicable to large scale simulations. In these simulations, the steel nodes and the surrounding concrete nodes have the same displacement. This can be implemented in two manners: merged concrete and steel coincident nodes, or kinematic relations which relate the steel displacements to the concrete displacements. In the latter case the meshing is easier since the steel nodes don't need to coincide with concrete nodes, but the number of equations is increased and the computation time can be increased significantly.

The perfect bond assumption though gives relevant results especially in strong bond conditions between steel and concrete such as pre-stressed ribbed bars. On the other hand, for poor bonding conditions between two materials (steel and concrete) or complicated loading scenarios such as cyclic loading, it is necessary to define an interface model in order to perform proper analysis (Grassl, Johansson and Leppanen 2018). Thus, cracking in reinforced concrete structures is generally influenced by the stress distribution along the interface between steel and concrete. Stress transfer between these two materials directly affects the crack width, crack spacing and stress distribution in reinforced concrete members. The bond between concrete and steel bar has a vital importance for the performance and durability of reinforced concrete structures (Lin, et al. 2017). For this reason, profound consideration of steel-concrete interface is essential to predict the cracking in reinforced concrete structures. In this section numerical models for steel-concrete interface are described briefly.

3.1. Spring elements

Within the framework of the finite element method, researchers have developed several different approaches for defining the steel-concrete interface. One of the first approaches is the representation of 2D spring elements by (Ngo and Scordelis 1967) which connects steel and concrete nodes by spring elements that have constant stiffness (Figure 1.5a). Since constant stiffness values are defined for the spring elements, the model assumed total elasticity for the steel-concrete bond.

After, some researcher introduced an irreversible slip behavior for spring elements (Gan 2000). For a similar application, the Fiber Reinforcement Polymer, (Fawzia, Zhao and Al-Mahaidi 2010) and (Dehghani, et al. 2012) used also spring elements and suggested bilinear or trilinear models in order to represent both elastic and plastic parts of the bond-slip curve (Figure 1.5b). Afterwards, (He and Xian 2017) proposed the use of spring elements in 3D applications, and a simplified form of trilinear curve by using exponential functions (Figure 1.5c).

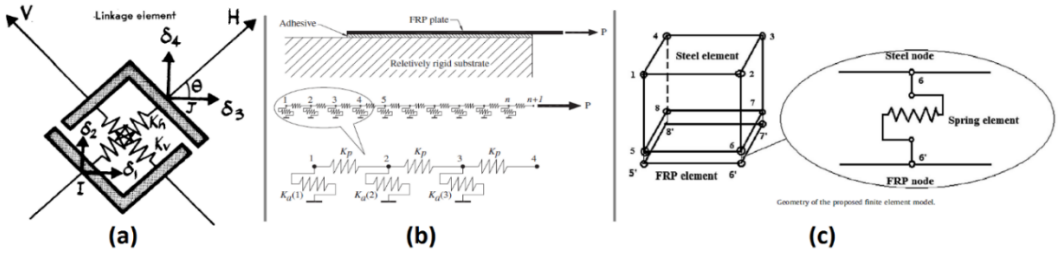

Figure 1.5 Representation of spring element: (a) (Ngo and Scordelis 1967), (b) (Dehghani, et al. 2012), (c) (He and Xian 2017).

3.2. Finite elements for an interface zone

Instead of spring elements, (Reinhardt, Blaauwendraad and Vos 1984) proposed to model an interface zone (a slip layer section) with 2D elements to calculate the slip between steel and the outer concrete (Figure 1.6a). They introduced Mohr-Columbus kind of laws. Afterwards, 2D and 3D finite volume bond elements and multidimensional interface constitutive models have been proposed. Among those (Lundgren 2002) developed an interface element based on total plasticity which can fulfill 3D features (Figure 1.6b). Afterwards, (Jendele and Cervenka 2006) proposed a simplified version of Lundgren's model with rather low computational cost. Then, (Santos and Henriques 2015) suggested an alternative interface element model which represents elastoplastic behavior of the bond by considering steel bar diameter and concrete strength (Figure 1.6c).

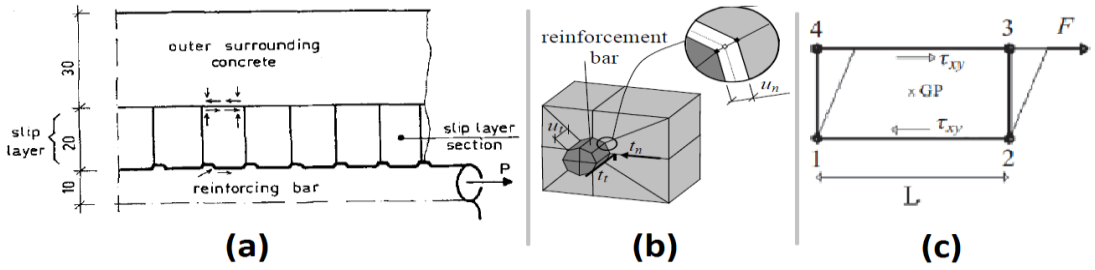

Figure 1.6 Representation of interface element: (a) (Reinhardt, Blaauwendraad and Vos 1984), (b) (Lundgren 2002), (c) (Santos and Henriques 2015).

3.3. Joint elements

Another common representation of steel-concrete bond is the joint elements which are firstly proposed by (Clément 1987) by introduction of zero thickness interface element in 2D (Figure 1.7a). Since the joint element has no physical dimensions, the two connected nodes originally occupy the exact location in the finite element representation of un-deformed structure. Based on that, different types of joint elements are suggested in literature like (Daoud 2003), (Brisotto, Bittencourt and Bessa 2012), (Sanz and Planas 2018), etc. and used to analyze reinforced concrete structures (Figure 1.7b and 1.7c). For example, (Lowes, Moehle and Govindjee 2004) introduced a time dependent bond model by considering loading history on joint elements. (Dominguez, et al. 2005) defined 2D joint element considering different physical phenomenon like concrete cracking and friction between the materials within the thermodynamic framework (Figure 1.7d). (Sanz, Planas and Sancho 2013) proposed expanding joint elements (Figure 1.7e) to represent the corrosion of the reinforcement. Another alternative is the introduction of cohesive elements between the steel and concrete like (Rezazadeh, Carvelli and Veljkovic 2017) for example (Figure 1.7f).

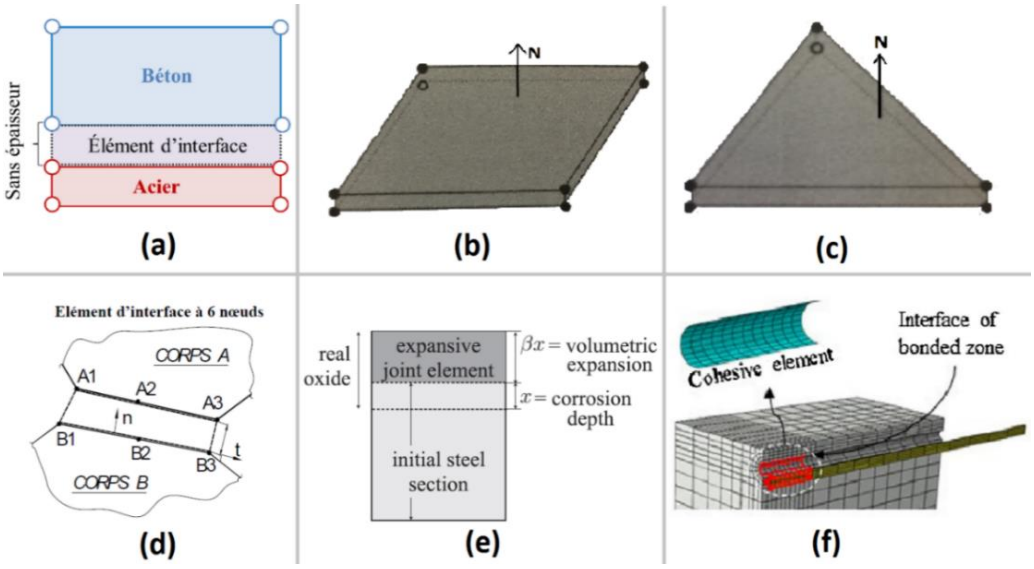

Figure 1.7 Representation of joint element: (a) (Clément 1987), (b) and (c) (Sanz and Planas 2018), (d) (Dominguez, et al. 2005), (e) (Sanz, Planas and Sancho 2013), (f) (Rezazadeh, Carvelli and Veljkovic 2017).

3.4. Coaxial joint element

The joint elements presented in section 3.3 are attractive since there is no need to define an interface zone like in section 3.2. However, they are difficult to apply to large structures (mesh difficulties, calculation time etc.) since the steel is represented by 2D or 3D elements, and since they need coincident meshing. For computational and meshing efficiency, steel reinforcement is often modeled with wired elements (truss or beam). Based on these considerations, a new element has been developed by (Mang 2016) after the work of (Torre-Casanova 2013). It is a coaxial zero thickness joint element which connects, through nonlinear behavior laws, a 1D wired steel finite element to the surrounding 3D concrete solid elements, with no need for coincident meshing. Indeed, the interface element has two nodes on steel element and two nodes on a segment strictly superimposed to the steel bar. The nodes of this superimposed segment are perfectly bounded to the concrete element by kinematic relations as in case of perfect bonding model. The slip between steel and concrete is calculated in the interface element and the stresses are computed through the bond behavior law. Methodology of the bond slip model and the numerical representation of the interface element can be seen in the Figure 1.8.

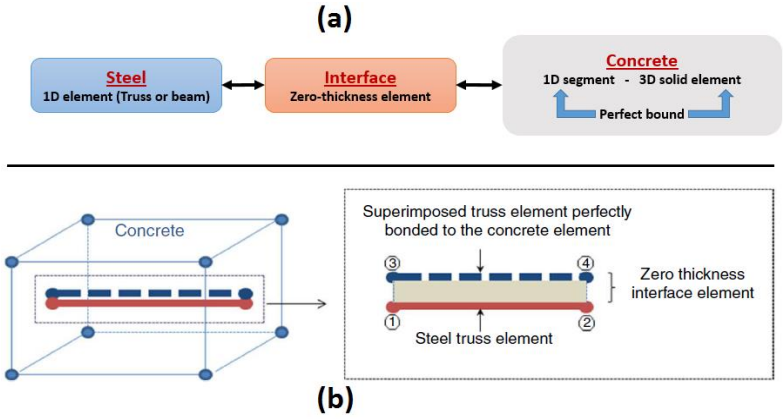

Figure 1.8 (a) Methodology of the model, (b) representation of interface element (Mang 2016).

The details of the formulation of this finite element will be presented in Chapter 2.

4. Steel-Concrete Bond Law

In this section, different adhesion laws from literature are presented in two different classes which are monotonic and cyclic laws respectively. The main parameters which are influencing the bond law are explained. It should be noted that the proposed bond laws from various authors for numerical applications as an input parameter are specific to the precise configurations which means that the characteristic values and the shapes of the law varies one author to another.

4.1. Monotonic Bond Law

One of the first experimental campaign on the steel-concrete bond is performed by (Abrams 1913), by performing pull-out tests. The influence of the several parameters on the bond behavior are tested like steel bar diameter, anchorage lengths, concrete aging. (Abrams 1913) claimed that the bond strength is decreasing with increasing steel bar diameter for plain bars (no ribs). Yet, the bond strength is independent from the embedment length of the steel bar. He observed that the slip is starting after a certain stress value which is equal to 1/6 of the concrete compressive strength. Some results showed that the rusted steel bars have higher bond strength than the polished ones. (Slater, Richart and Scofield 1920) made another pull-out test campaign in order to analyze the bond behavior. The proportion between bond strength and the concrete compressive strength suggested by (Abrams 1913) is approved by these series of experimental tests. Thus, lesser bond strength values are detected for painted steel bars compared to the unpainted ones which demonstrates the influence if the steel bar surface properties.

Furthermore, (Tepfers 1973) indicated the influence of the concrete tensile strength and the thickness of the concrete cover to the maximum bond stress. According to (Eligehausen, Popov and Bertero 1983), the bond resistance is provided with chemical adhesion in low slip values, micro interlocking mechanisms take place between the concrete cement and the irregularities on the steel bar surface when the load increases. The increase in the bond stress due to this interlocking mechanism then produces progressive cracking in the surrounding concrete cover. If the load continues to increase, the interlocking mechanisms gradually disappear due to the damage in the concrete cover as a result of cracking. Only the frictional forces take a part between the steel and concrete after that moment. This frictional resistance is estimated to be roughly 30% of the ultimate resistance force. A similar bond mechanism is also emphasized by a certain amount of authors like (Moretti and Tassios 2007), (Xu, Zhimin, et al. 2012), (Lim and Ozbakkaloglu 2014) etc. after different experimental campaigns on steel concrete bond behavior. In literature it is mentioned by (Verderame, et al. 2009) and (Xu, et al. 2016) that the frictional stress depends on the material properties, the geometry of the steel and concrete. The aggregate size, the steel surface area and geometry (ribs etc.) directly influence the friction between the two materials.

Based on the experimental campaigns mentioned above, influence parameters are detected. According to that, several adhesion laws are proposed in the literature. Among those, the simplest one is proposed by (Ngo and Scordelis 1967) as a linear law only focusing on the pre-peak behavior of the bond (Figure 1.9a). Whereupon, some bilinear (Figure 1.9b) or trilinear (Figure 1.9c) adhesion laws are proposed by various authors like (Khafallah and Ouchenane 2007), (Xia and Teng 2005), (Wang and Wu 2018) respectively. One of the most widely used adhesion law is the one proposed by (Eligehausen, Popov and Bertero 1983) including all stages of the adhesion law (pre-peak part, peak plateau and softening branch). The law is represented by an exponential pre-peak part, and linear peak and softening segments (Figure 1.9d). This law has been modified by several authors in order to adopt different cases and make more realistic bond presentations. For example, (Dehghani, et al. 2012) is assumed the pre-peak section as linear for simplification and (Tudjono, Pamungkas and Han 2014) only modified the law parameters (keeping the shape proposed by (Eligehausen, Popov and Bertero 1983)) according to their test setup. In literature, there are also several models for composite materials based on experimental results like (Lua, et al. 2005) who proposed two different (bilinear and polynomial) adhesion laws (Figure 1.9e). Finally, (Casanova, Jason and Davenne

2012) proposed an adhesion law which captures all pre-peak, softening and residual parts of the bond behavior (Figure 1.9f).

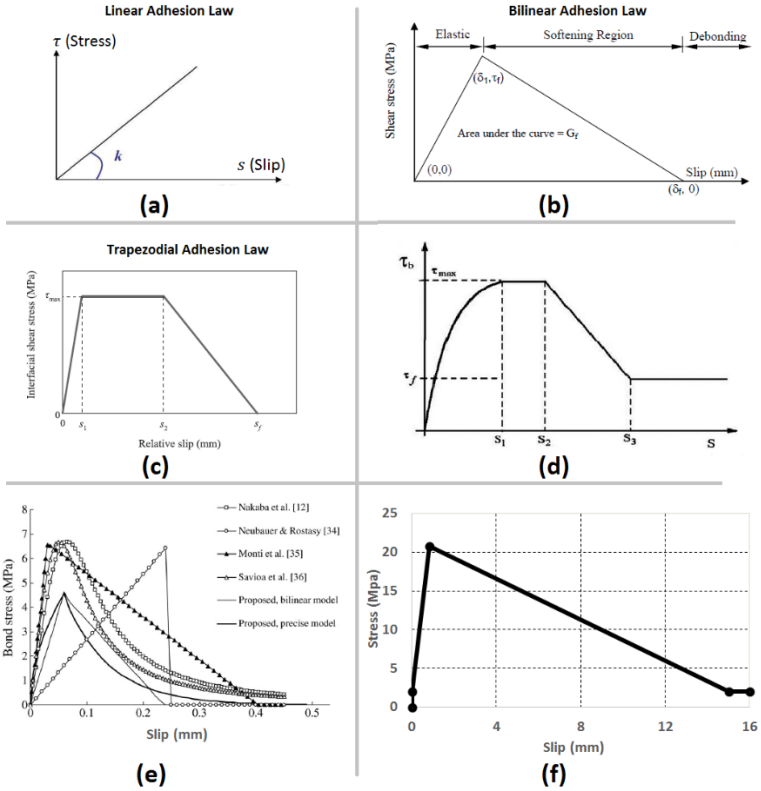

Figure 1.9 Examples of Adhesion Laws: (a) (Ngo and Scordelis 1967), (b) (Xia and Teng 2005), (c) (Wang and Wu 2018), (d) (Eligehausen, Popov and Bertero 1983), (e) (Lua, et al. 2005), (f) (Torre-Casanova 2013).

4.2. Cyclic Bond Law

In the case of an alternative loading, the mechanical behavior of the reinforced concrete structures can be strongly dependent on the steel-concrete bond. The chemical adhesion fails with increasing number of cycles which affects the general response of the structure. Only the frictional forces between the two materials remains for the adhesion between steel and concrete cover after several loading cycles (Eligehausen, Popov and Bertero 1983). Understanding of these phenomena is quite important to predict the general response of the reinforced structures under cyclic loading, especially when the crack properties are considered (Mang 2016). As mentioned before (in section 2), the crack pattern in reinforced structures is directly related to the steel-concrete bond behavior. Since this behavior is changing according to the loading history, the crack properties also depend on the irreversible behavior of the bond as well. It is essential to understand the behavior of adhesion in order to predict the structural behavior under cyclic loading.

The cyclic pull-out tests are studied by several authors like (Flippou, Popov and Bertero 1983), (Gan 2000), (Moretti and Tassios 2007), (Lindorf, Lemnitzer and Curbach 2009), etc. and cyclic adhesion laws are proposed to represent the irreversible behavior of the interface. One of the earliest cyclic bond model is suggested by (Morita and Kaku 1974) which considers the degradation of the bond capacities in relation to the number of cycles (Figure 1.10a). In addition, (Viwathanatepa , Popov and Bertero 1979) proposed a quadri-linear model of the concrete where degradation depends on the slip values (Figure 1.10b). (Eligehausen, Popov and Bertero 1983) defined a general analytical model based on their extensive experimental campaign in which the degradation of the bond strength is dependent on damage parameters of the corresponding cycles and slips. The ascending curve of the bonding law is represented by a monomial curve while the softening behavior is represented by a tri-linear curve (Figure 1.10c). They indicated that the majority of the bond strength and stiffness degradation can be observed in the first five loading cycles. This model is subsequently modified by (Flippou, Popov and Bertero 1983) for general applications (Figure 1.10d). (Verderame, et al. 2009) noted that the characteristic of the bond reach constant values after the first 3 cycles. They proposed a cyclic bond model which considers hysteric loops through the maximum slip values and the pure frictional resistance (Figure 1.10e). They presumed that the hysteric behavior of the bond is symmetric for both loading and reloading phases, and defined two main parameters for their irreversible bond model: the ultimate bond strength τ_u and the frictional bond strength τ_f. These parameters are derived from the compressive strength of the concrete f_c whith the following formulas:

$$\tau_u = 0.31 \times \sqrt{f_c} \tag{1.4}$$

$$\tau_f = 0.13 \times \sqrt{f_c} \tag{1.5}$$

Finally, (Mang, Jason and Davenne 2015)included a rough estimation of irreversible bond behavior into the bond-slip model of (Casanova, Jason and Davenne 2012) (Figure 1.10f). This latter model will be presented more in details in Chapter 2.

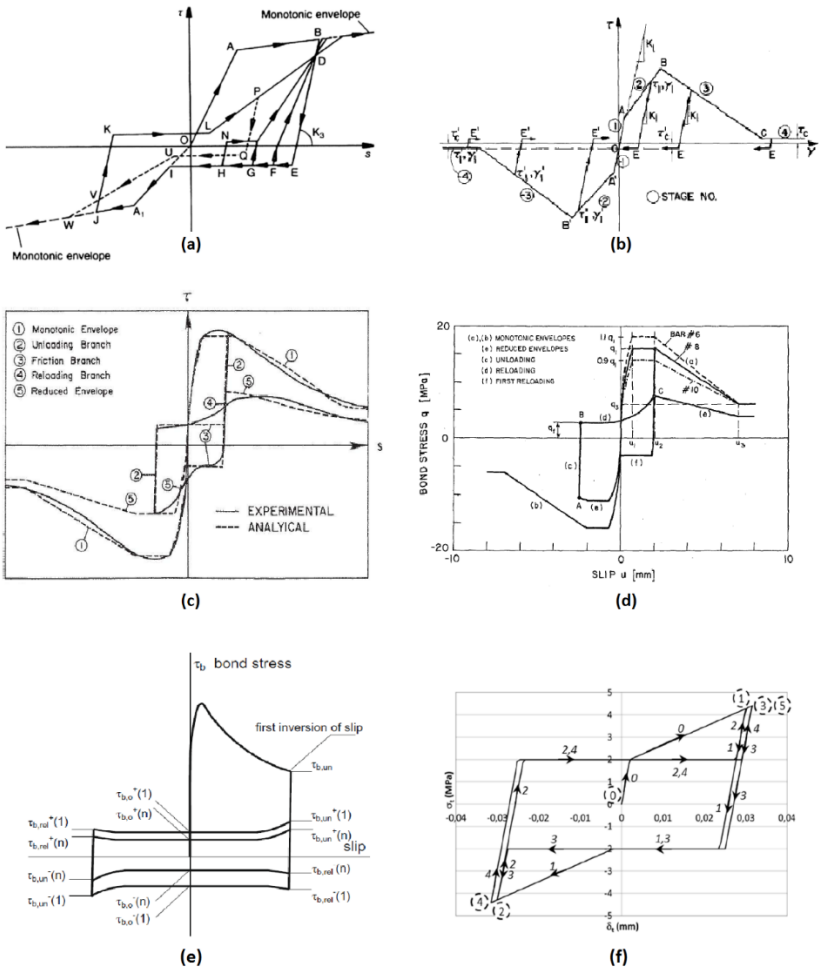

Figure 1.10 Bond-slip models for cyclic loading (a) (Morita and Kaku 1974), (b) (Viwathanatepa , Popov and Bertero 1979), (c) (Eligehausen, Popov and Bertero 1983), (d), (Flippou, Popov and Bertero 1983), (e) (Verderame, et al. 2009), (f) (Mang 2016).

4.3. Influence of the Confinement

The bond properties between steel and concrete are influenced by the concrete strength, concrete confinement, geometry of anchorage, geometry of concrete, reinforcement diameter, reinforcement deformation and yielding of reinforcement (Park and Paulay 1975), (Eligehausen, Popov and Bertero 1983), (Darwin, et al. 1996), etc. Numerous parameters should be considered in computational applications for an adequate representation of the bond behavior in reinforced concrete structures. One of these parameters is the confinement of concrete which increases the bond strength and anchorage behavior especially after ultimate strength by providing resistance against sudden brittle types of failure (Sulaiman, Ma, et al. 2017). Many authors like, (Karatas, Turk and Ulucan 2010), (Soylev and François 2005), (Yang, et al. 2015) etc. have pointed out the importance of the confinement on the steel-concrete bond properties in literature by some experimental and numerical studies. For that

reason, it is plausible to consider the confinement effect on the bond behavior in the numerical applications in order to have more factual presentation of the global and local behavior of the reinforced concrete structures. General information related with the concrete confinement and its relevance to the steel-concrete bond is presented in this section.

The aim of the confinement by means of lateral compression is to prevent a potential failure of the structure by shearing or splitting which are associated directly with the bond properties. It has been pointed out by (Park and Paulay 1975) that the increased concrete cover produces some extra resistance against splitting and consequently the transverse compression has a positive effect on adhesion and friction mechanisms between anchorage and the concrete. In the case of poor confinement, splitting occurs along the entire steel bar transmission layer which leads to a complete anchorage loss due to the spalling of concrete cover. On the contrary, when a well-confinement is considered, the circumferential tensile stress inducing splitting can be easily prevented increasing concrete cover thickness around the steel (Figure 1.11).

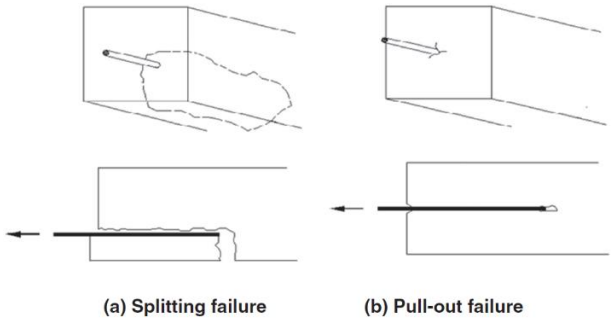

Figure 1.11 Types of anchorage failure (Sulaiman, Ma, et al. 2017).

The confinement effect can be considered in two ways:

- By means of an external loading on the structures (active confinement),
- By means of concrete cover or secondary reinforcements which prevent the concrete from cracking in certain directions (passive confinement).

Active confinement plays a role similar to an external loading. It reduces cracking phenomena of the concrete by preventing the expansion of the concrete and thus preventing micro cracking and by increasing the strength of the specimen in the direction of the tensile stresses. Active confinement results from the external lateral stress that provides confinement pressure inside the concrete and affects the bond strength between the concrete cover and the reinforcement bars (Figure 1.12). When the containment is exposed to an external load, the concrete is, in a way, pre-stressed. Its resistance increases, which has the effect of reducing its ability to crack (Malvar 1991).

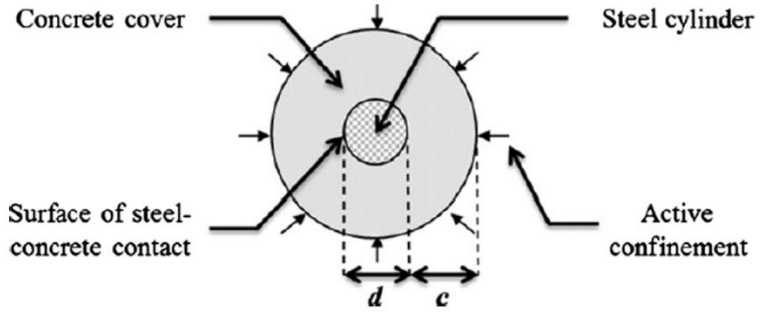

Figure 1.12 Principales of active confinement (Sulaiman, Ma, et al. 2017).

Passive confinement is composed of the lateral reinforcements surrounding the concrete structure that provides concrete confinement due to the bond stresses between steel and concrete that holds fast against the external and internal stresses (Figure 1.12). (Galvez, et al. 2009) studied the effect of concrete cover (especially underneath the steel bars) to the bond strength by performing an experimental campaign on a tie-rod (Figure 1.13). Splitting failures have been observed on the specimens with the thin concrete covers. The critical released load that showed the splitting failure diminished when the depth of the reinforcement indentations increased (Galvez, et al. 2009).

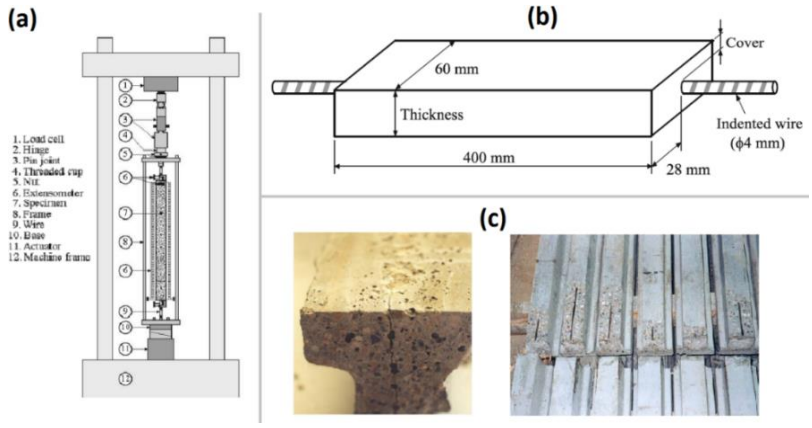

Figure 1.13 (a) Sketch of experimental test setup. (b) Geometry and dimensions of the specimens. (c) Example of splitting failure (Galvez, et al. 2009).

Transverse reinforcement inside concrete core is a passive type confinement and emerges only when concrete expands due to loading. When lateral expansion of concrete occurs, tensile hoop of transverse reinforcement arises to balance the concrete lateral expansion (Figure 1.14). (Yong, Nour and Nawy 1988) state that the strength and ductility of concrete can be enhanced by using rectangular, spiral or circular types of confinement. The internal cracking of concrete core due to natural volumetric expansion can effectively be prevented by providing sufficient lateral confinement to the concrete and this confined concrete exhibits higher strength than unconfined one.

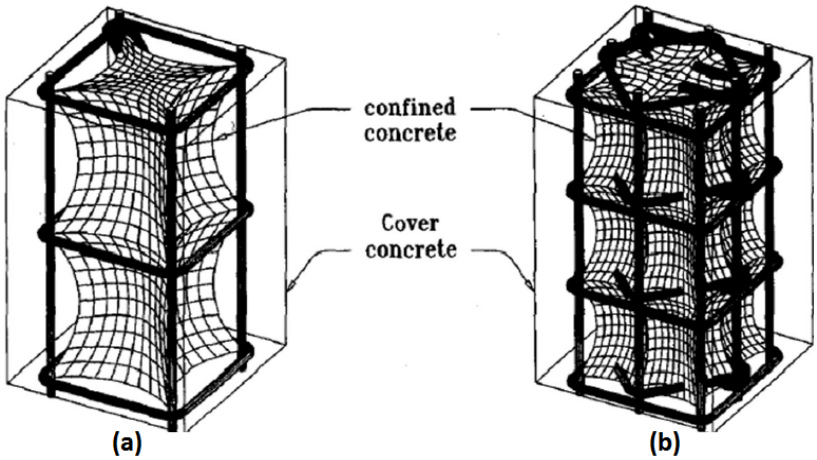

Figure 1.14 Configuration of passively confined concrete: (a) poorly confined concrete, (b) well confined concrete (Sulaiman, Ma, et al. 2017).

Active and passive confinement effect on the steel-concrete bond has been studied by many authors like (Bazant and Burrow 1980), (Magnusson 2000), (Venderame, et al. 2009), etc. As indicated earlier, bond-slip curve of reinforced concrete structures consists of 2 main parts: ascending and descending. Initially, the bond between steel and concrete is provided by chemical adhesion. Then the formation of micro cracks also known as bond cracks allows the steel bar slip along the force direction which resulted a non-linear bond slip curve. Finally, mechanical friction between two materials takes place. It has been shown by (Tepfers 1973), (Eligehausen, Popov and Bertero 1983), (Sulaiman, Ma, et al. 2017), (Baktheer and Chudoba 2018) etc. that the confinement has a vital effect on both ultimate bond stress τ_u and friction stress τ_{uf}.

A general way to investigate steel-concrete bond is to perform pull-out tests. (Eligehausen, Popov and Bertero 1983) have shown that the maximum bond stress increases in proportion to the rise in lateral pressure (Figure 1.15a). Thus, (Eligehausen, Popov and Bertero 1983) indicate that the lateral pressure has equal effects on maximum bond stress τ_u and friction stress τ_{uf} (Figure 1.15b). (Verderame, et al. 2009), (Jin, Li and Du 2016), (Li and Wu 2016) etc. also claimed that the active confinement has a significant effect on the cyclic bond behavior. (Verderame, et al. 2009) has declared that lateral pressure has a slight impact on the adhesion law but it becomes extremely important when alternative loads are considered. The lateral pressure affects the friction stress between the steel and the concrete which has a direct influence on the irreversible bond behavior. This behavior is then tested for cyclic slip with increasing the amplitude of lateral pressure by (Baktheer and Chudoba 2018). Some experimental studies like (Xu, Zhimin, et al. 2012), (Lim and Ozbakkaloglu 2014), (Zhang,

Wu, et al. 2016) etc. have also shown that the friction bond strength τ_{uf} depends not only on lateral pressure but also on the geometric-material properties of the steel and the concrete, on the embedment length and on the friction coefficient.

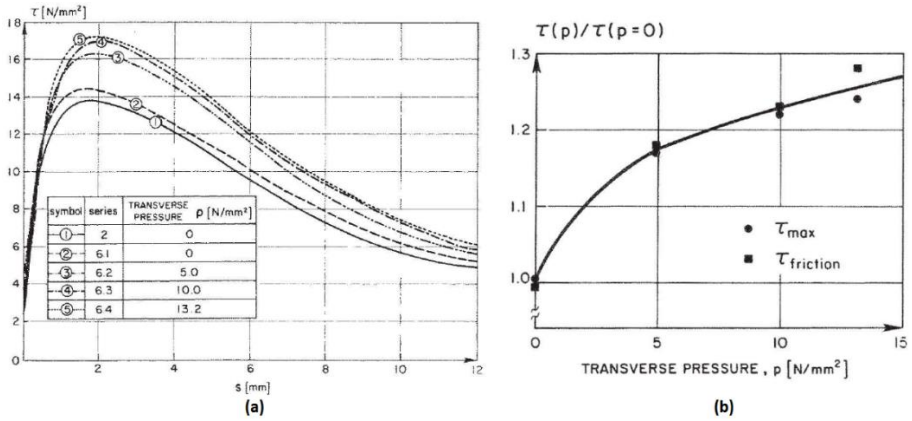

Figure 1.15 Influence of transverse pressure (a) on bond stress-slip relation, (b) on bond resistance (Eligehausen, Popov and Bertero 1983).

The bond behavior of the reinforced concrete structures is highly dependent on the confinement and it has a great importance in the design and the analysis of the concrete structures. Several pull-out tests are performed in order to investigate the bond behavior under lateral pressure in literature like (Xu, Zhimin, et al. 2012), (Wu, et al. 2014), (Lim and Ozbakkaloglu 2014) etc. Some empirical formulas are also proposed to define the bond stress, as a result of all these pull-out tests.

(Lowes, Moehle and Govindjee 2004) proposed a relationship between ultimate bond strength (τ_u) and confining pressure (P_{Lat}) based on the experimental investigations by (Eligehausen, Popov and Bertero 1983), (Malvar 1991), (Gambarova, Rosati and Zasso 1989) etc. (Figure 1.16). The proposed relationship is presented in Eq. 1.6.

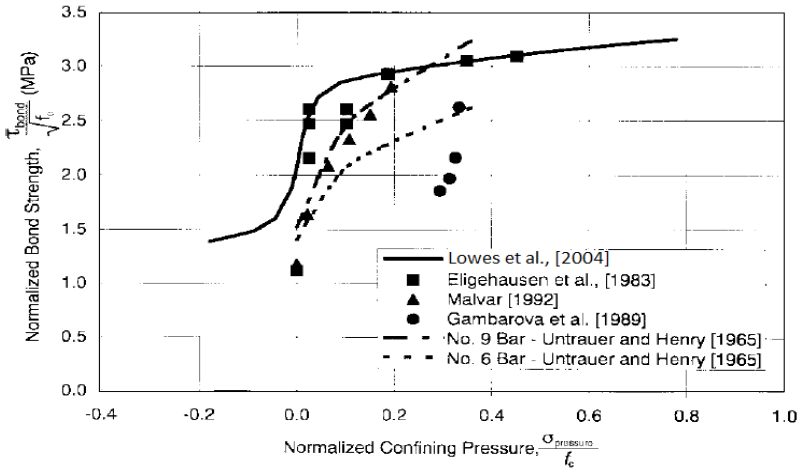

Figure 1.16 Bond strength as a function of confining pressure (Lowes, Moehle and Govindjee 2004).

$$\tau_u = 2.1\left[1-\lambda_1\left(1-e^{-40\left|\frac{P_{Lat}}{f_c}\right|}\right)-\lambda_2\left(1-e^{-\left|\frac{P_{Lat}}{f_c}\right|}\right)\right]\sqrt{f_c} \qquad (1.6)$$

where, f_c is the concrete compressive strength, λ_1 and λ_2 are model parameters which are 0.25 and 0.5 under tensile confining pressure and -0.35 and -0.4 for compressive confining pressure.

(Xu, Wu, et al. 2014) performed an experimental investigation on the bond behavior of plain round bars under lateral pressure (Figure 1.17a). It was concluded that the residual and ultimate bond strengths increase by increasing the average lateral pressure (Figure 1.17b). A constitutive model for bond with lateral pressure effect is presented (Eq. 1.7).

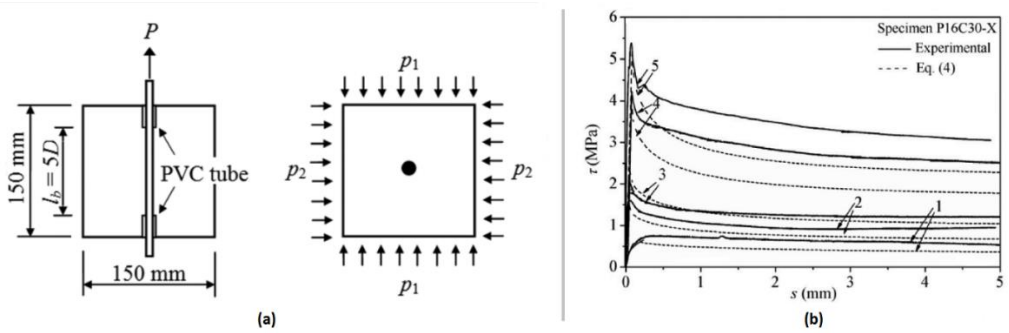

Figure 1.17 (a) Schematic representation of the pull-out test specimen, (b) Bond stress slip curves for different lateral pressures (Xu, Wu, et al. 2014).

$$\frac{\tau}{\sqrt{f_c}} = k_1 + k_2\frac{p_m}{f_c} \qquad (1.7)$$

where τ is the bond strength, f_c is the concrete compressive strength, k_1 denotes the bond strength ratio without confinement, k_2 denotes the contribution of the lateral pressure and p_m is the average value of lateral pressure ($p_m = \frac{p_1+p_2}{2}$).

Basing on the experimental data it was denoted that the lateral pressure can enhance the bond capacity by increasing frictional force at the steel-concrete interface when they are applied perpendicular to the steel rebar. It remains constant if applied pressure is parallel to the reinforcement. It has been recorded that the bond strength is increased by 300% when lateral pressure is increased from 0 to $0.6f_c$. Thus, the failure occurs by pull-out only when the lateral pressure is applied, otherwise the specimen fails by splitting.

Although the lateral compressive stress has a positive effect on the bond behavior, the lateral tensile stress has a negative effect on the bond behavior which causes a decrease in the bond strength (Lindorf, Lemnitzer and Curbach 2009), (Wu, et al. 2014) etc. (Figure 1.18a). An empirical formulation is suggested by (Zhang, Dong, et al. 2014) for the bond stress τ under lateral tensile stress as in the Eq. 1.8 based on a series of pull out tests. It has been discovered that both ultimate and residual bond strengths are significantly influenced by the applied lateral tension. The bond strength decreases exponentially with the increase of the average lateral tension (Figure 1.18b).

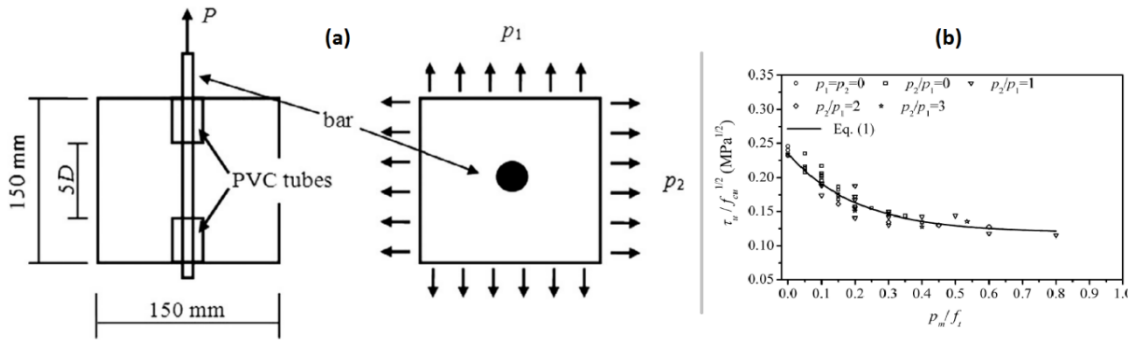

Figure 1.18 (a) Schematic representation of the pull-out test specimen, (b) relation between lateral stress and ultimate bond strength (Zhang, Dong, et al. 2014).

$$\frac{\tau_u}{\sqrt{f_c}} = 0.12 + 0.116e^{\left(-\frac{p_m}{f_t}\right)} \qquad (1.8)$$

where τ is the bond strength, f_c is the concrete compressive strength, k_1 denotes the bond strength ratio without confinement, k_2 denotes the contribution of the lateral pressure and p_m is the average value of lateral pressure ($p_m = \frac{p_1+p_2}{2}$).

Alternatively, (Wu, et al. 2014) proposed an empirical formulation for the bond strength by considering lateral tension and compression effect (Eq. 1.9) based on pull-out tests (Figure 1.19a). They observed the negative effect of lateral tension (Figure 1.19b) and the positive effect of lateral compression (Figure 1.19c) on the bond strength.

$$\frac{\tau_u}{\sqrt{f_c}} = a - b\frac{p_t}{f_t} + c\frac{p_c}{f_c} - d\frac{p_t}{f_t}\frac{p_c}{f_c} \qquad (1.9)$$

where, a, b, c are the coefficients based on material properties, p_t is the lateral tension and p_c is the lateral compression, f_c is the concrete compressive strength and f_t is the concrete tensile strength

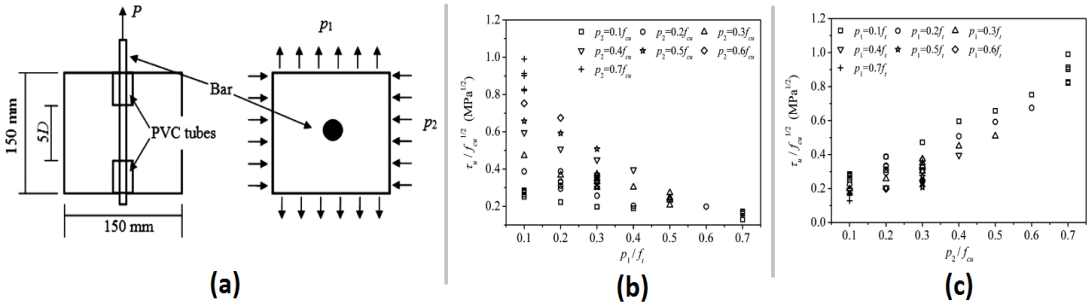

Figure 1.19 (a) Schematic representation of the pull-out test specimen, (b) relation between lateral tension and ultimate bond strength, (c) relation between lateral compression and ultimate bond strength (Wu, et al. 2014).

(Zhang, Wu, et al. 2016) claimed that the friction plays the main role for the bond behavior when the lateral tension is applied especially when plain round bars are considered. They also have suggested another empirical formulation for the bond strength due to the frictional effect (τ_f) for plain round bars embedded inside concrete subjected to lateral tension. The empirical formulation proposed by (Zhang, Wu, et al. 2016) is presented in the Eq. 1.10.

$$\tau_f = \frac{(E_s^*\varepsilon_0 - 2\alpha p_m)R_s}{2\nu_s l_d}\left(0.113 + 0.04\mu\frac{l_d}{R_s}\right) \qquad (1.10)$$

where, ε_0 shrinkage concrete strain, E_s elastic modulus of steel, E_c elastic modulus of concrete, ν_s Poisson ration of steel, ν_c Poisson ratio of concrete, R_s is the radius of steel, l_d is the embedment length, μ is the friction coefficient, p_m is the average lateral pressure and α is a coefficient as:

$$\alpha = \frac{E_s^*}{E_c^*} \text{ where } E_c^* = \frac{E_c}{(1-\upsilon_c^2)} \text{ and } E_s^* = \frac{E_s}{(1-\upsilon_s^2)}$$

(Robins and Standish 1982) is performed two different types of experimental campaign with pull-out test and semi-beam test (Figure 1.20) to examine the effect of active confinement to the steel-concrete bond by pointing out that the lateral pressure effect on the bond is mainly frictional for round bars. They also claimed the pull-out load may increase around 200% and bond strength may increase around 50% for round bars when applied external lateral pressure is close to concrete compressive strength. Thus, they suggested an empirical formulation for the frictional bond strength (τ_f) (Eq. 1.11).

$$\tau_f = \frac{(\varepsilon_0 + \varepsilon_0^*)E_s}{\nu_s}\left[1 - \exp\left(\frac{-2E_c\nu_s\mu l_d}{E_s d_s(1+\nu_c)}\right)\right] \tag{1.11}$$

Here the lateral pressure is included as increase in strain (ε_0^*) by following equation:

$$\varepsilon_0^* = p_m\left[\frac{1}{E_c}\left(\frac{d_s^2 + (d_s + c)^2}{(d_s + c)^2 - d_s^2}\right) + \frac{1 - \nu_s}{E_s}\right] \tag{1.12}$$

where, c is the thickness of concrete cover and d_s is the diameter of the steel bar.

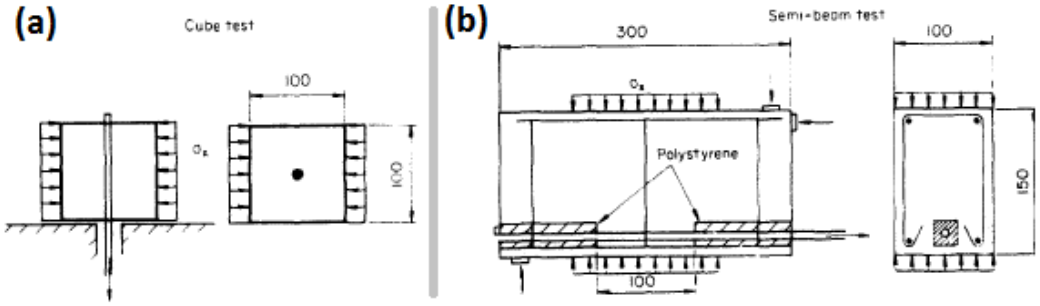

Figure 1.20 Representation of (a) pull-out test geometry, (b) semi-beam geometry (Robins and Standish 1982).

The general conclusion of (Robins and Standish 1982)'s study is that the effect of lateral stress is evident not only on the ultimate bond strength (τ_u) but throughout the whole loading processes which effects the entire adhesion law.

The effect of confining concrete around the steel bar on the steel-concrete bond properties have also been investigated by several authors ((Sulaiman, Redzuan, et al. 2017), (Rao, Pandurangan and Sultana 2007)). Among those, (Orangun, Jirsa and Breen 1977) proposed an empirical equation for the bond strength by including the effect of concrete cover (Eq. 1.13).

$$\frac{\tau_u}{\sqrt{f_c}} = 1.22 + 3.23\frac{c_{min}}{d_s} + 53\frac{d_s}{L_s} \tag{1.13}$$

where, L_s is reinforcement length, d_s is steel bar diameter, c_{min} is minimum of $[c_x, c_y, c_s]$, c_x is side cover thickness, c_y is bottom cover thickness and c_s is the bar spacing distance.

Another alternative equation is proposed by (Darwin, et al. 1996) in order to determine the cover thickness for the design of reinforced concrete structures (Eq. 1.14).

$$\frac{\tau_u}{\sqrt{f_c}} = [8.76 L_s (c_{min} + 0.5 d_s)] \left(0.14 \frac{c_{max}}{c_{min}} + 0.86\right) \qquad (1.14)$$

where c_{max} is the maximum of $[c_x, c_y, c_s]$.

(Esfahani and Rangan 2000) have successfully represented the passive confinement effect on the steel-concrete interface specifically by defining the dependence of the bond strength to the concrete cover. More detailed formulation of the bond strength is presented:

$$\tau_u = \tau_o \frac{1 + 1/M}{0.85 + 0.024\sqrt{M}} \left(0.88 + 0.12 \frac{c_{med}}{c_{min}}\right) \qquad (1.15)$$

with,

$$\tau_o = 4.9 \frac{(c_{min}/d_s) + 0.5}{(c_{min}/d_s) + 3.6} f_{ct} \qquad (1.16), \qquad M = \cosh\left(0.0022 L_s \sqrt{\frac{3 f_{ct}}{d_s}}\right) \qquad (1.17)$$

where, c_{med} is the median of $[c_x, c_y, c_s]$ and $f_{ct} = 0.55\sqrt{f_c}$.

Furthermore, (Hadi 2008) performed pull-out test with different steel bar diameters which have same concrete covers (Figure 1.21a) to identify a simplified formulation for the bond strength (Eq. 1.18) by combining the equations proposed by (Orangun, Jirsa and Breen 1977), (Darwin, et al. 1996) and (Esfahani and Rangan 2000). The comparison of the proposed empirical equations with measured bond strengths is given in Figure 1.21b.

$$\frac{\tau_u}{\sqrt{f_c}} = 0.083045 \left[22.8 - 0.208 \frac{c_{min}}{d_s} - 38.212 \frac{d_s}{l_d}\right] \qquad (1.18)$$

where, l_d is the embedded length of the reinforced bar.

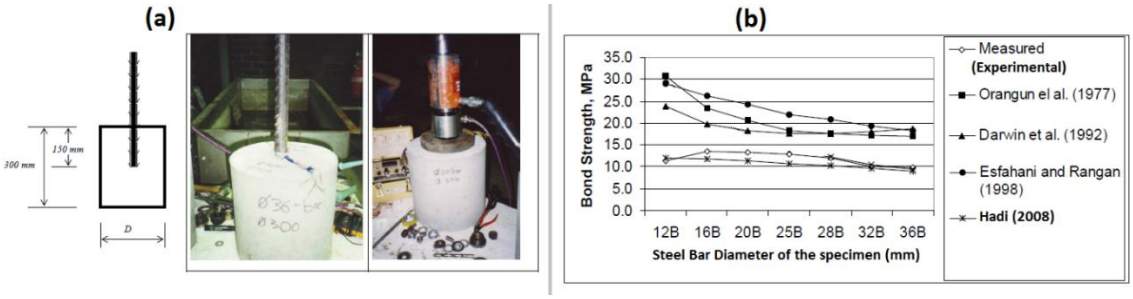

Figure 1.21 (a) Details of the specimen, (b) Comparison of the bond strengths (Hadi 2008).

Finally, (Torre-Casanova, Jason, et al. 2013) studied the passive confinement effect with numerical simulations of a bar with ribs embedded in a concrete cylinder, with different concrete covers. They identified a transition between the two different failure modes (splitting and pull-out) depending on the concrete cover to steel bar diameter ratio (c/d_s) (Figure 1.22). The evolution of the bond strength with the concrete cover is governed by the given equations:

For splitting failure where $\frac{c}{d} \leq 4.5$:

$$\frac{\tau_u}{f_t} \approx 1.53\frac{c}{d_s} + 0.36 \qquad (1.19)$$

For pull-out failure where $\frac{c}{d} > 4.5$:

$$\frac{\tau_u}{f_t} \approx 7.2 \qquad (1.20), \qquad \frac{\tau_u}{f_c} \approx 0.6 \qquad (1.21)$$

where, d is the steel bar diameter, c is the thickness of the concrete cover, τ_u is the ultimate bond strength, f_t is the tensile strength of the concrete and f_c is the compressive strength of the concrete.

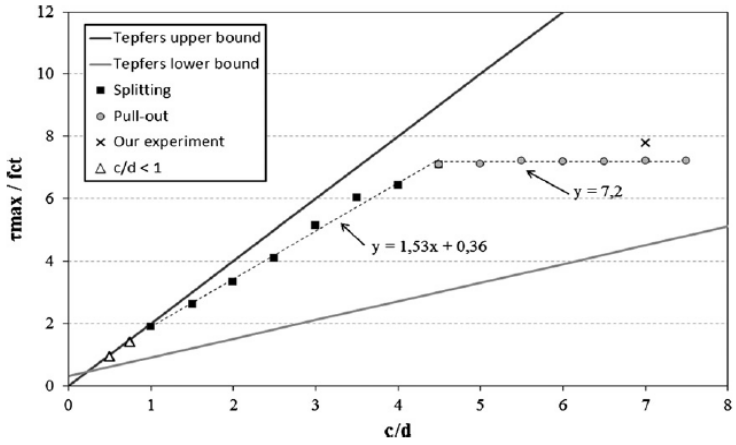

Figure 1.22 Bond strength evolution with concrete cover (Casanova, Jason and Davenne 2012).

The equations (Eq. 1.19, 1.20 and 1.21) proposed by (Torre-Casanova, Jason, et al. 2013) have completed the work from (Uijl and Vliet 1996) who developed certain constitutive equations for the splitting failure depending on the passive confinement. Thus, according to these results, transition from splitting failure to pull-out failure can be determined from Eq. 1.22.

$$\left(\frac{c}{d_s}\right)_{\text{splitting to pull-out}} = 0.39\left(\frac{f_c}{f_t}\right) - 0.24 \qquad (1.22)$$

The results have shown that the maximum bond strength (τ_u) first increases linearly when the steel to concrete cover ratio ($\frac{c}{d_s}$) increases up to a certain level and finally becomes constant.

All the equations from various authors which are presented above related with the confinement effect on the bond behavior can be summarized as in Table 1.1.

Table 1.1 Proposed empirical equations for confinement effect on the bond.

Author	Confinement Type	Reinforcement	Equation
(Orangun, Jirsa and Breen 1977)	Passive	Deformed	1.13
(Robins and Standish 1982)	Active	Plain round	1.11
(Darwin, et al. 1996)	Passive	Deformed	1.14
(Esfahani and Rangan 2000)	Passive	Deformed	1.15
(Lowes, Moehle and Govindjee 2004)	Active	Deformed	1.6
(Hadi 2008)	Passive	Deformed	1.18
(Torre-Casanova, Jason, et al. 2013)	Passive	Deformed	1.19-1.20-1.21
(Wu, et al. 2014)	Active	Plain round	1.9
(Xu, Wu, et al. 2014)	Active	Plain round	1.7
(Zhang, Dong, et al. 2014) (Zhang, Wu, et al. 2016)	Active	Plain round	1.8-1.10

Consequently, active and passive confinement should be considered carefully especially for the numerical analysis of the structural elements.

5. Dowel Action

Dowel action is one of the shear transfer mechanisms that plays an important role for the shear resistance of the reinforced concrete structures. Therefore, it should also be considered in numerical applications where the shear forces are taken into account. In this section, the shear resistance of the reinforced concrete structures is going to be explained by focusing on the dowel action mechanism.

Shear transfer mechanisms of cracked reinforced concrete structures consist of three main parameters (Figure 1.23) according to (Jelic, Pavlovic and Kotsovos 1999), (Nogueira, Venturini and Coda 2013) and (Xia, et al. 2015)**:**

- Shear resistance of un-cracked concrete
- Aggregate interlock
- Dowel action

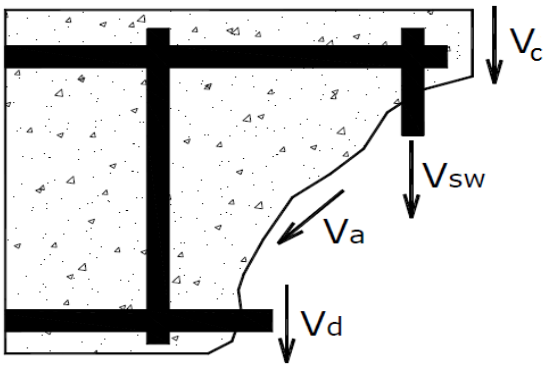

Figure 1.23 Cracked reinforced concrete member and shear force mechanisms (Nogueira, Venturini and Coda 2013).

Current consideration on the shear transfer philosophy of the reinforced concrete members is based on the assumption that the internal stress is mainly concentrated on the cracked regions (Walraven and Reinhardt 1981). In Figure 1.23, V_c denotes the concrete resistance itself which can be expressed as the contribution of concrete itself to the shear resistance during the un-cracked stage due to its material properties, V_{sw} denotes the shear reinforcement resistance, V_a denotes the aggregate interlock resistance, and V_d denotes the dowel action resistance. (Xia, et al. 2015) represents the total shear force (V) in reinforced concrete structures as a combination of all these forces with the Eq. 1.23:

$$V = V_c + V_a + V_d + V_{sw} \qquad (1.23)$$

According to (Kim and Park 1996) and (Xia, et al. 2015), the contributions of these components to the total shear resistance are estimated as follows:

- 20-40% un-cracked concrete resistance
- 25-50% aggregate interlock
- 15-25% dowel action

On the other hand, (Jelic, Pavlovic and Kotsovos 1999) indicates that it is usually difficult to measure the contributions of each force transfer mechanism to the total shear resistance, since they always combine with each other especially when dowel action is considered.

5.1. Definition of Dowel Action

Concrete blocks at two sides of the crack slide against each other, the bar embedded inside the concrete is subjected to a relative transverse displacement. The contra flexural bending of the two ends of the reinforced bar is called “Dowel Action”. Dowel action can be defined as the force transfer capacity of the reinforcing bars in perpendicular direction to their axis. This kind of effect arises only if the crack surfaces is widened up to a certain amount. However, only a certain length of the bar is subjected to a significant deformation (Figure 1.24).

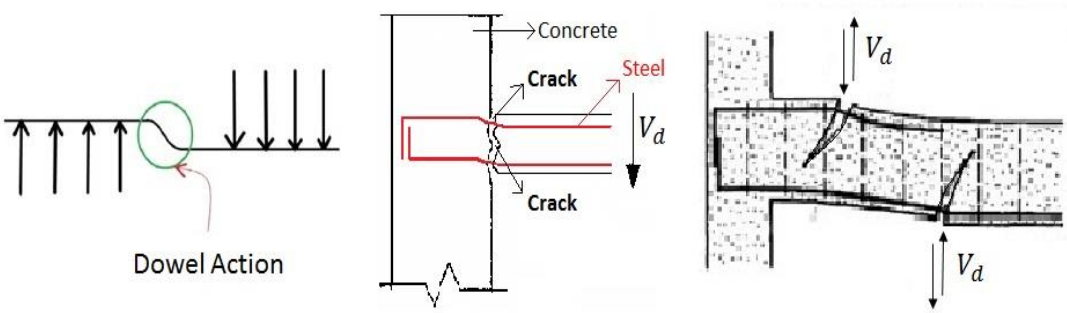

Figure 1.24 Representation of Dowel Action (Ince, Yalcin ve Arslan 2003).

Dowel action occurs only if the crack exists (Figure 1.24). It becomes significant around the peak loading stage. Dowel Strength across the shear plane is a combination of shear, kinking and bending of reinforcement which is represented in Figure 1.25 (Park and Paulay 1975). The influence of the dowel action is normally ignored during the design of reinforced concrete beams since shear reinforcement (vertical or web) offers a significant amount of shear resistance. However, for ultra-high-performance concrete (UHPC) structures without shear reinforcement, dowel action contribution to the shear resistance becomes an important parameter and should be considered in the design stage in order to assure non-brittle type of failure (Xia, et al. 2015).

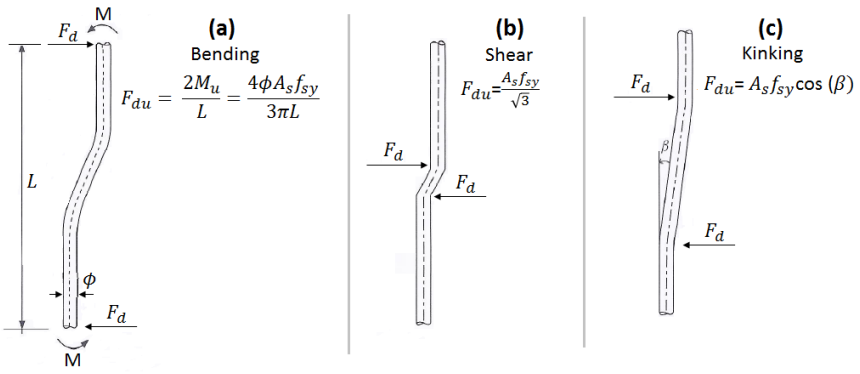

Figure 1.25 Deformation mechanisms of a steel bar: (a) bending, (b) shear, (c) Kinking (Park and Paulay 1975).

5.2. Experimental Characterization

As mentioned before, it is challenging to distinguish dowel action among other shear transfer mechanisms since the transfer is combination of all. For that reason, limited test setups exist in literature for the purpose of investigating specifically the dowel action behavior in reinforced concrete structures. Among those, the most common one is the double L shape beam specimen (L-beam) separated from each other by a small gap which eliminates aggregate interlock and concrete resistance. In literature, several push-off tests are performed on L-beams like, (Sagaseta and Vollum 2011), (Xiao, Li and Li 2014), (Navarro-Gregori, et al. 2016) etc. in order to investigate the dowel action. The geometry of L beam can be seen in Figure 1.26a. Alternatively, (Husain, Oukaili and Muhammed 2009) performed some tests on rectangular concrete prisms so called semi-beams to measure dowel effect. The semi-beams were separated by a thin polythene layer in order to eliminate aggregate interlock and concrete resistance itself (Figure 1.26b). Again with L-beam push-off tests, (Ince, Yalcin and Arslan 2007) showed that the dowel strength decreases as the structure size increases by obtaining coherent results with the Bazant's size effect law (Z. Bazant 1984). On the other hand, (Xiao, Li and Li 2014) investigated the dependence of the temperature effect on the shear transfer mechanism with L-beam push-off tests in different temperatures and concluded that the shear resistance (and also the dowel strength) is decreasing by increasing concrete and steel temperatures.

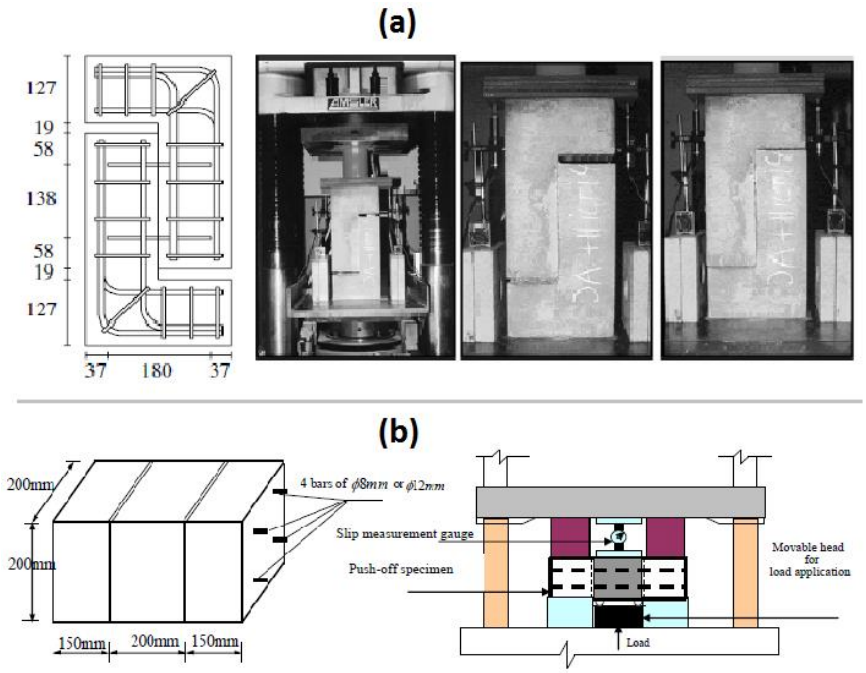

Figure 1.26 Push-off specimen geometry: (a) L-beam (Júlio, et al. 2010), (b) semi-beams (Husain, Oukaili and Muhammed 2009).

L-beams and semi beams are the geometries to investigate dowel action at the laboratory scale applications. At the structural scale, the bending tests on deep beams are a common way to investigate the shear behavior of the reinforced concrete structures including dowel action according to the literature (Al-Nahlawi and Wight 1992), ((Hassan, Hossain and Lachemi 2010), (Abed, El-Chabib and AlHamaydeh 2012) etc.). By means of bending tests on deep beams (Figure 1.27), the contribution of dowel action to the total shear behavior can be investigated.

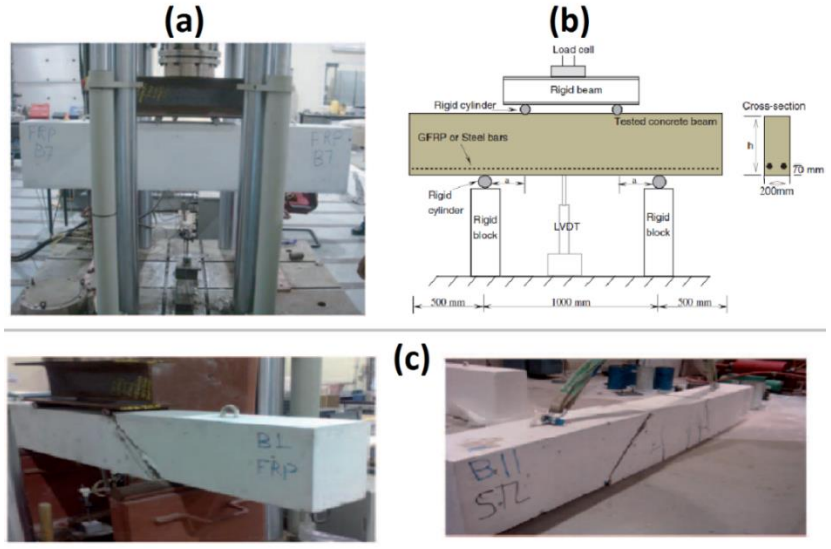

Figure 1.27 (a) Geometry of the deep beam specimens. (b) Sketch of experimental bending test setup (c) Example of shear failure on deep beams (Abed, El-Chabib and AlHamaydeh 2012).

As a sum up, according to the (Jelic, Pavlovic and Kotsovos 1999), (Ince, Yalcin and Arslan 2007) and (Nogueira, Venturini and Coda 2013) dowel action depends on:

- Reinforced layout (longitudinal and transversal reinforcement ratio),
- Structural geometry of the concrete (concrete cover),
- Material properties of concrete and reinforcement,
- Arrangement of the applied loads (location, direction, distribution, value, etc.),
- Crack pattern (angle, width, location, etc.).

Since it depends on many parameters, it is not easy to investigate the dowel action separately among the other transfer components. Furthermore, the contributions of these parameters keep on changing when the applied loads increase due to the internal stress distribution (Jelic, Pavlovic and Kotsovos 1999).

5.3. Analytical Representation

There have been many studies like (Kazakoff 1974), (Sorousian 1987), (Kim and Park 1996), (Ashour 1997), etc. that were carried out to understand the mechanisms of shear transfer in reinforced concrete structures and to represent them by various numerical and/or analytical methods. Among those, (Dulacska 1972) and (Vintzeleou and Tassios 1987) defined similar formulations (Eq. 1.24) for estimating the ultimate dowel strength (V_{du}) at the peak stage based on experimental results.

$$V_{du} = 1.27 d_s^2 \sqrt{f_c f_y} \qquad (1.24)$$

where d_s is the steel bar diameter, f_c is the compressive strength of the concrete and f_y is the yield strength of the dowel bar. The constant value 1.27 is modified slightly by some authors afterwards (eg. (Kwan and Ng 2012)).

Alternatively, several authors invoke different parameters to define ultimate dowel strength (V_{du}) and suggested various empirical expressions 1.25 (Baumann and Rüsch 1970), 1.26 (Houde and Mirza 1974) and 1.27 (Sorousian 1987).

$$V_{du} = 1.64 b_{eff} d_s \sqrt[3]{f_c} \qquad (1.25)$$

$$V_{du} = 37 b_{eff} \sqrt[3]{f_c} \tag{1.26}$$

$$V_{du} = \alpha f_t b_{eff} \frac{\pi}{2\beta} \leq 1.27 {d_s}^2 \sqrt{f_c f_y} \tag{1.27}$$

where, f_t is the tensile strengths of the concrete, b_{eff} and $\frac{\pi}{2\beta}$ are the effective width and length of the beam respectively and α is a constant parameter.

(Kim and Park 1996) stated that the dowel action contribution is extremely dependent on the thickness and the strength of the concrete cover. (Ince, Yalcin and Arslan 2007) concluded that the dowel action contribution increases with the increase of ρf_y value, where ρ is the reinforcement ratio and f_y is the reinforcement yield stress, and proposed Eq. 1.28:

$$V_{du} = \rho \sqrt{f_c f_y \sin(\theta)} \left[1 + \sqrt{\frac{36}{d_{agg}}}\right] \left[1 + \frac{L}{19.4 d_{agg}}\right]^{-1/2} \tag{1.28}$$

where, d_{agg} is the aggregate size and θ is the inclination angle of reinforcement normal to the shear plane.

Furthermore, the dowel force depending on the steel bar deformation along the loading process can be analyzed by using the "beam on elastic foundation" theory in order to deal with the interaction between the steel bar and surrounding concrete. The foundation may be treated as a bed of Winkler springs so that the reaction force at any point may be assumed to be proportional to the deflection of the beam at that point (Figure 1.28a).

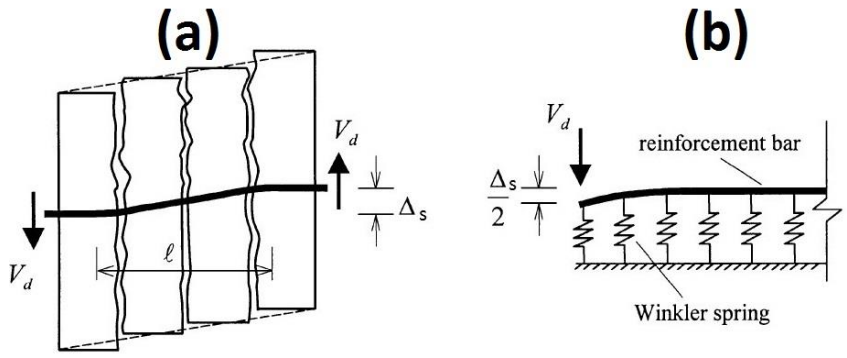

Figure 1.28 Winker spring representation of shear force (He and Kwan 2001).

According to the beam in elastic foundation theory, (Kwan and Ng 2012) expressed a linear elastic-perfectly plastic force-displacement behavior described as the following:

$$V_d = k_d \Delta_d \text{ for } \Delta_d \leq \Delta_{du} \quad (1.29)$$

$$V_d = V_{du} \text{ for } \Delta_d > \Delta_{du} \quad (1.30)$$

where, V_d is the dowel force, V_{du} is the ultimate dowel force proposed by (Sorousian 1987), Δ_d is the dowel displacement, Δ_{du} is the displacement at the ultimate dowel force and k_d is the dowel stiffness.

The dowel bar which can be considered as a semi-infinite beam on an elastic foundation as in Figure 1.28b. Based on the analytical solution of the beam on elastic foundation problem, the displacement at any point along the dowel bar Δ_{dx} can be derived as:

$$\Delta_{dx} = \frac{V_d}{E_s I_s \lambda^3} e^{-\lambda x} \cos(\lambda x) \quad (1.31)$$

where x is the distance from the dowel force, E_s is the elastic modulus of dowel bar, I_s is the moment of inertia of the steel bar (equals to $\frac{\pi d_s^4}{64}$ with d_s the diameter of the steel bar) and λ represents the relative stiffness of the foundation, which can be determined from the formula below (Sorousian 1987):

$$\lambda = \sqrt[4]{\frac{k_c d_s}{4 E_s I_s}} \quad (1.32), \qquad k_c = \frac{127c\sqrt{f_{cc}}}{d_s^{2/3}} \quad (1.33)$$

The dowel force is applied for x = 0. Hence, by substituting x by zero in the Eq. 1.31, the dowel force-displacement relation can be written as following:

$$V_d = E_s I_s \lambda^3 \Delta_d \quad (1.34)$$

From which the dowel stiffness in the Eq. 1.29 can be described as:

$$k_d = E_s I_s \lambda^3 \quad (1.35)$$

Combining the studies of (Dulacska 1972) and (Sorousian 1987), (El-Ariss 2007) also proposed an alternative formulation (1.36) for the dowel force (V_d) depending in the dowel bar displacements (Δ_d) based on beam on elastic foundation presented above.

$$V_d = V_{du}\left[1 - \exp\left(-\frac{k_d \Delta_d}{V_{du}}\right)\right] \quad (1.36)$$

where, V_{du} is the ultimate dowel force proposed by (Dulacska 1972) as in Eq. 1.24 and k_d is the stiffness of elastic foundation which is proposed by (Sorousian 1987) as in the Eq. 1.35.

5.4. Numerical Representation

The dowel force-displacement relationship which was derived, based on the beam on elastic foundation theory, can also be expressed by the dowel stress and strain, in order to be compatible with the numerical applications together with cracked and damaged reinforced concrete models (Ashour 1997), (Jelic, Pavlovic and Kotsovos 1999), (He and Kwan 2001). Even though the flexural behavior of reinforced concrete structures can be predicted quite accurately by using simple bending theories, the prediction of shear behavior remains as a challenging task even with the sophisticated finite element methods.

Finite element modeling of dowel action has three major difficulties according to (He and Kwan 2001):

- It is difficult to measure the dowel action directly since the shear transfer occurs with the other transfer parameters. Therefore, experimental results are rather limited for the comparison with the numerical ones.
- It is difficult to represent the dowel action in finite element methods in a simple manner. Proper finite element analysis of the dowel action requires individual modeling of steel bars, very fine meshing of the structure and taking very small loading steps.
- Since dowel action is significant in the post peak loading stage, experimental testing and theoretical analysis should also include these stages.

According to the mentioned difficulties above, numerical representation of the dowel action should be analyzed very carefully by considering all the possible parameters which might affect the numerical calculation.

(Frantzeskakis and Theillout 1989) proposed a smeared element for numerical representation of reinforced concrete structures by including a linear model for dowel action phenomenon (Figure 1.29a). The dowel action of the steel bar inside the concrete cover is substituted by

equivalent normal and shear stresses action on the surface of the cracks (Frantzeskakis and Theillout 1989). Alternatively, a composite material model is used by (Oliver, et al. 2008) which takes dowel action into account with fiber bundles (Figure 1.29b). In this composite model the dowel action is considered separately in composite strains to calculate composite stresses.

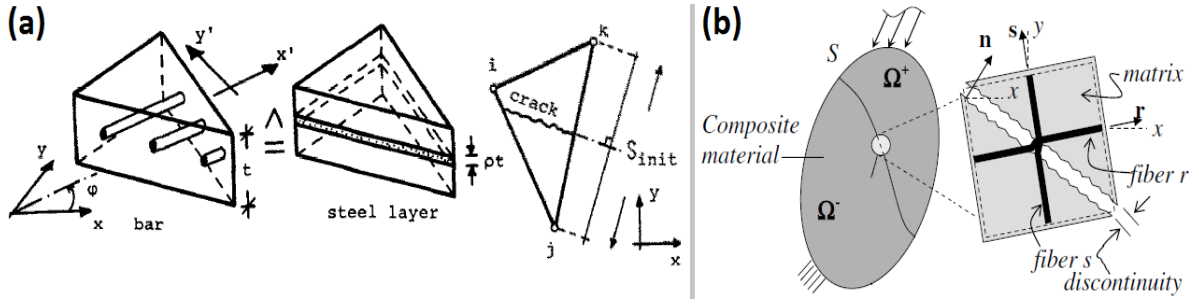

Figure 1.29 (a) Representation of the (a) smeared element for reinforcement (Frantzeskakis and Theillout 1989), (b) composite element with fiber bundles (Oliver, et al. 2008).

(Martin-Pérez and Pantazopoulou 2001) proposed a numerical model combining all the shear forces including dowel action based on beam on elastic foundation theory (Figure 1.30). The authors represented the total shear resistance (υ_{xy}) by the given equation:

$$\upsilon_{xy} = \upsilon_c + \upsilon_s + \upsilon_p \qquad (1.37)$$

where, υ_p is the compressive normal boundary stresses (axial loads) which are applied, υ_c and υ_s are the shear contributions of concrete and steel respectively.

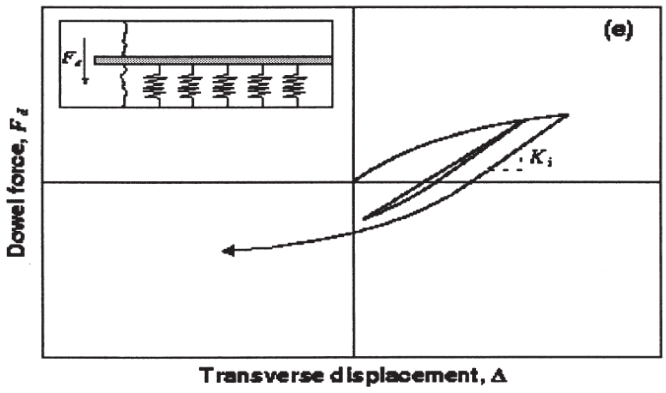

Figure 1.30 Relationship between dowel force and transverse displacement (Martin-Pérez and Pantazopoulou 2001).

(Martin-Pérez and Pantazopoulou 2001) included the dowel action within the υ_c component by defining a constative law of dowel force (V_d) given below:

$$V_d = V_{du}\left[1 - e^{\left(\frac{-K_i \Delta}{V_{du}}\right)}\right] \tag{1.38}$$

where V_{du} is the ultimate dowel force, Δ is the displacement across the crack, K_i is the initial dowel stiffness.

The ultimate dowel force and initial dowel stiffness are defined as following according to (Martin-Pérez and Pantazopoulou 2001):

$$V_{du} = 1.3{D_s}^2\sqrt{f_c f_y(1 - A^2)} \tag{1.39}$$

$$K_i = 0.166K_f^{0.75}d_s^{1.75}E_s^{0.25} \tag{1.40}$$

where, f_c is the concrete compressive strength, f_y is the yield strength of steel, A is the ratio of applied axial force to yield axial force, d_s is the bar diameter, E_s is the elastic modulus of steel and K_f is the foundation stiffness calculated from following equation:

$$K_f = 127\beta\sqrt{f_c}\left[\frac{1}{d_s}\right]^{2/3} \tag{1.41}$$

with a constant β value ranging from 0.6 to 1.

Another representation of dowel action is proposed by (He and Kwan 2001) for simulations where the steel and the concrete were discreetly represented in a way given in Figure 1.31a in 2D.

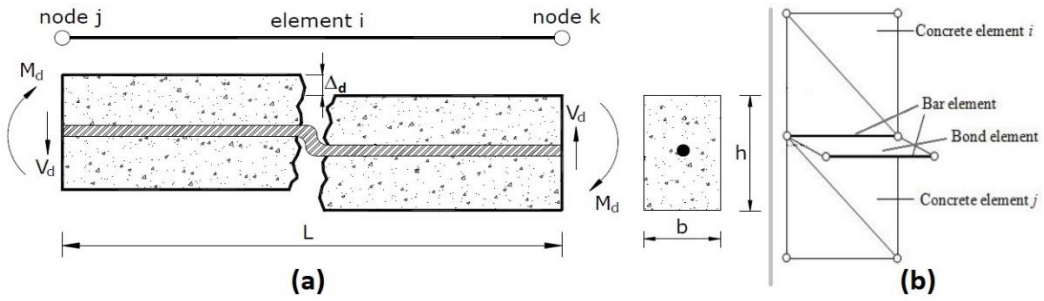

Figure 1.31 (a) Numerical representation of dowel action (Nogueira, Venturini and Coda 2013), (b) adjoining concrete elements (Kwan and Ng 2012).

Using the beam in elastic foundation theory presented previously, (He and Kwan 2001) expressed the dowel stress (τ_d) by using dowel displacement (Δ_d) and dowel force (V_d) as following:

$$\Delta_d = l_s \times \gamma_{12} \tag{1.42}$$

$$V_d = K_d \times \Delta_s \tag{1.43}$$

$$\tau_d = \frac{\rho_s}{A_s} \times V_d \tag{1.44}$$

where, l_s is the length of the steel bar element, γ_{12} is the shear strain perpendicular to the dowel bar, K_d is the dowel stiffness, ρ_s is the reinforcement ratio in the concrete direction and A_s is the sectional area of the steel bar.

Then, the dowel stress (τ_d) can be transformed into tensile (σ_1) and shear (τ_{12}) stresses using the given equations below:

$$\sigma_1 = \frac{\rho_s}{A_s} \times K_d \times l_s \times \varepsilon_1 \tag{1.45}$$

$$\tau_{12} = \frac{\rho_s}{A_s} \times K_d \times l_s \times \gamma_{12} \tag{1.46}$$

where, ε_1 is the tensile strain across the crack.

Combining the equations given above, the contribution of dowel action to the tensile and shear stresses across the crack can be obtained in 2D (for x and y directions) as following:

$$\begin{bmatrix}\sigma_1 \\ \tau_{12}\end{bmatrix} = [T_d]^t \begin{bmatrix}\frac{\rho_{sx}}{A_{sx}} K_{dx} l_{sx} & 0 \\ 0 & \frac{\rho_{sy}}{A_{sy}} K_{dy} I_{sy}\end{bmatrix} [T_d] \begin{bmatrix}\varepsilon_1 \\ \gamma_{12}\end{bmatrix} \tag{1.47}$$

$$T_d = \begin{bmatrix}\cos\theta\sin\theta & \cos^2\theta \\ \cos\theta\sin\theta & -\sin^2\theta\end{bmatrix} \tag{1.48}$$

where, T_d is the transformation matrix, θ is the angle of crack direction normal to the plane of crack and l_s is the length of the steel bar element for x and y directions of the steel bar.

(Kwan and Ng 2012) is modified the methodology of (He and Kwan 2001) for 3D numerical applications by including the dowel stiffness (K_d) in the two adjoining concrete elements around the steel element as in the Figure 1.31b. According to Figure 1.31b, the dowel displacement Δ_d can be written as Eq. 1.49 for the concrete element i.

$$\Delta_d = l_s \gamma_{12} [T_d][B_i][\delta_i] \tag{1.49}$$

where, B and δ are respectively the strain and displacement matrixes of adjoining concrete element (whether i or j as in the Figure 1.31b) and T_d is the transformation matrix in 3D.

with,

$$T_d = \begin{bmatrix} \cos^2\theta & \sin^2\theta & \cos\theta\sin\theta \\ \sin^2\theta & \cos^2\theta & -\cos\theta\sin\theta \\ -2\cos\theta\sin\theta & 2\cos\theta\sin\theta & \cos^2\theta - \sin^2\theta \end{bmatrix} \tag{1.50}$$

and

$$\gamma_{12} = [0 \quad 0 \quad 1] \tag{1.51}$$

where, θ is the angle of crack direction normal to the plane of crack and γ_{12} is the shear strain across the crack.

From the energy principle, dowel stiffness matrix (K_d) is derived as:

$$[K_d] = \alpha_i k_d {l_s}^2 [B_i]^T [T_d]^T \begin{bmatrix} 0 & 0 & 0 \\ 0 & 0 & 0 \\ 0 & 0 & 1 \end{bmatrix} [T_d][B] \tag{1.52}$$

and α is the distribution coefficient of the concrete area (whether i or j as in the Figure 1.31b) can be represented as:

$$\alpha_i = \frac{A_i}{A_i + A_J} \tag{1.53},$$

$$\alpha_j = \frac{A_j}{A_i + A_J} \tag{1.54}$$

where k_d is the dowel stiffness calculated from Eq. 1.35, A_i and A_j are the areas of the two adjoining concrete elements.

6. Conclusion

The bond-slip model by (Casanova, Jason and Davenne 2012) is an alternative approach to represent the effects of steel-concrete bond behavior in reinforced concrete structures associated to a finite element model. In this Chapter, some state of the art information is explained to highlight the objective of this study and the followed methodology.

As a state of the art, the steel-concrete interaction in reinforced concrete structures are generally explained and the importance of interface behavior to the crack properties is expressed. Then, numerical representation of the steel-concrete bond is expressed by defining several existing numerical models especially focusing on bond-slip model by (Torre-Casanova 2013). A background information is provided on the monotonic and cyclic bond behaviors. Subsequently, the confinement influence on the steel-concrete bond are briefly clarified for different confinement types. Eventually, dowel action and its importance to the shear resistance is explained.

According to the provided information within this Chapter, the following conclusions may be drawn:

- A detailed evaluation of the bond-slip model is necessary to utilize the model in industrial applications. Especially, transversal and irreversible behavior of the bond should be considered carefully to represent the local and global behavior of the reinforced concrete structures (Chapter 2).
- Moreover, external pressure (active confinement) is also an important parameter which affects the bond characteristics. The consideration of active confinement effect within the bond-slip model may improve the factual representation of local and global structural behavior (Chapter 3).

Dowel actions is an important parameter for the shear transfer especially at the crack location. On the other hand, its numerical representation or experimental detection are quite troublesome since dowel action occurs with other transfer components. Elaborate numerical investigations should be performed on the dowel action in order to understand its importance. Thus, bond-slip model by (Torre-Casanova 2013) is an effective model to capture the local behavior (crack properties) and might be used to investigate dowel action in reinforced concrete structures (Chapter 4).

Chapter-2:
Development of the Bond-Slip Model

1. Introduction

This Chapter is dedicated to the developments in the bond-slip model initially proposed by (Casanova, Jason and Davenne 2012) and (Mang, Jason and Davenne 2015). First of all, a general principle of the bond-slip model is presented in this Chapter to elucidate the model's methodology. Afterwards, the main focus was on analyzing the model and locating the deficiencies, refining it by a solution and then validating the new proposal. Generally, the simulations like pull-out tests and shear walls which were performed by mentioned authors are complex geometries. Since there are many parameters affecting the bond behavior, it is quite difficult to analyze only the bond-slip model's contribution in numerical calculations. For this reason, rather simple geometries like one single interface element are chosen to understand the acceptability and the numerical efficiency of the bond-slip model.

Mainly, two major anomalies are detected related with the transversal and irreversible bond behavior of the model separately. After the detection of those anomalies, different solutions are proposed, tested and then implemented in the source code. Namely, an alternative solution is proposed in order to obtain the transversal behavior of the bond and a completely new methodology is proposed to obtain the irreversible behavior of the steel-concrete bond under cyclic loading. Thereafter, the implementations are validated with several simulations on simple geometries. Since the bond-slip model is improved by several modifications, tangential bond behavior is also validated before performing any further analysis on complex geometries.

2. Bond-Slip Model

In this section, first the main principles of the bond-slip model are explained and then the detected anomalies are presented in detail.

2.1. Theoretical Presentation of the Model

Bond-slip model is a constitutive approach which has been proposed by (Torre-Casanova 2013) and to represent the effects of steel-concrete bond behavior in reinforced concrete structures associated to a Finite Element Model (FEM). The main principle is to define a zero thickness interface element between the steel and concrete as presented in the Figure 2.1. This is done via a simple methodology by creating a superimposed element on the 1D steel element. The superimposed element is strictly bounded to the concrete element by certain kinematic relations where it acts like the concrete cover.

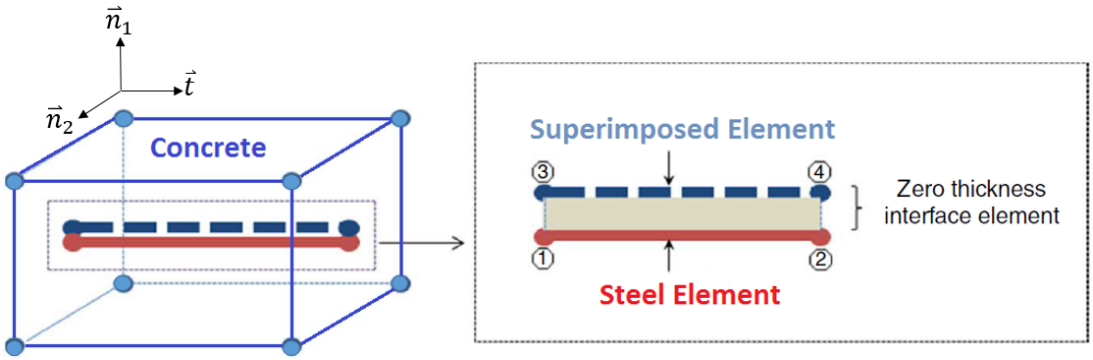

Figure 2.1 Representation of interface element (Mang 2016).

Then the bond characteristics (like adhesion law) are defined on the interface element by the user in order to calculate the bond stress. As it can be seen in Figure 2.2a the interface element consists of 4 nodes and each node has 3 degrees of freedom (DOF). Displacement {u} of the interface element nodes can be written as Eq. (2.1) below where t denotes the tangential direction along the steel bar, n_1 and n_2 denote the normal directions of interface nodes.

$$\{u\}^T = \{u_{1t}, u_{1n_1}, u_{1n_2}, u_{2t}, u_{2n_1}, u_{2n_2}, u_{3t}, u_{3n_1}, u_{3n_2}, u_{4t}, u_{4n_1}, u_{4n_2}\} \qquad (2.1)$$

From the displacement difference between the interface element nodes, the slip (δ_{node}) between steel and concrete can be easily calculated (Figure 2.2b) by using the Eq. (2.2) below.

$$\{\delta_{node}\} = \begin{bmatrix} I_3 & 0_3 & -I_3 & 0_3 \\ 0_3 & I_3 & 0_3 & -I_3 \end{bmatrix} \{u\} \qquad (2.2)$$

where

$$I_3 = \begin{bmatrix} 1 & 0 & 0 \\ 0 & 1 & 0 \\ 0 & 0 & 1 \end{bmatrix} \qquad (2.3), \qquad 0_3 = \begin{bmatrix} 0 & 0 & 0 \\ 0 & 0 & 0 \\ 0 & 0 & 0 \end{bmatrix} \qquad (2.4)$$

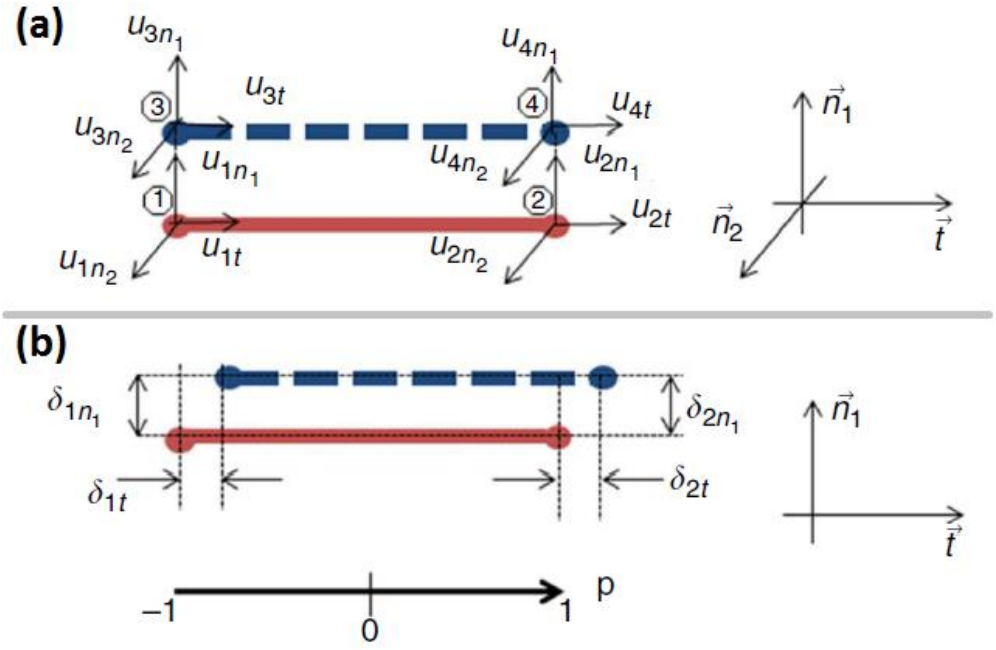

Figure 2.2 (a) degrees of freedom of an interface element, (b) definition of the slip within the interface element (Mang, Jason and Davenne 2015).

From Eq. (2.2), the slip can be represented by Eq. (2.5):

$$\{\delta_{\text{node}}\}^{\text{T}} = \{\delta_{1t}, \delta_{1n1}, \delta_{1n2}, \delta_{2t}, \delta_{2n1}, \delta_{2n2}\} \tag{2.5}$$

The generalized slip of the interface element is calculated as in Eq. (2.6):

$$\{\delta(\text{p})\} = \begin{Bmatrix} \delta_{\text{t}}(\text{p}) \\ \delta_{\text{n1}}(\text{p}) \\ \delta_{\text{n2}}(\text{p}) \end{Bmatrix} = [\text{B}_1(\text{p}) \quad \text{B}_2(\text{p})]\,\{\delta_{\text{node}}\} \tag{2.6}$$

where

$$\text{B}_1(\text{p}) = 0.5\,(1-\text{p})\text{I}_3 \qquad (2.7), \qquad \text{B}_2(\text{p}) = 0.5\,(1+\text{p})\text{I}_3 \tag{2.8}$$

$$-1 \le \text{p} \le 1 \tag{2.9}$$

Combining the equations 2.2 and 2.5, the slip can be written in terms of displacement as in Eq. (2.10):

$$\{\,\delta(\text{p})\,\} = \text{B}(\text{p})\;\{\text{u}\} \tag{2.10}$$

The generalized stresses $\{\sigma(\text{p})\}$ are written as in Eq. (2.11) which contains again 3 different components: 1 for tangential and 2 for normal directions.

$$\{\sigma(p)\} = \begin{Bmatrix} \sigma_t(p) \\ \sigma_{n_1}(p) \\ \sigma_{n_2}(p) \end{Bmatrix} \tag{2.11}$$

The stresses for the tangential direction can be calculated by a defined adhesion law (stress-slip relation) which is presented in Eq. 2.12. In the normal directions, a linear relation is assumed by defining the normal stiffness values (k_n) as constant as in Eq. 2.13. Usually the k_n values are chosen high enough to obtain perfect bond relation in the normal directions (n_1 and n_2).

$$\sigma_t(p) = f(\delta_t(p)) \tag{2.12}$$

$$\begin{Bmatrix} \sigma_{n1}(p) \\ \sigma_{n2}(p) \end{Bmatrix} = k_n \begin{Bmatrix} \delta_{n1}(p) \\ \delta_{n2}(p) \end{Bmatrix} \tag{2.13}$$

Besides, the nodal forces on the interface element for the 4 different nodes are represented as in Eq. (2.14).

$$\{F_{interface}\}^T = [F_1^T \quad F_2^T \quad F_3^T \quad F_4^T] \tag{2.14}$$

These forces on each interface element nodes can be calculated by Eq. (2.15) and Eq. (2.16) below by integrating the stresses (Eq. 2.13 and Eq. 2.13) of each node.

$$F_1 = \begin{Bmatrix} F_{1t} \\ F_{1n1} \\ F_{1n2} \end{Bmatrix} = \frac{\ell_{int}}{2} \int_{-1}^{1} A \{\sigma(p)\} dp \tag{2.15}$$

$$F_2 = \begin{Bmatrix} F_{2t} \\ F_{2n1} \\ F_{2n2} \end{Bmatrix} = \frac{\ell_{int}}{2} \int_{-1}^{1} A \{\sigma(p)\} dp \tag{2.16}$$

where ℓ_{int} is the length of the interface element and

$$A = \begin{bmatrix} \pi d_s & 0 & 0 \\ 0 & d_s & 0 \\ 0 & 0 & d_s \end{bmatrix} \tag{2.17}$$

with d_s the diameter of steel bar.

The following equations (2.18) and (2.19) can be obtained from the force equilibrium.

$$F_3 = \begin{Bmatrix} F_{3t} \\ F_{3n1} \\ F_{3n2} \end{Bmatrix} = -F_1 \qquad (2.18), \qquad F_4 = \begin{Bmatrix} F_{4t} \\ F_{4n1} \\ F_{4n2} \end{Bmatrix} = -F_2 \qquad (2.19)$$

For the resolution matrix, linearity of the stresses along the interface element is assumed. This choice allows an analytic integration of the nodal forces of the interface element from the stresses at each Gauss point. The generalized stresses can be written according to the stresses at the Gauss points (σ_{GP}) of the interface element as in Figure 2.3 in the local coordinates (t, n_1 and n_2):

$$\{\sigma(p)\} = [B_1(p) \quad B_2(p)]\, Q\, \{\sigma_{GP}\} \qquad (2.20)$$

with

$$\{\sigma_{GP}\}^T = \{\sigma_{GP1t} \quad \sigma_{GP1n1} \quad \sigma_{GP1n2} \quad \sigma_{GP2t} \quad \sigma_{GP2n1} \quad \sigma_{GP2n2}\} \qquad (2.21)$$

$$Q = \begin{bmatrix} B_1(a_{GP1}) & B_2(a_{GP1}) \\ B_1(a_{GP2}) & B_2(a_{GP2}) \end{bmatrix}^{-1} \qquad (2.22)$$

$$a_{GP1} = -\frac{1}{\sqrt{3}} \qquad (2.23), \qquad a_{GP2} = \frac{1}{\sqrt{3}} \qquad (2.24)$$

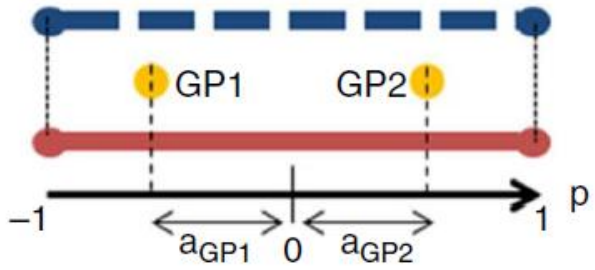

Figure 2.3 Positions of Gauss points in the interface element (Mang, Jason and Davenne 2015).

Using the defined formulations above, the nodal forces in the global coordinates (Figure 2.4) can be expressed as in the Eq. 2.25.

$$\{F\} = \begin{Bmatrix} F_1 \\ F_2 \\ F_3 \\ F_4 \end{Bmatrix} = T_{L\to G}\ C\ Q\{\sigma_{GP}\} \qquad (2.25)$$

where:

$$T_{L\to G} = \begin{bmatrix} T_1 & 0_3 & 0_3 & 0_3 \\ 0_3 & T_1 & 0_3 & 0_3 \\ 0_3 & 0_3 & T_1 & 0_3 \\ 0_3 & 0_3 & 0_3 & T_1 \end{bmatrix} \tag{2.26}$$

$$T_1 = \begin{bmatrix} x.t & x.n_1 & x.n_2 \\ y.t & y.n_1 & y.n_2 \\ z.t & y.n_1 & z.n_2 \end{bmatrix} \tag{2.27}$$

and

$$C^T = [C_1^T \quad C_2^T \quad -C_1^T \quad -C_2^T] \tag{2.28}$$

$$C_1 = l_e A \left[\frac{3I_3}{8} \; \frac{I_3}{8}\right] \tag{2.29}$$

$$C_2 = l_e A \left[\frac{I_3}{8} \; \frac{3I_3}{8}\right] \tag{2.30}$$

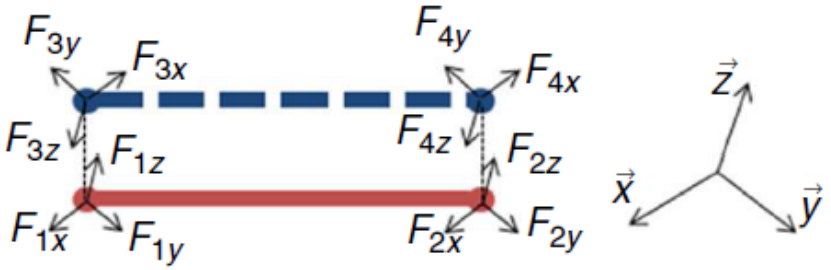

Figure 2.4 Nodal forces of the interface element in the global coordinate system (Mang, Jason and Davenne 2015).

2.2. Anomalies of the Model

The anomalies which are detected during the analysis of the bond-slip model basically can be grouped into two categories: transversal and irreversible bond behaviors. In this section, these anomalies are explained in detail.

Transversal Behavior

In the previous studies like (Torre-Casanova 2013) and (Mang 2016), the bond-slip model was mainly focused on the tangential behavior of the bond. First series of test simulations have been performed on a single interface element with the bond-slip model in order to investigate also the behavior in the normal direction. A 2 cm length (l_{int}) single interface element without any thickness is considered with a steel bar diameter $d_S = 1$ cm as in Figure 2.5. The bottom line of the element is blocked against any displacement as a boundary condition and 5 mm

displacement is applied on the top nodes in Y or Z direction (normal directions) separately. A linear bond stress-slip relation is assumed both in tangential (X) and normal directions (Y and Z) with the defined stiffness values (k_t, k_{n1} and k_{n2}). Tangential stiffness (k_t) is taken equal to $1.10^{12}\mathrm{Pa/m}$ and the normal stiffness values (k_{n1} and k_{n2}) are defined to be the same in both normal directions as $1.10^{15}\mathrm{Pa/m}$.

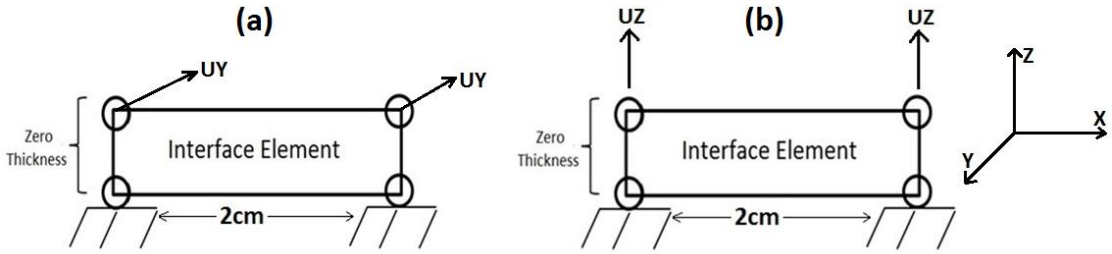

Figure 2.5 Representation of the interface element geometry for the 2 different test cases.

The calculation results revealed a particular problem that had not been noticed before in the calculation of the forces in normal directions of the interface element. When displacement is imposed in Y direction as in Figure 2.5a, the ultimate nodal force is calculated as 1.10^{10} N for both of the normal directions (Y and Z) even though no displacement was applied on Z direction. When displacement is imposed in Z direction (Figure 2.5b), the ultimate forces in both of the normal directions are calculated as zero. Based on these results, the source files of the bond-slip model are subsequently analyzed to determine the abnormalities in the bond-slip model (Table 2.1).

Table 2.1 Ultimate force values on interface element for initial and modified model.

Type of the model	**Imposed Displacement**	**Ultimate Force (F_u)**		
		$F_{u,x}$(N)	**$F_{u,y}$(N)**	**$F_{u,z}$ (N)**
Initial Bond-slip Model	5 mm Y-direction	0	1.10^{10}	1.10^{10}
	5 mm Z-direction	0	0	0

As a sum up, a deficiency is thus detected in the calculation of the forces in the normal directions of the joint element.

Irreversible Behavior

Second series of simulation are focused on the irreversible behavior of the bond-slip model. The cyclic adhesion law of the bond-slip model defined and implemented by (Mang 2016) has been tested with several simulations. Indeed, only the frictional force between steel and concrete remains in the tangential direction after several loading cycles. Understanding of this

phenomenon is quite important to predict the general response of a reinforced structure under cyclic loading, especially when the crack properties are considered.

The irreversible bond behavior of the bond-slip model is investigated for different alternative loadings to test its validity. In order to concentrate only on the bond behavior, once again, the single interface element geometry is chosen for the numerical analysis. Figure 2.6 represents a 2 cm length zero thickness interface element geometry with 1 cm diameter (d_S). The bottom nodes are blocked against displacement and the alternative load is applied on one of the top nodes as an imposed displacement (u_x). All of the simulations for the irreversible bond behavior analysis are performed on this single interface element.

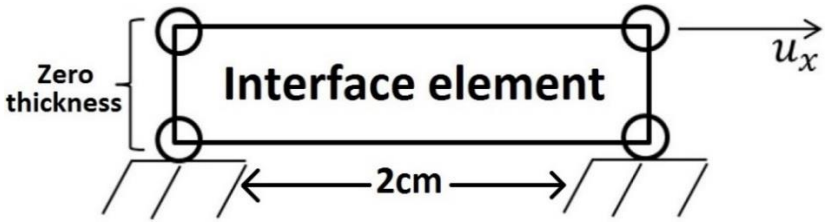

Figure 2.6 Representation of the interface element geometry.

Incremental Alternative Loading Test

For the first analysis, the same test case which was defined by (Mang 2016) is performed using the same parameters. An incremental cyclic displacement along the tangential direction (u_x) is imposed on one node of the single interface element (Figure 2.6) with a loading history as shown in Figure 2.7a and the adhesion law that is defined as shown in Figure 2.7b. The properties of the adhesion curve are given in Table 2.2.

Table 2.2 Bond Properties

Elastic Limit Stress τ_0 (MPa)	Maximum Strength τ_u (MPa)	Frictional Stress τ_0 (MPa)
2	20.8	2

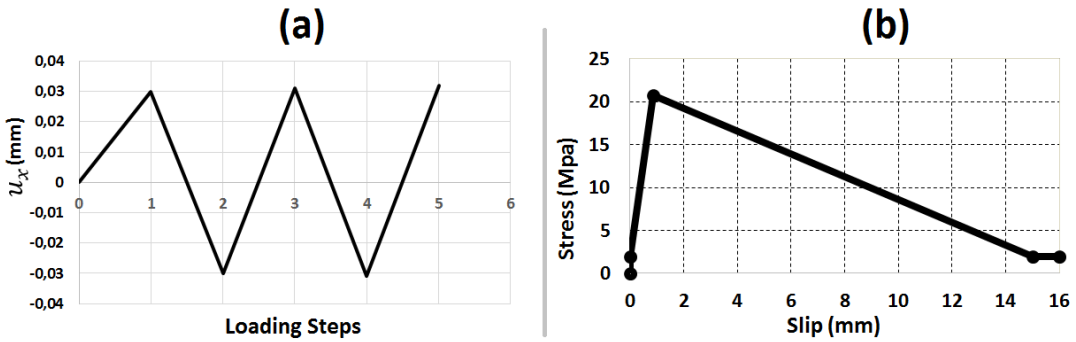

Figure 2.7 (a) History of imposed displacement. (b) Adhesion law of the interface between the steel and concrete.

The response stress-slip curve is presented in Figure 2.8. The irreversible behavior is presented in the pre-peak stage of the adhesion law. Normally, the stress values should follow the A – B path until the last maximum stress value B and then it should follow the defined adhesion law along the B-C path instead of. A-A'-C path in Figure 2.8. There are a few steps between the points A and A´ which do not represent the intents of the model. To sum up, there should not be any distance between the points A-A´ and B-C in the reloading stage. This problem should be straightened out for the realistic calculations.

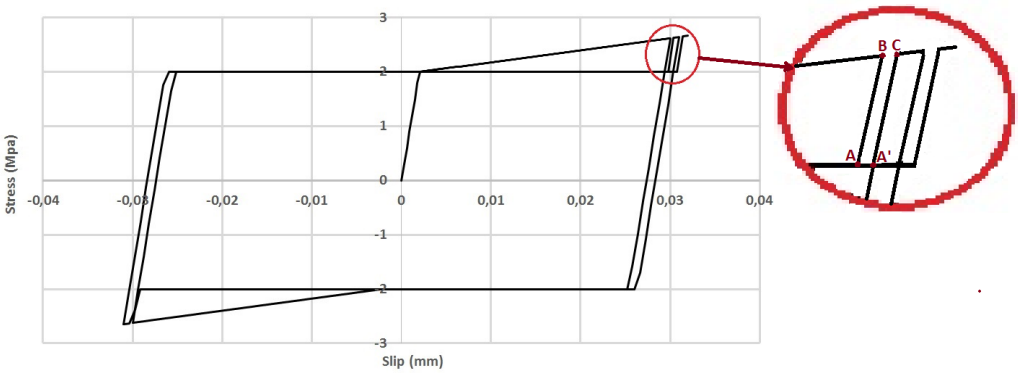

Figure 2.8 Stress-slip curve of the interface element under cyclic loading.

Analysis of the Frictional Stress

As stated earlier, friction between the steel and concrete is taking a part in the reloading stage when a cyclic loading is considered. In the bond-slip model of (Mang 2016), this frictional stress is considered as equal as the elastic limit stress (τ_0). However, in reality, the frictional stress varies depending on many parameters like geometry and material properties of the structures (Park and Paulay 1975). That is why it may be necessary to define bonding laws with different friction stresses (τ_f) according to the selected numerical applications.

For the second test case, friction stress effect on the bond behavior is tested again on a single interface element (Figure 2.6) with identical geometry, loading and boundary condition as in the previous test case. Only 1 MPa frictional stress value (τ_f) at the end of the loading is defined in the input adhesion law instead of 2 MPa. The loading history and defined adhesion low are given in Figure 2.9a and b. The properties of adhesion curve are presented in Table 2.3.

Table 2.3 Bond Properties

Elastic Limit Stress τ_0 (MPa)	Maximum Strength τ_u (MPa)	Frictional Stress τ_f (MPa)
2	20.8	1

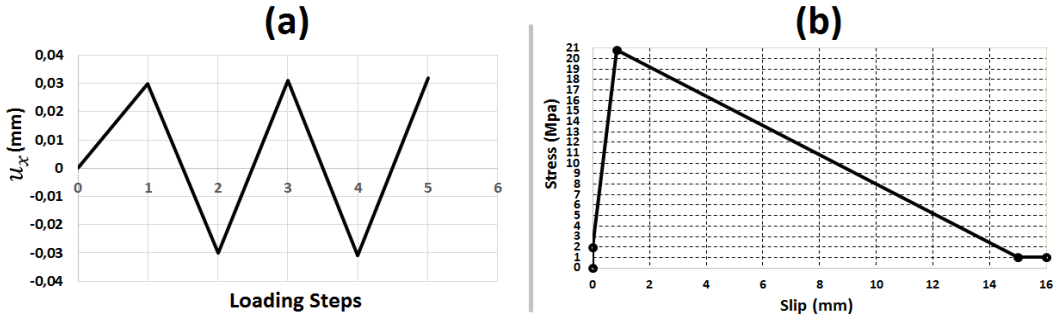

Figure 2.9 (a) History of imposed displacement. (b) Adhesion law of the interface between the steel and concrete.

The response bond stress-slip curve is presented in Figure 2.10. Two different anomalies are detected according to the results.

The first one is related with the correct follow up of the defined adhesion law during the loading phase which can be seen in the right top corner of Figure 2.10. In reality, the stress-slip curve should follow the A-B-C path instead of A-A′-C path. This problem originates from the identical anomaly which is explained in the previous section, but we remark that τ_f has an influence on the shape of this anomaly.

The second anomaly is related with the defined frictional stress (τ_f) between the steel and concrete. It can be observed that the bond-slip law is not correctly implemented, a stress jump can be seen between the points D′ and E in Figure 2.10. In reality, the curve should follow the D-E line for the loading instead of D-D′-E path (Figure 2.10). The program makes a confusion between the first loading until the elastic limit (τ_0) and the reloading following a horizontal line at the value of the frictional stresses (τ_f). This incoherent results cannot be observed if $\tau_0=\tau_f$. Therefore, this problem should be corrected as well.

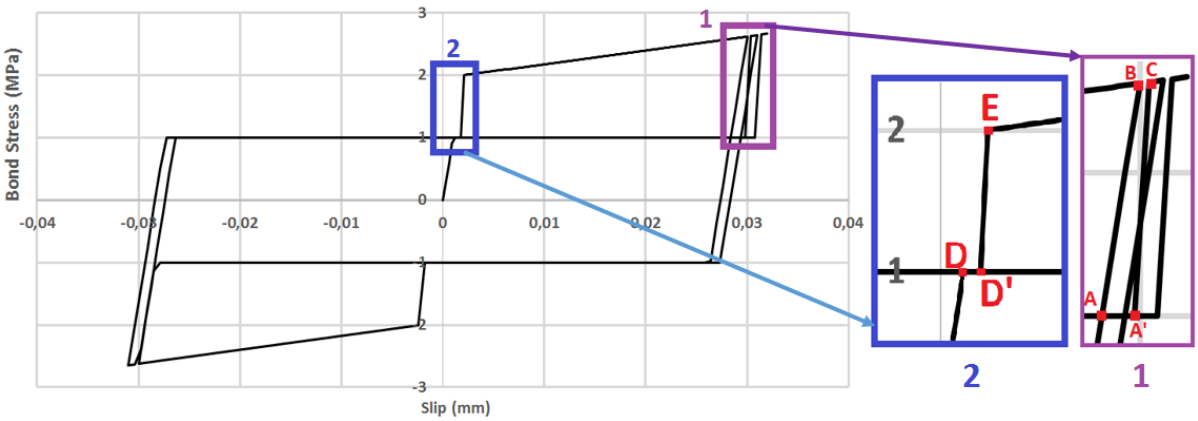

Figure 2.10 Stress-slip curve of the interface element under cyclic loading for 1MPa frictional stress between the steel and concrete.

Analysis of the Adhesion Law

So far, a classical adhesion law is used in numerical analysis which is proposed by (Torre-Casanova 2013). This law is a non-linear law defined by four straight lines: elastic, pre-peak, post-peak and residual friction phases (Figure 2.7b). In the engineering applications, the bond characteristics can be can be mutative depending on the material and geometric properties of the reinforced structures. Therefore, it is necessary to be able to use various adhesion laws in bond-slip model for the numerical analysis.

In the third test, the bond-slip model dependence on the adhesion law is examined again on the single interface element (Figure 2.6) by applying cyclic loads. The availably of using different adhesion laws is tested. A particular adhesion law (with multiple straight lines) is defined (Figure 2.11b) which has a weaker bond strength ($\tau_u = 15$ MPa) and higher frictional stress ($\tau_f = 7$ MPa). The imposed displacement is chosen as in Figure 2.11a so that the behavior of the steel-concrete bond can be observed in the different phases (elastic, before and after the peak). The characteristics of the defined adhesion curve are given in Table 2.4.

Table 2.4 Bond Properties

Elastic Limit Stress τ_0 (MPa)	Maximum Strength τ_u (MPa)	Frictional Stress τ_f (MPa)
1	15	7

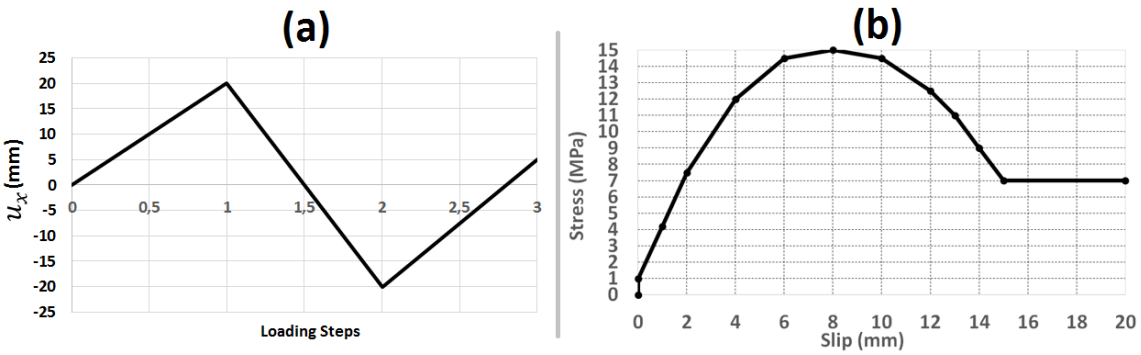

Figure 2.11 (a) History of imposed displacement. (b) Adhesion law of the interface between the steel and concrete.

The bond stress slip values after the test simulation is illustrated in Figure 2.12. Again, there is a confusion between the elastic limit stress and the friction stress which are different here. This leads to an error between first loading and reloading in the reverse direction (change of sign of loading). The stress drop between F and F' could bring numerical difficulties. Even if it not the true physical reality, a straight direct path from F to G on Figure 2.12 would be better.

The modification of implementation of (Mang 2016)'s bond-slip model is necessary for the utilization of different adhesion laws.

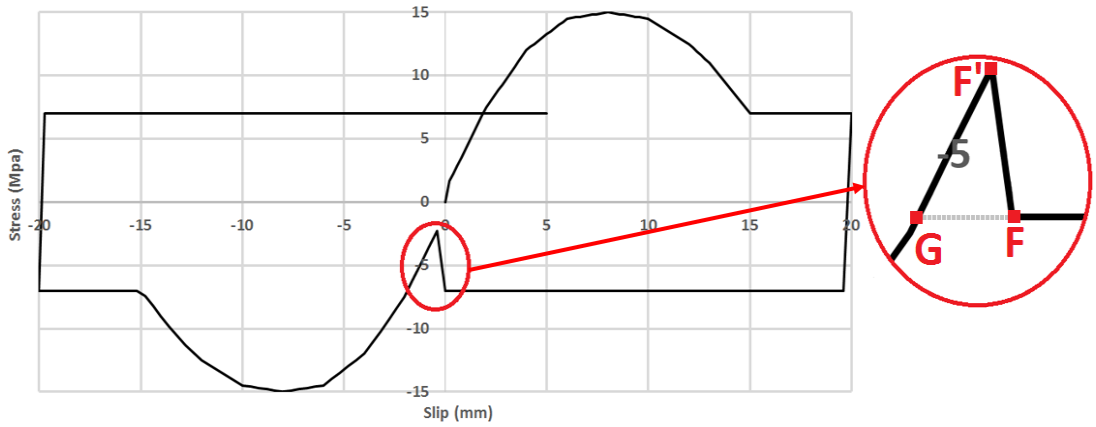

Figure 2.12 Stress-slip curve of the interface element under cyclic loading for different adhesion law.

All the anomalies inside the irreversible law of bond-slip model can be summarized as follows:

- When the loading exceeds the maximum load in history, the stress does not correctly follow the adhesion law which is defined by the user.
- If the user defines a friction stress different from the elastic limit stress, some anomalies appears in the response: at the first loading if $\tau_0 > \tau_f$, and at the reverse loading if $\tau_0 < \tau_f$

After examining the source code of the cyclic adhesion law, and considering the results of the three test cases carried out above, it came out that the problem was originated in the definition of every load-reload possibility of the system depending on the values of τ_0 and τ_f. Therefore, a completely new methodology is suggested to represent the irreversible behavior of the bond which can be adapted to any case. This new irreversible bond model will be explained in detail in the following section.

3. Implementation of the New Model

In this section, the implementation and the validation of the new bond-slip model is explained in detail.

3.1. Transversal behavior of the bond

The detected anomaly related with the transversal bond behavior is already elaborated in section 2.2. It has been recorded that when the displacement is imposed to Y normal direction, the nodal forces are calculated in both directions (Y and Z) and when the displacement is imposed to Z normal direction, the nodal forces are calculated zero in both directions (Y and Z).

After thoroughly examining the source codes, it has been conceived that there was a kind of problem originating from integration of the forces. Inside the source codes the global forces on the interface element nodes (for 3D case) are assumed to be the same both in Y and Z directions. In actual applications, it can be different according to the applied load characteristics. This anomaly is retrieved by a new numerical integration methodology that is implemented inside the model to be able to consider the force calculation in Y and Z directions separately. The nodal and local forces are shown together in Figure 2.13.

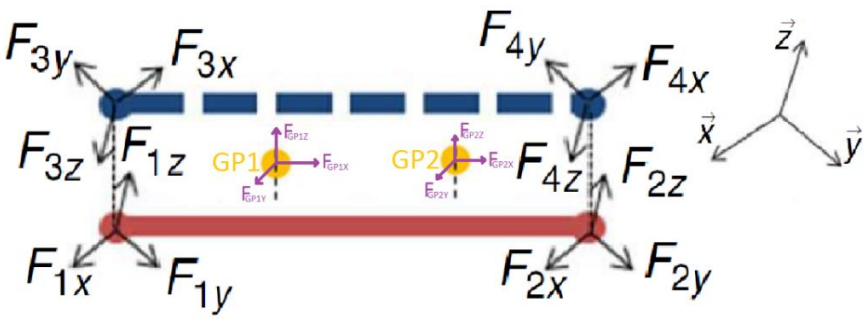

Figure 2.13 Representation of the forces on the Gauss points and the nodal forces on the interface element.

The numerical formulations that are implemented inside the model for the calculation of the nodal forces are defined as follows:

$$F_{1x} = F_{GP1x} \times \alpha_{xx} + F_{GP1y} \times \alpha_{xy} + F_{GP1z} \times \alpha_{xz} \quad (2.31)$$

$$F_{1y} = F_{GP1y} \times \alpha_{yx} + F_{GP1y} \times \alpha_{yy} + F_{GP1z} \times \alpha_{yz} \quad (2.32)$$

$$F_{1z} = F_{GP1z} \times \alpha_{yx} + F_{GP1y} \times \alpha_{zy} + F_{GP1z} \times \alpha_{zz} \quad (2.33)$$

$$F_{2x} = F_{GP2x} \times \alpha_{xx} + F_{GP2y} \times \alpha_{xy} + F_{GP2z} \times \alpha_{xz} \quad (2.34)$$

$$F_{2y} = F_{GP2y} \times \alpha_{yx} + F_{GP2y} \times \alpha_{yy} + F_{GP2z} \times \alpha_{yz} \quad (2.35)$$

$$F_{2z} = F_{GP2z} \times \alpha_{yx} + F_{GP2y} \times \alpha_{zy} + F_{GP2z} \times \alpha_{zz} \quad (2.36)$$

where, F_1, F_2, F_3, F_4 are the nodal forces and $F_{GP1,}$ F_{GP2} are the local forces in the Gauss points along the X, Y and Z directions. The alpha (α) values represents the transition between the local to global coordinate system (see eq 2.26 and 2.27). By the use of the forces equilibrium criteria, the nodal forces of the 3rd and 4th nodes can be written as follows:

$$F_{3x} = -F_{1x} \quad (2.37), \qquad F_{3y} = -F_{1y} \quad (2.38), \qquad F_{3z} = -F_{1z} \quad (2.39)$$

$$F_{4x} = -F_{2x} \quad (2.40), \qquad F_{4y} = -F_{2y} \quad (2.41), \qquad F_{4z} = -F_{2z} \quad (2.42)$$

Interface Element Test

The same numerical analyses as depicted in Figure 2.5 are performed once again with the modifications after the implementation of the new formulas. The results before and after modifications are compared with each other. Ultimate forces on the interface element are presented in Table 2.5 to point out the new improvements.

Table 2.5 Ultimate force values on interface element for initial and modified models.

	Imposed Displacement	**Ultimate Force (F_u)**		
		$F_{u,x}$(N)	**$F_{u,y}$(N)**	**$F_{u,z}$ (N)**
Before modification	5 mm-Y direction	0	1.10^{10}	1.10^{10}
	5 mm-Z direction	0	0	0
After modification	5 mm-Y direction	0	1.10^{10}	0
	5 mm-Z direction	0	0	1.10^{10}

As can be seen in Table 2.5, the forces are calculated as zero in the initial model when 5 mm displacement is imposed in the normal direction Z. Since the integration of the forces in global coordinate system were not formulized properly, the forces are calculated as zero at the end of each step. After the implementation of adequate methodology in the calculation of forces, it can be seen that the forces are calculated accurately on the interface element which can also be verified with the simple analytical solution below. The general relation between stress (σ_n) and displacement (δ_n) along the normal directions can be written as in Eq. (2.43):

$$\sigma_n = k_n \times \delta_n \tag{2.43}$$

where, k_n denotes the normal stiffness with a constant value ($k_n = 1.10^{15}$ Pa/m), the ultimate forces (F_u) can be calculated directly from Eq. (2.44) for both of the normal directions.

$$F_{u,n} = \int (\sigma_n)\, dS_{int} = \sigma_n \times l_{int} \times d_S \tag{2.44}$$

where, S_{int} is the surface area of the interface element, l_{int} is the interface element length and d_S is the diameter of the steel bar.

When proper values are placed into the equations, the ultimate stresses are found equal to 1.10^{10} Pa/m in both normal directions, which verify the numerical analysis results. The reason of obtaining the same ultimate force values in both simulations is due to assumption of same stiffness values ($k_{n1} = k_{n2} = 1.10^{15}$ Pa/m) and same imposed displacements in Y and Z directions.

The next step is to test the modified bond-slip model's performance on a reinforced concrete geometry in order to analyze the global behavior of the structure.

Interface Element with Concrete Cover

After the implementation of the new methodology for the calculation of the nodal forces in normal directions, the second series of numerical analyses have been performed in order to validate the model. Simulations are implemented on a more generic case like a concrete cover on a steel bar, and by the bond slip-model representing an interface between them. The concrete cover is represented as a cubic element with a total volume of 1 m^3 around the steel. A 1 m long steel bar is placed in the center of the cube with the diameter (d_s) of 1 cm. A zero-thickness joint element is defined between the concrete (superimposed beam element) and the

steel bar. A linear bond stress-slip relation is assumed for tangential and transversal directions of the interface. Tangential stiffness value is taken as $k_t = 1.10^{12}$ Pa/m and normal directional stiffness value is taken as $k_n = 1.10^{15}$ Pa/m. Total elasticity is assumed for the steel and concrete. The material properties of steel and concrete are presented in Table 2.6. Boundary conditions and mesh geometry for the aforementioned numerical analysis are summarized in Figure 2.14 and Figure 2.15. 5 mm displacement (U_Z) is imposed at the end of the steel bar (point PA2) throughout the positive Z direction. The bottom surface of the cube element (S1) is blocked against any displacement as a boundary condition. The new bond-slip model's validity is examined for the numerical applications of reinforced concrete structures with this simulation.

Table 2.6 Material properties of steel and concrete.

	Poisson Ratio	Young Modulus (GPa)
Steel	0.3	200
Concrete	0.2	25

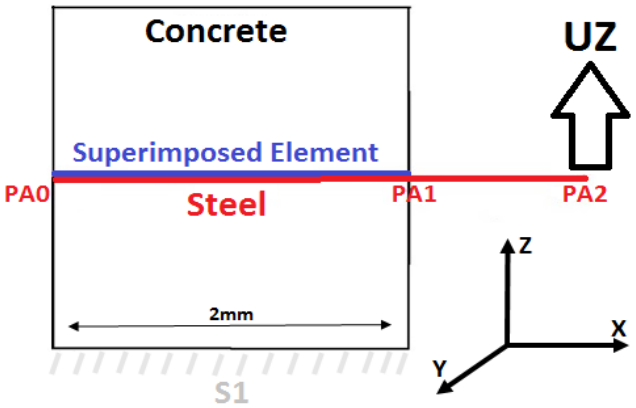

Figure 2.14 Representation of the reinforced concrete box geometry with interface element for 2 test cases.

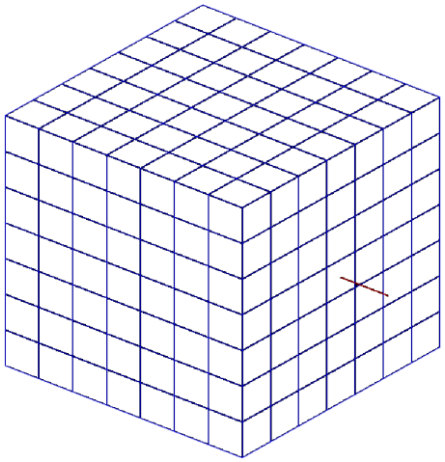

Figure 2.15 Mesh geometry of the reinforced concrete box for 2 test cases.

Numerical simulations are performed with initial and modified bond-slip models. As expected, the forces are calculated as zero on the superimposed element and concrete element nodes for the initial model simulation due to the miss-integration of the normal directional forces. With the implemented modifications, the forces in the interface element acting on the concrete element are calculated in a proper way. The stress transfer between steel and concrete are considered correctly with the modified bond-slip model. The ultimate force values of all simulations can be found in Table 2.7.

Table 2.7 Ultimate stress values of steel with concrete cover for modified and initial model.

Type of the model	**Imposed Displacement**	**Ultimate Force (F_u)**		
		$F_{u,x}$(N)	$F_{u,y}$(N)	$F_{u,z}$ (N)
Before modifications	5 mm Z-direction	0	0	0
After modification	5 mm Z-direction	0	0	2.84×10^7

3.2. Irreversible Behavior of the Bond

It was mentioned in section 2.2 that the proposed irreversible bond model had some anomalies related with the reloading stage, frictional forces and different adhesion laws defined by the user. Firstly, the source code is profoundly analyzed in order to understand the irreversible bond behavior within the model. After the evaluation of the source codes, it has been found out that the initially proposed model has been defined for all the loading-reloading scenarios for a single adhesion law. This model contains many loading-reloading cases and cannot be applicable for different adhesion laws. It cannot be used, especially for the conditions where the modification of the adhesion law is necessary like active confinement effect on the bond behavior. Because of the mentioned reasons above, a completely new irreversible bond model is suggested instead of modifying the previous version. The new irreversible model is more generalized compared to the initial one with less loading-reloading cases and can be applicable for different adhesion laws which can be defined by the user. The frictional stress between the steel and concrete is included as an additional parameter in the new cyclic model. Yet, the proposed cyclic model is validated on a single interface element by comparing the initial model on the same test cases.

New cyclic bond model

The methodology of the new irreversible bond model is detailed in this section.

The logic of the new irreversible bond-slip model can be easily explained by considering a single interface element application (Figure 2.16). In order to simplify the model methodology, the slip along the tangential direction of the steel bar (t_+) is assumed as the positive direction as presented in the Figure 2.16a. On the other hand, the opposite tangential direction of the steel element (t_-) is assumed as negative direction as in Figure 2.16b.

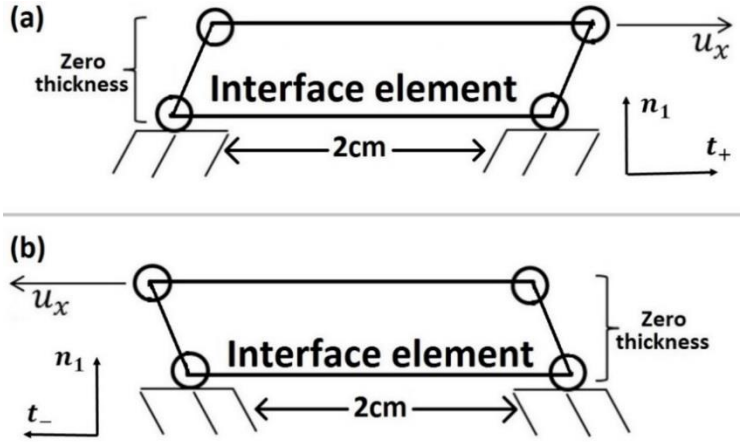

Figure 2.16 Representation of (a) loading in the positive tangential direction (t_+) and (b) re-loading in the negative tangential direction (t_-) of the interface element.

For each loading step, the loading directions are determined within the model. Determining the loading direction (t_+ or t_-) eliminates half of the possibilities automatically in the beginning of each calculation step. The program stores only the current slip value (s) and the maximum slip values in both directions (s_{maxp} and s_{maxn}) as represented in Figure 2.17.

According to the program logic, if the current slip value (s) is not in between the maximum slips in the loading history ($s > s_{maxp}$ or $s < s_{maxn}$), it follows the monotonic law which is defined by the user. On contrary, if the slip value (s) is in between the values s_{maxn} and s_{maxp}, then the bond behavior is in the cyclic region. Within the cyclic region, 3 different cases are considered:

- The first case is the elastic region which is presented in Figure 2.17 between the slip values s_n and s_p where elastic bond behavior is observed.

- Second case is the stress jump when the loading direction is changed (between t_+ and t_-) which is presented in Figure 2.17 between the slip values $s_{maxp} - s_{maxp1}$ or $s_{maxn} - s_{maxn1}$.
- Third case is the reloading case where only the frictional stress (τ_f) is active which is presented in the Figure 2.17 between the slip values $s_p - s_{maxp}$ or $s_n - s_{maxn}$.

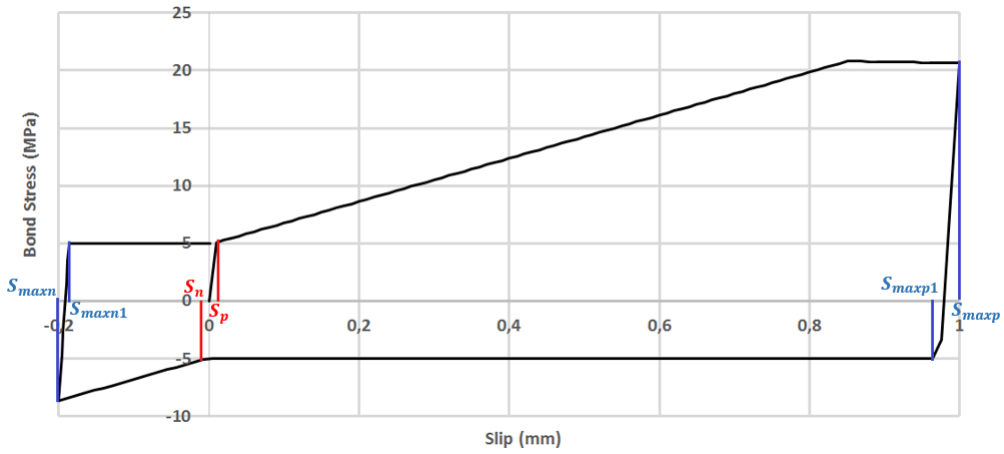

Figure 2.17 Example of the cyclic bond behavior in both directions (t_- and t_+).

The new irreversible bond model is a more generalized model compared to the previous one (with less cases for the cyclic behavior). Since the program considers less cases by eliminating method for each loading step of the numerical calculation, the computation time is decreased compared to the initial model for the presented tests in the section 2.2. Then for the initial model, the friction stresses are assumed equal as the elasticity limit of the bond. In the new irreversible model, the frictional stress is independently defined from the elastic limit of the bond, which makes it possible for users to define different values for both limits. The new irreversible bond-slip model is also applicable for different adhesion laws which may be defined by the user. This provides a possibility to modify the adhesion law in the beginning or during the numerical calculation if demanded. In order to enlighten the methodology explicitly, schematic representation of the program is also given in Figure 2.18.

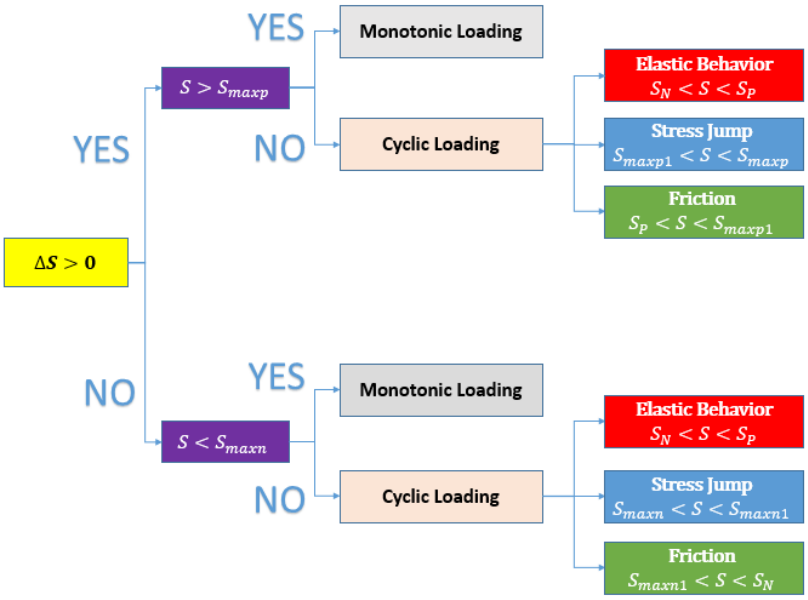

Figure 2.18 Schematic representation of the program logic.

The new irreversible bond model is tested on several simulations on the single interface element (Figure 2.6) for distinct loading types, frictional stresses and adhesion laws. The same test cases on the initial model which were presented in section 2.2 are reproduced with the new bond-slip model to disclose the amendments.

Incremental Alternative Loading Test

Antecedently, the same test simulation proposed by (Mang 2016) which is presented in section 2.2 is performed with the new irreversible bond model. Interface element geometry (Figure 2.6), imposed displacement (Figure 2.7a) and the adhesion law (Figure 2.7b) are chosen identical with the previous test case. Stress-slip curve of the simulation is illustrated in Figure 2.19.

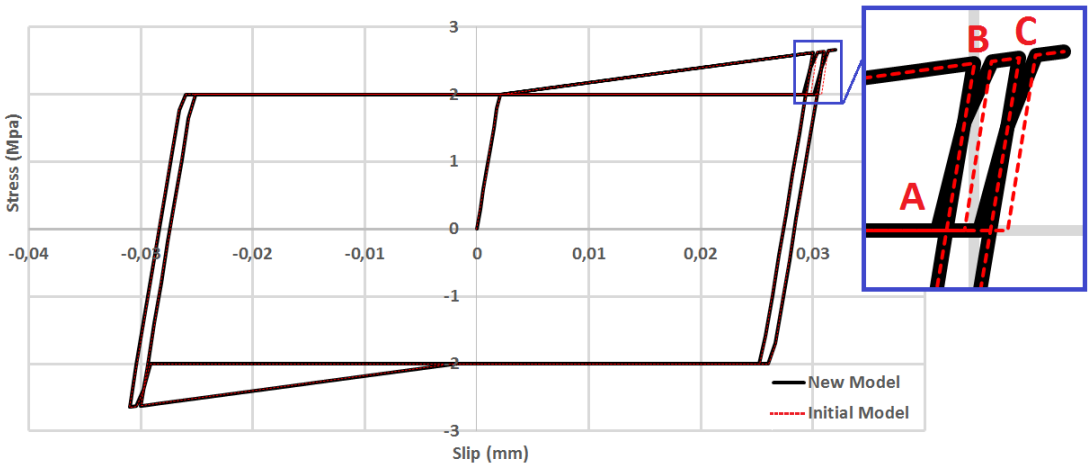

Figure 2.19 Stress-slip curve of the interface element under cyclic loading.

Figure 2.19 shows that the bond behavior follows the defined adhesion law for both loading and reloading phases. Moreover, for this case, the calculation time is reduced by 16% with the new irreversible bond-slip model against the initial model for exactly the same simulation.

Analysis of the Frictional Stress

For the second test case, exactly the same simulation represented in section 2.2 is performed on the single interface element (Figure 2.6) for the exact imposed displacement (Figure 2.9a) and adhesion law (Figure 2.9b) with the new irreversible bond model in order to examine the bond friction. Stress-slip curve of the simulation is illustrated in Figure 2.20.

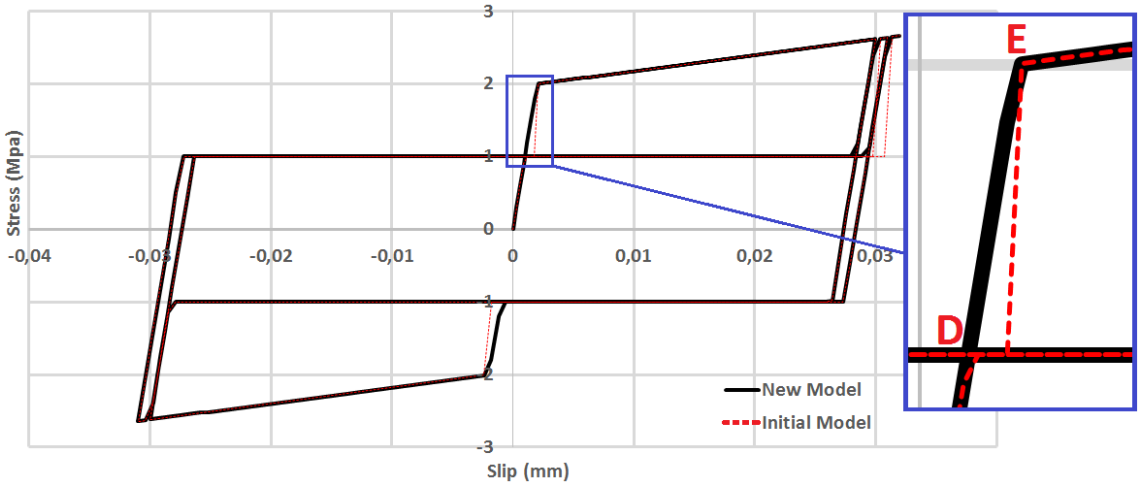

Figure 2.20 Stress-slip curve of the interface element under cyclic loading for 1MPa frictional stress between the steel and concrete.

The new irreversible model considers the elasticity limit (2MPa) and the frictional stress (1MPa) separately and performs the calculations according to this phenomenon. Since the frictional stress is considered separately inside the program, there is no interruption between the points D and elasticity limit E as it can be seen from Figure 2.20 in the initial loading phase contrary to the behavior of initial program which was presented in Figure 2.10. The calculation time is again reduced by 17% in the new model against the initial one for exactly the same simulation.

Analysis of the Adhesion Law

For the third test case, exactly the same simulation represented in section 2.2 is performed on the single interface element (Figure 2.6) for the exact imposed displacement (Figure 2.11a) and

adhesion law (Figure 2.11b) with the new irreversible bond model in order to examine the influence of the adhesion law. Stress-slip curve of the simulation is illustrated in Figure 2.21.

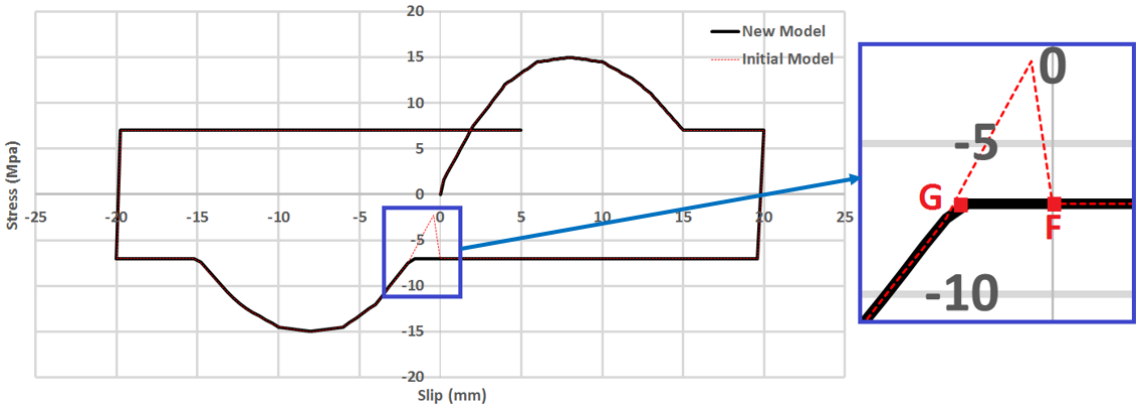

Figure 2.21 Stress-slip curve of the interface element under cyclic loading.

It can be seen from Figure 2.21 that the different adhesion laws are applicable for the new irreversible bond model. The interconnection between the points F and G can be seen in Figure 2.21 which is contrary to the situation in Figure 2.12 for the same test case with the initial model for the unloading phase. The new irreversible model calculates the intersection point G according to the defined adhesion law and friction stress values and considers this for both loading/unloading phases. Moreover, the calculation time is reduced by about 15% in the new irreversible model against the initial one for the identical test case.

4. Analytical Validation of the New Bond-Slip Model on a Tie-Rod

This section is dedicated to the validation of the new bond-slip model's outcomes in tangential direction by the comparison of numerical calculations with the analytical ones. Since there were several anomalies detected related with the bond-slip model and the model improved by implementing tangential and cyclic bond behavior, it has been decided to do an analytical validation of the model to be certain about the model's response before performing any further analysis. To accomplish this, a simple test on a tie rod which was previously studied by (Torre-Casanova 2013) and (Mang 2016) is considered. The analytical solution for the pull-out test geometry which is proposed by (Torre-Casanova, Jason, et al. 2013) is compared with the numerical simulations in order to validate the tangential behavior of the bond. The slip and stress distribution on the materials are analytically calculated for the defined case and compared with the numerical results of the developed bond-slip model simulations. Different tangential

stiffness values are also evaluated in bond-slip model and compared with the perfect bond hypothesis. Consequently, the bond-slip model is validated for the tangential direction.

For the pull-out test geometry, a tie rod embedded inside a concrete beam is chosen which is presented in Figure 2.22. Steel rod is tied at one end and 27.3 kN force (F_x) is applied on the other end in the tangential direction. The steel bar is embedded inside a 1.15m length (L) concrete beam which has $0.01\ m^2$ cross-sectional area (A_c). The steel diameter (d_s) is equal to 1 cm and it has a $7.85 \times 10^{-5}\ m^2$ cross-sectional area (A_s). A linear relation is used between stress and slip along the tangential axis in order to facilitate the analytical solution. The steel and concrete properties are provided in Table 2.8. Numerical and analytical surveys are performed according to these properties.

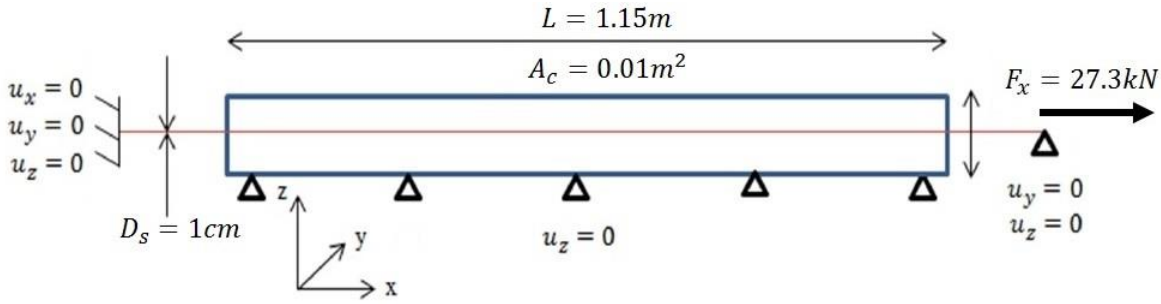

Figure 2.22 Presentation of the tie rod, boundary conditions and loading (Mang 2016).

Table 2.8 Material properties of steel and concrete (Mang 2016).

Steel Properties		**Concrete Properties**	
Young Modulus E_s (GPa)	**Poisson Ratio ν_s**	**Young Modulus E_c (GPa)**	**Poisson Ratio ν_c**
210	0.3	30.2	0.2

Analytical solution

In the analytical solution, for stress in steel σ_s, for stress in concrete σ_c and for slip δ_t equivalents are taken from the study of (Torre-Casanova 2013) and (Mang 2016) for the given geometry. The formulation of these is given below:

$$\sigma_s(x) = \left(\frac{F}{S_s} + \frac{\beta}{\alpha^2}\right)\frac{\cosh(\alpha x)}{\cosh\left(\frac{\alpha L}{2}\right)} - \frac{\beta}{\alpha^2} \qquad (2.45)$$

$$\sigma_c(x) = \frac{bE_C}{\alpha^2}\left(\frac{\cosh(\alpha x)}{\cosh\left(\frac{\alpha L}{2}\right)} - 1\right) \quad (2.46)$$

$$\delta_t(x) = u_s(x) - u_c(x) = \frac{F \times \sinh(\alpha x)}{\alpha E_S S_S \cosh\left(\frac{\alpha L}{2}\right)} \quad (2.47)$$

where,

$$\alpha = \sqrt{a} \quad (2.48), \qquad \beta = bEs \quad (2.49)$$

and

$$a = \pi d_s k_t \left(\frac{1}{E_s S_s} + \frac{1}{E_c S_c}\right) \quad (2.50), \qquad b = -\frac{\pi d_s k_t F}{E_s S_s E_c S_c} \quad (2.51)$$

F denotes the external force, L denotes the length of the steel bar, S_s denotes the cross-sectional area of the steel, E_c denotes Young modulus of concrete, E_S denotes Young modulus of steel, u_s is used for the steel displacement and u_c is used for the concrete displacement in the above given formulas.

Numerical Model

Concrete beam and steel bar are divided into 50 elements for the numerical analysis. Concrete is represented by 8 node cubic elements and steel is represented by 1D truss element in the numerical simulations. Total elasticity is assumed for both materials numerical analysis. Different tangential stiffness values (k_t) are tested. The stiffness values (k_t) are taken as 1.10^{11} Pa/m, 1.10^{12} Pa/m and 1.10^{14} Pa/m. Mesh geometry is represented as in Figure 2.23 and the simulation properties can be found in Table 2.9.

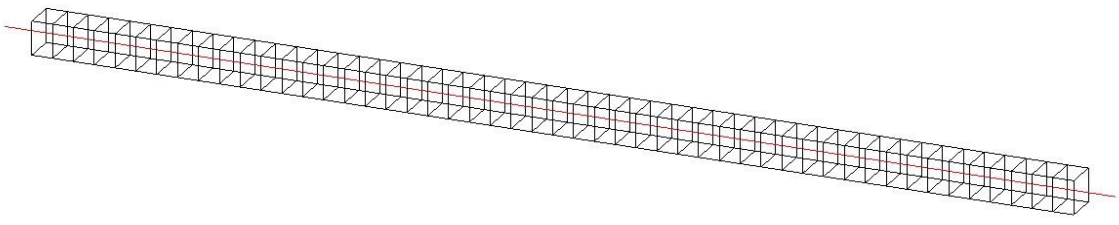

Figure 2.23 Concrete and steel mesh geometry of the tie rod.

Table 2.9 Simulation Properties.

	Mesh Geometry	Model Properties	Number of Elements
Concrete	3D Solid Elment	Elastic Behavior	50
Steel	1D Truss Element	Elastic Behavior	50
Interface	Joint Element (zero thickness)	Bond-slip Model 1) $k_t = 1.10^{11}$ Pa/m $k_{n1} = k_{n2} = 1.10^{15}$ Pa/m 2) $k_t = 1.10^{12}$ Pa/m $k_{n1} = k_{n2} = 1.10^{15}$ Pa/m 3) $k_t = 1.10^{11}$ Pa/m $k_{n1} = k_{n2} = 1.10^{15}$ Pa/m	50
Applied Load		**Time Steps**	
27.3kN		2	

The analytical and numerical solutions for stress along the steel rod and slip between the steel and concrete materials for different stiffness values are presented in Figures 2.24a and 2.24b respectively.

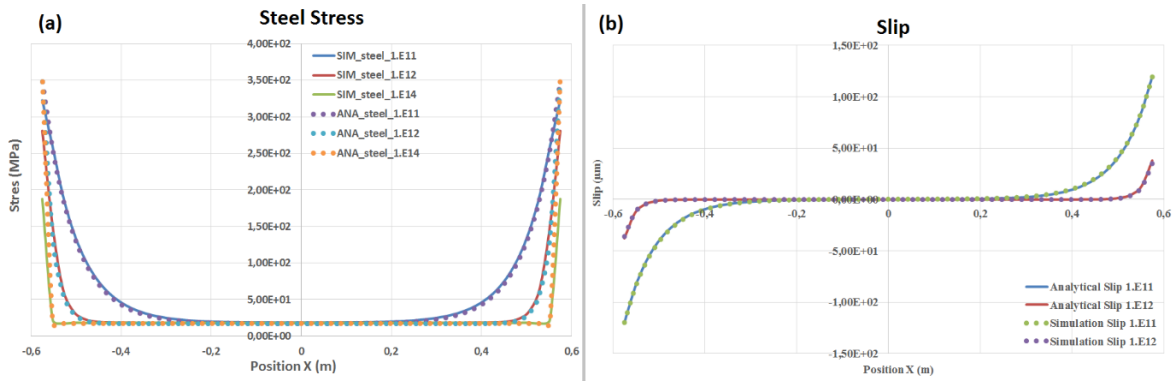

Figure 2.24 (a) Stress distribution along the steel bar, (b) Slip between the steel and concrete.

It can be clearly seen from Figures 2.24a and 2.24b that all the numerical results are identical as the analytical ones for different rigidity values (k_t). The stress on the steel bar is concentrated at the end-points in all the simulations as expected since the stress in the middle is transferred through the concrete cover. Thus, the maximum slip is observed at these end-points since the stress difference between steel and concrete is the highest at these points. These results confirm the validity of the new bond-slip model in the tangential direction.

Comparison between Bond-Slip Model and Perfect Bond Model on a Tie-Rod

It was expected that in the bond-slip model if the rigidity (k_t) in the tangential direction is taken high enough, the general behavior of the structure should be the same when the perfect bond

model is assumed between steel and concrete. In this part, 3 different rigidity values (k_t) are tested with bond-slip model to determine the proper tangential stiffness value (k_t) which provides the same results as the perfect bond model. The numerical analysis is performed on the same pull-out test geometry which was presented in Figure 2.22. Elastoplastic truss element is used for the steel rod representation and Mazars's damage model (Mazars 1986) is used for the concrete in order to be more realistic. Mazars concrete damage model is described below before representing the comparison of the two bond models. The details of simulation properties can be found in Table 2.8.

Mazars Damage Model

(Mazars 1986) has developed an isotropic damage model which takes only the positive principal strains into account to calculate the damage. This criterion is widely used for its simplicity and relative accuracy specially to represent failures of concrete structures under monotonic loading. In this model, the reduction in rigidity of the material under the effect of crack growth is calculated from a single scalar damage varying between 0 (no damage) and 1 (completely damaged structure). The stress in concrete is then governed by the law below:

$$\sigma = (1 - D)\, \Lambda : \varepsilon \qquad (2.52)$$

where σ is the stress tensor, ε is the strain tensor, D is the damage variable and Λ is the fourth order tensor of elasticity.

An equivalent strain ε_{eq} is defined from the positive principle strain tensors:

$$\varepsilon_{eq} = \sqrt{\sum_i (\langle \varepsilon_i \rangle)^2} \qquad (2.53)$$

with, ε_i the principal strain tensor. The damage threshold can be defined from:

$$f(D) = \varepsilon - K(D) = 0 \qquad (2.54)$$

with $K(D) = \varepsilon_{D0} =$ initial damage threshold.

Mazars model (Mazars 1986) makes it possible to describe the reduction of the stiffness of the material under the effect of micro-cracks in concrete. It depends on only one scalar local variable D that describes the isotropic damage and distinguishes the damage in tension or in

compression. The calculations of the damage variable and constraints are carried out from the strain tensor. The concrete damage is the combination of compression and tension which can be described in the formula below:

$$(\varepsilon) = \alpha_T(\varepsilon)D_T(\varepsilon) + \alpha_C(\varepsilon)D_C(\varepsilon) \qquad (2.55)$$

where D_T is damage in tension, D_C is damage in compression and ε is strain tensor.

Numerical Analysis

For the comparison of two models, 5 mm displacement is applied on the rod and the results are compared for different k_t values of the bond-slip model and also with the perfect bond hypothesis. All the other properties are taken the same as that was presented in Table 2.8. Three different rigidity values of $k_t = 1.10^{11}$ Pa/m, $k_t = 1.10^{12}$ Pa/m and $k_t = 1.10^{15}$ Pa/m are tested in the bond-slip model to affirm the same results as in the perfect bond relation. Stress slip curves of the pullout test with different tangential stiffness values are presented in Figure 2.25.

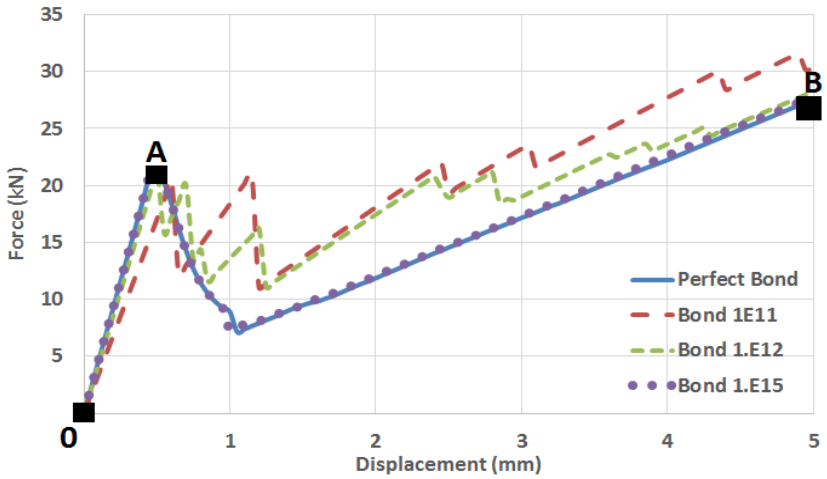

Figure 2.25 Force displacement curves of bond-slip model and perfect bond model.

It can be seen from Figure 2.25 that the general behavior of the bond-slip model with rigidity $k_t = 1.10^{15}$ Pa/m is the same as the perfect bond hypothesis. This means that if $k_t = 1.10^{15}$ Pa/m value is used in a bond-slip model, it behaves like the steel is perfectly bonded to the concrete cover and both materials have the same displacement when the load is applied to the structure. When the bond-slip model with the $k_t = 1.10^{12}$ Pa/m results are compared with the perfect bond model simulation results, it can be seen in Figure 2.25 that the bond model behaves almost the same as the perfect bond model in the elastic region (between the

points 0-A). Nevertheless, in $k_t = 1.10^{12}$ Pa/m simulation, the general behavior is quite different from the perfect bond results in the plastic region (A-B). This is also quite realistic since the steel and concrete has a different response in the plastic region at the first crack occurrence. It is also quite logical that the stress on the steel bar is quite higher in all the bond model simulations compared to the perfect bond results since stress transfer between the steel and concrete considered differently in the cracked locations through the interface. Results with the $k_t = 1.10^{11}$ Pa/m simulation is quite different from the perfect bond results both in elastic and plastic regions. This means that if the tangential stiffness (k_t) is taken high enough in the new model, the perfect bond solutions can be obtained.

Since it is expected to have a perfect behavior in the elastic region and different behavior in the plastic regions, it seems plausible to use $k_t = 1.10^{12}$ Pa/m rigidity value in the bond-slip simulations. However, for some applications, a higher rigidity might be necessary to obtain the perfect behavior in the plastic region. It is essential to explore the rigidity values (k_t) for different configurations and with different applications in order to make a proper calibration on the bond model.

5. Conclusion

The developments in the bond-slip model is presented in this Chapter. Antecedently, the transversal behavior of the bond-slip model is analyzed. The results have revealed that the forces on the interface element nodes are not accurately calculated. Subsequently the source codes are reviewed to detect this anomaly. It has been discovered that there is a drawback related with the integration of the forces between the local and global coordinate systems. The normal directional forces on the interface element nodes were assumed to be equal to each other in the initial bond-slip model. This assumption does not correspond to the reality and provokes incorrect results in the numerical applications. The appropriate formulations for the numerical integration are implemented inside the source codes right after the detection of this deficiency. The same simulations are performed once more on the interface element and a concrete box with reinforcement to see the improvements in the modified model. The results with the modified bond-slip model have shown that the forces on the interface element nodes are calculated correctly. The accuracy of force values at the end of the numerical calculations are checked with a very simple analytical solution.

Subsequently, the irreversible behavior of the bond-slip model is analyzed. Several numerical tests are performed on the single interface element under cyclic loading. Different adhesion laws and different alternative loadings are examined within these simulations. The cyclic adhesion law proposed by (Mang 2016) is found to be suitable for the adhesion law for the steel-concrete bond that is proposed by (Torre-Casanova 2013) and it is not applicable to another adhesion law which may be defined by the user. A completely new methodology is defined in order to represent the irreversibility of the interface which does not include the headachy of the previous model. This new methodology is implemented successfully in the (Cast3M 2017) finite element code. The new irreversible model is a general approach which is capable of adopting the user defined adhesion law applications. The friction forces of the bond can also be exclusively defined by the user and will be taken into account during the whole numerical process. The irreversible behavior of the interface is defined accurately in the new model and validated by various tests on the interface element. Since the new model checks and eliminates the inappropriate alternatives in order to find the authentic irreversible behavior; in comparison to the previous model that checks all the probabilities one by one, the calculation time of the new model is reduced by around 16% with respect to the initial version for the interface element trials.

Finally, the tangential behavior of the new bond-slip model is tested on a Tie-rod by comparing with analytical results. Three different stiffness (k_t) values are used for this test. The numerical and analytical results are found to be identical. Through all these numerical tests presented in this Chapter, tangential, transversal and irreversible behavior of the new bond-slip model is validated.

Chapter-3:
Implementation of the Confinement Effect on the Bond Behavior

1. Introduction

As mentioned earlier, active confinement has an influence on the steel-concrete bond behavior ((Eligehausen, Popov and Bertero 1983), (Malvar 1991) etc.). In this section, the implementation and validation of the active confinement effect on the bond-slip model are explained in detail. Moreover, the effect of active confinement on the structural behavior is investigated on a tie-rod by using the new bond-slip model.

2. Implementation of the Confinement Effect to the Bond-Slip Model

By means of active confinement, external pressure on the reinforced structure is affecting the adhesion properties of the bond. In order to represent this kind of behavior numerically, an empirical formulation is suggested to modify the adhesion law which is an input parameter of the bond-slip model, according to the external stress values. In literature, several authors like (Robins and Standish 1982), (Lowes, Moehle and Govindjee 2004), (Zhang, Wu, et al. 2016) etc. has mentioned that the active confinement effect on the slip properties is negligible while it significantly affects the ultimate bond strength (τ_u). Only the confinement effect on the bond stress is thus taken into account while the effect of lateral pressure on the slip is neglected. External tension and compression have different effects on the bond behavior. It has been mentioned earlier that bond strength increases with increasing lateral compression ((Robins and Standish 1982), (Xu, Wu, et al. 2014)), on contrary it decreases with increasing lateral tension ((Wu, et al. 2014)). After a detailed literature research, it has been found that the bond

stress (τ) is directly related with the lateral pressure (P_{lat}) and compressive strength of the concrete (f_c). Several experimental campaigns like (Orangun, Jirsa and Breen 1977), (Eligehausen, Popov and Bertero 1983), (Zhang, Dong, et al. 2014), etc., tend to show that the bond properties increase with the ratio of lateral pressure over the compressive strength (Eq. 3.1):

$$\tau \propto \sqrt{\frac{P_{lat}}{f_c}} \tag{3.1}$$

As mentioned in Chapter 1, several authors propose relations based on (Eq.3.1) to model the confinement effect on the steel-concrete bond ((Xu, Wu, et al. 2014), (Wu, et al. 2014) (Zhang, Wu, et al. 2016) etc.). When the lateral pressure is tension, some authors propose a reduction of the bond properties related to the tensile strength of the concrete ((Zhang, Dong, et al. 2014), (Wu, et al. 2014)).

Moreover, an effect of the concrete cover and the steel diameter on the active confinement is observed in different experimental tests according to the literature ((Shang, et al. 2017), (Xu, Wu, et al. 2014) etc.). The lower the concrete cover to steel diameter ratio (c/d_s), the greater the effect of lateral pressure. This ratio has already an influence when there is no active confinement. Indeed, for small (c/d_s) ratios, the passive confinement induced by the ribs of the reinforcement when the steel slips in the concrete can lead to a splitting failure of the cover concrete. (Torre-Casanova, Jason, et al. 2013) suggested a formulation in order to determine the splitting or the pull-out failures in reinforced concrete structures. This is detailed in Chapter 1, section 4.3.2.

Based on the consideration above, we propose a modeling of the influence of the lateral pressure around the steel through the relations given in Eq. 3.2 and Eq. 3.3:

For lateral compression (where $P_{lat} < 0$):

$$\tau^* = \tau\left(1 + \alpha\sqrt{\left|\frac{P_{lat}}{f_c}\right|}\right) \tag{3.2}$$

For lateral tension (where $P_{lat} > 0$):

$$\tau^* = \tau\left(1 - \alpha\sqrt{\left|\frac{P_{lat}}{f_t}\right|}\right) \tag{3.3}$$

where τ is the bond stress without confinement, τ^* is the modified bond stress under lateral pressure, P_{lat} is the applied lateral pressure on the interface, f_c and f_t are the concrete compressive and tensile strengths. α depends on the concrete cover to steel bar diameter ratio (c/d_s).

After the analysis of experimental results on several test campaign of the literature, our definition of the parameter α is based on the following considerations:

- There is a transition value for the ratio c/d_s below which the influence of lateral pressure is quite strong and above which the influence is weak. We proposed to use the same value as (Torre-Casanova, Jason, et al. 2013) for the transition value: $(c/d_s)_t = 4.5$
- α is near 1 for very small c/d_s ratios and tends toward 0 for large values of c/d_s, with a quite strong drop around the transition value

A continuous expression is chosen based on exponentials (Fig 3.1):

$$\alpha = 1 - e^{\beta\left[\frac{c}{d_s} - a\right]} \quad \text{if } \frac{c}{d_s} \leq 4.5 \tag{3.4}$$

$$\alpha = e^{-\gamma\left[\frac{c}{d_s} - b\right]} \quad \text{if } \frac{c}{d_s} > 4.5 \tag{3.5}$$

β and γ are parameters to control the shape of the exponentials, while a and b are adjusted to assure the continuity of α and its derivative at the transition point $(c/d_s)_t = 4.5$.

For the following we choose the shapes $\beta = 1$ and $\gamma = 0.8$, this led to $a = 5.31$ and $b = 3.77$.

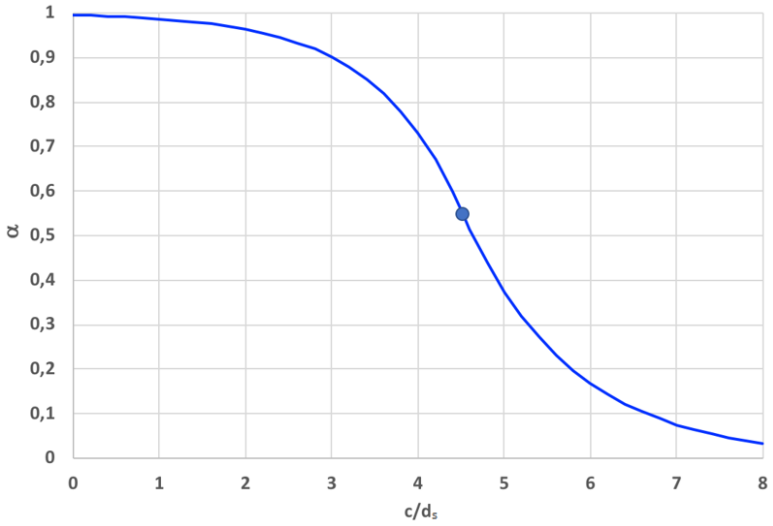

Figure 3.1 Evolution of α as a function of c/d_s.

The bond stress (τ) of the input adhesion law is modified according to applied lateral pressure on the interface while the slip (s) keeps constant with the given equations above. An example of initial (defined by user) and modified (under 10MPa external compression) bond stress-slip laws within the new bond-slip model can be found in Figure 3.2 where τ_u^* is the modified ultimate bond stress and τ_u is the initial ultimate bond stress, τ_f^* is the modified frictional bond stress and τ_f is the initial frictional bond stress.

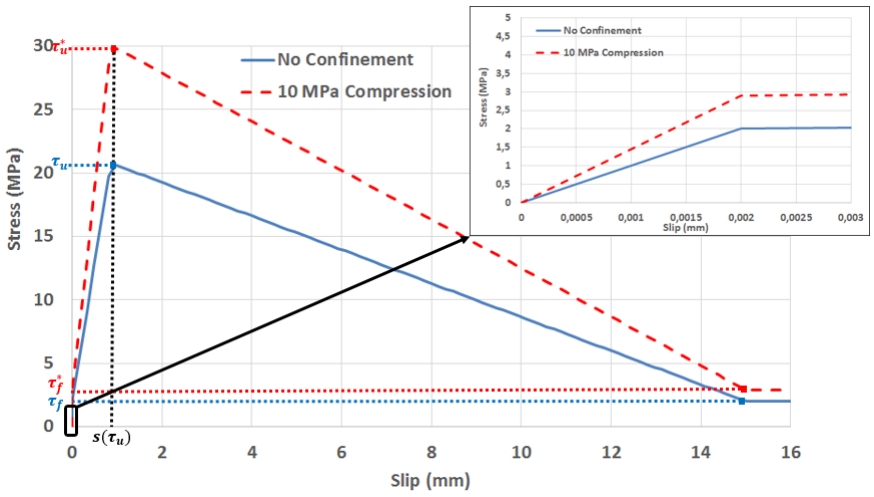

Figure 3.2 Modification of adhesion law in new bond-slip model by considering applied external pressure (active confinement).

According to new bond-slip model, the concrete properties (f_c and f_t), adhesion law (τ(s)) and concrete to steel ratio (c/d_s) are defined as the input parameters. The external pressure applied to the interface (P_{lat}) is calculated for each interface element and for each calculation step. After obtaining the lateral stresses (P_{lat}) on the steel-concrete interface, the stress-slip relation (adhesion law) is modified by the proposed formulas (Eq. 3.2 and 3.3). Then the bond stress

and slip are calculated according to this modified adhesion law. The calculation of lateral pressure (P_{lat}) within the new bond-slip model can be explained with Figure 3.3.

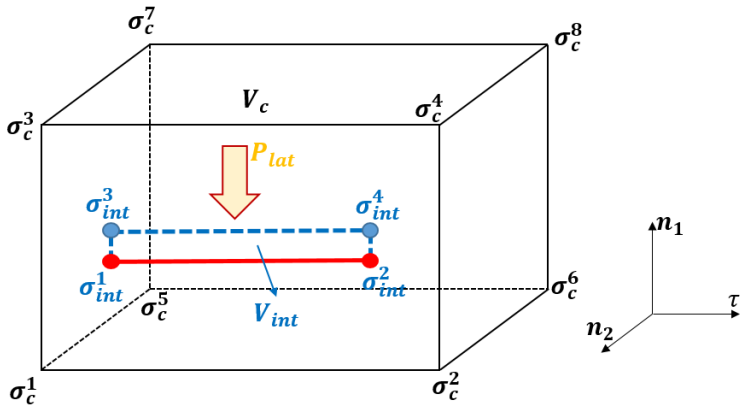

Figure 3.3 Stresses on the concrete and the interface element nodes.

The lateral pressure (P_{lat}) per interface element is calculated with the following order:

1. Detection of the concrete element nodes around each interface element (V_c).
2. Projection of the stress values for each concrete element (σ_c) on the corresponding interface element (σ_{int}).
3. For each Gauss point of the interface element, compute the stress matrix in the local coordinate system (t, n_1, n_2)
4. Calculation of stress values in the normal directions of the reinforcing bar (n_1 and n_2) with the given formula:

$$P_{lat} = \frac{\sigma_{int}^{n_1 n_1} + \sigma_{int}^{n_2 n_2}}{2} \qquad (3.6)$$

Since P_{lat} is calculated for each interface element, the lateral pressure applied to the interface is not uniform along the steel bar. This means the effect of confinement on the bond properties may vary along the steel length.

The algorithm above is implemented with the "PROCEDURE_PERSO1" of (Cast3M 2017), which has to be written in GIBIANE language (data high-level language of Cast3M). This user procedure is called after each time step, and it has access to all the precedent time steps results. The computed lateral pressure is stored in the "internal variables" field, in such a way that it will be accessible, in the next time step, at the Gauss point level of the interface elements, when the behavior law is called. This first implementation is valid in our examples where the steel

elements are along the global x-axis. In this case, the third step of the algorithm (coordinate system changing) is not needed since:

$$\sigma_{int}^{n_1 n_1} = \sigma_{int}^{yy} \quad (3.7), \qquad \sigma_{int}^{n_2 n_2} = \sigma_{int}^{zz} \quad (3.8)$$

In this logic, the concrete stresses which are considered in the new bond-slip model are taken from the previous calculation step. This means that calculated lateral pressure on the interface (P_{lat}) will be used in the next calculation step to modify the adhesion law. The consideration of P_{lat} values per calculation step can be easily seen in Figure 3.4. This kind of consideration may delay the response of the active confinement on the bond but can be easily compensated by using sufficiently small calculation steps.

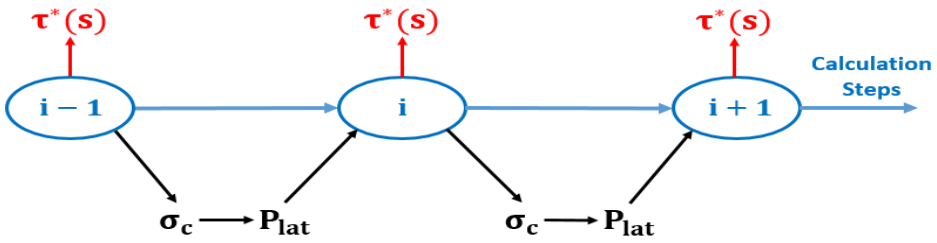

Figure 3.4 Consideration of the confinement effect with the new bond-slip model.

3. Validation of the new model

After implementing the effect of confinement on the bond-slip model, it was validated with several test geometries. In this section, the validation tests and their results are presented.

3.1. Interface Element Test

The first series of simulations are performed on a single interface element to be focused only on the bond behavior under various lateral pressures. In order to test only the implementation accuracy, a very simple geometry is chosen. Figure 3.5 represents a 2 cm length single interface element with zero thickness. The bottom nodes are blocked against displacement and the loading is applied to both of the top nodes as an imposed displacement along the x-direction (u_x). Different lateral compression and tension are applied on the top of the interface element to test the confinement effect.

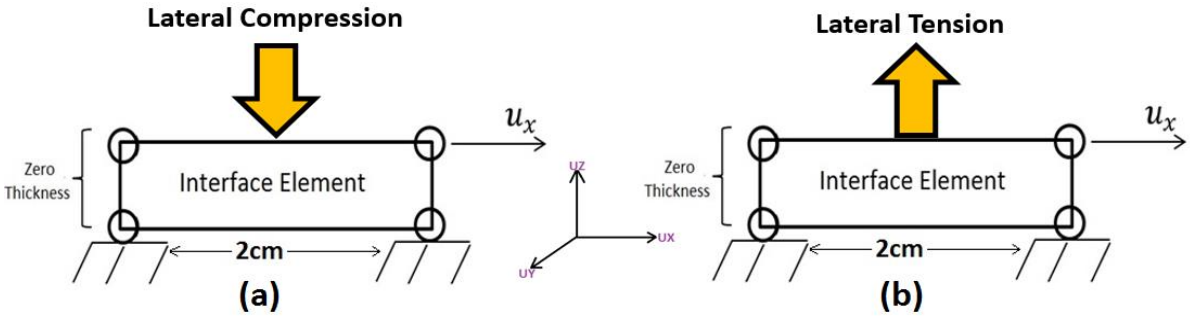

Figure 3.5 Representation of the interface element geometry: (a) under lateral compression, (b) under lateral tension.

Monotonic Loading

The first test series are performed on the single interface element for monotonic loading case. Figure 3.6a shows stress-slip relation as an input parameter for this test which is proposed by (Torre-Casanova 2013) and Figure 3.6b defines the imposed displacement in the x-direction. Three different constant lateral pressure values (both tension and compression) are also applied from the beginning of the computation until the end. The applied lateral compression and tension values are presented in Table 3.1.

Table 3.1 Applied Lateral pressure values.

Lateral Compression	Lateral Tension
No confinement (0 MPa)	No confinement (0 MPa)
5 MPa	1 MPa
10 MPa	2 MPa

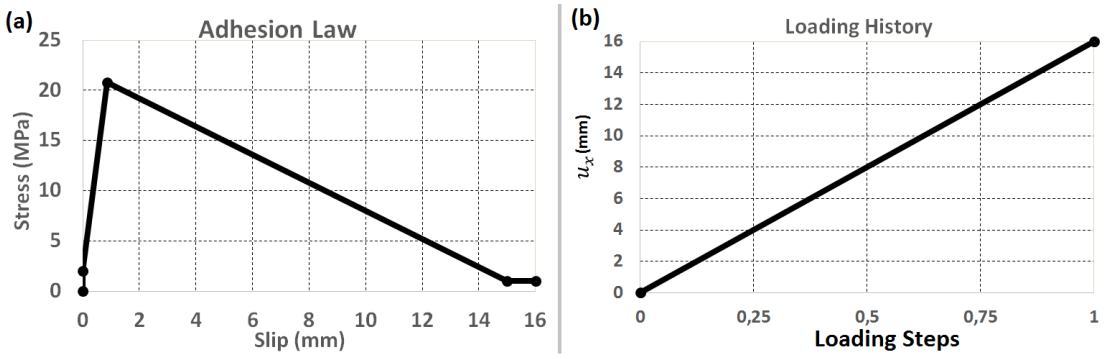

Figure 3.6 (a) Adhesion law, (b) Loading history for the monotonic interface element test.

Figure 3.7 represents the bond stress-slip relation of the interface element under various lateral tension and compression. It can be seen that the bond strength is increased under increasing lateral compression (Figure 3.7a). On contrary, bond strength is decreased under increasing lateral tension (Figure 3.7b).

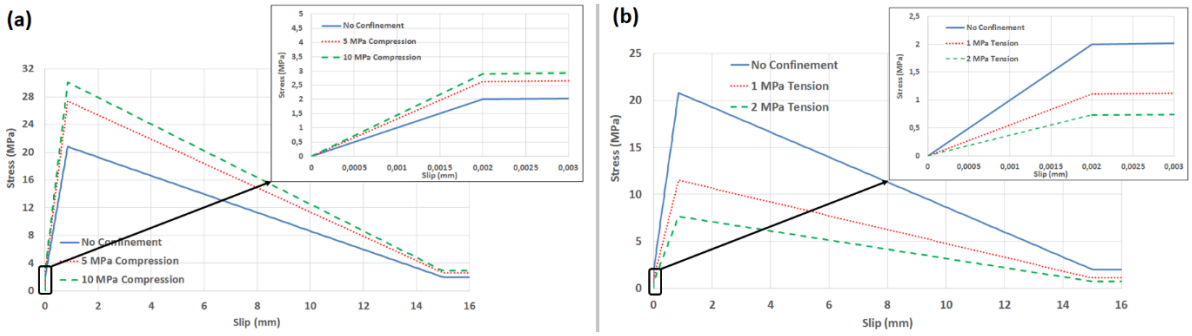

Figure 3.7 Bond stress-slip relation under (a) lateral compression, (b) lateral tension.

In order to validate the implementation, the ultimate bond stress (τ_u) is analytically calculated for different lateral pressures by using Eq. 3.2 and Eq. 3.3. The analytical results are compared with the numerical ones in Table 3.2. Coherent τ_u values are obtained between numerical and analytical solutions.

Table 3.2 Comparison of analytical and numerical ultimate bond stress values for interface element test.

	Ultimate Bond Stress: τ_u (MPa)	
Lateral Compression	**Analytical**	**Numerical**
No confinement	20.80	20.80
5 MPa	27.38	27.38
10 MPa	30.10	30.10
Lateral Tension	**Analytical**	**Numerical**
No confinement	20.80	20.80
1 MPa	11.49	11.49
2 MPa	7.64	7.64

Cyclic Loading

For the second series of simulation, the confinement effect on the irreversible bond behavior is tested. In order to do so, an alternative loading is applied on the single interface element as presented in Figure 3.8a. Moreover, an increasing lateral pressure is applied to the element to observe the effect of confinement throughout the calculation procedure. Applied lateral pressure is presented in Figure 3.8b. Identical initial conditions and bond properties (adhesion law) are defined for the interface as in the monotonic case.

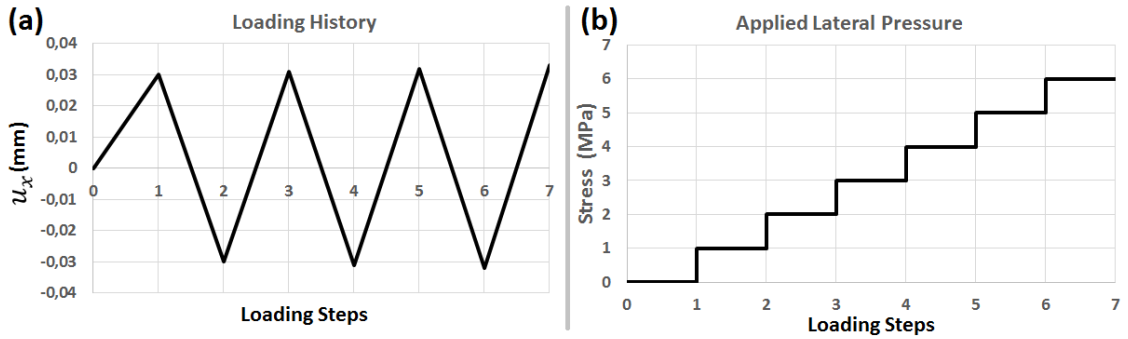

Figure 3.8 (a) Loading history, (b) applied lateral pressure for the cyclic interface element test.

Figure 3.9 represents the irreversible stress-slip relation of the interface element under increasing lateral pressure. It can be seen that the bond strength is increased by increasing lateral pressure as expected. The remaining friction stress in the irreversible behavior (unloading and reverse reloading) is also increased. The connections of the different parts of the response are correct, even in case of variation of lateral pressure during the loading. The implementation methodology is validated for monotonic and cyclic cases for constant and variable applied lateral pressures.

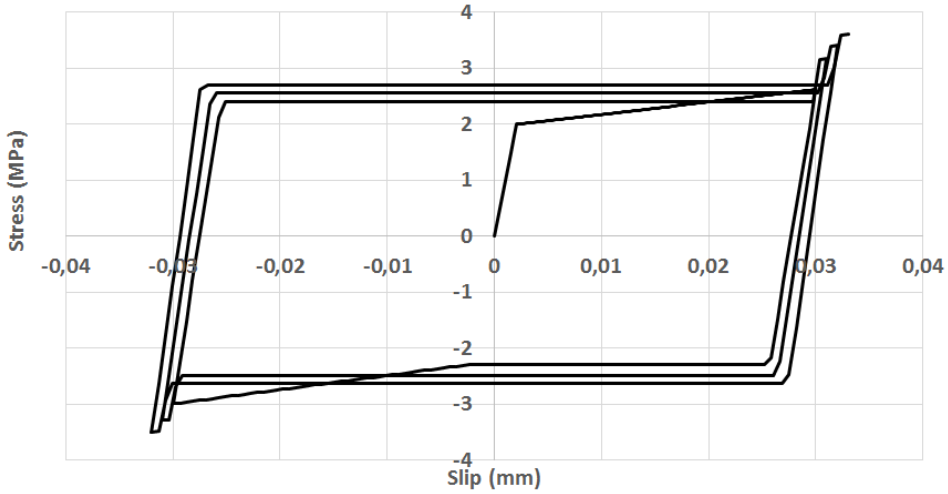

Figure 3.9 Irreversible bond stress-slip relation under increasing lateral pressure.

3.2. Pull-out Tests

After validating the implementation methodology with interface element tests, several experimental campaigns are reproduced by new bond-slip to validate the proposed formulas for the active confinement effect. As mentioned earlier, the pull-out tests are commonly performed to analyze the bond behavior of reinforced concrete structures ((Abrams 1913), (Eligehausen, Popov and Bertero 1983), (Malvar 1991) etc.). After a detailed literature research, three different experimental pull-out campaigns by (Torre-Casanova, Jason, et al.

2013), by (Shang, et al. 2017) and by (Xu, Zhimin, et al. 2012) are chosen for the model validation. In all the experimental tests, the embedment lengths (l_e) are taken equal to the five times of the steel bar diameter (d_s). Various concrete to steel ratios (c/d_s), applied lateral pressures (P_{lat}) and bond properties (strong and weak) are tested. New bond-slip model is used for all the simulations and the numerical results are compared with the experimental ones. The performed pull-out tests and their results are explained one by one in the following sections.

3.2.1. Pull-Out Test-1: (Torre-Casanova, Jason, et al. 2013)

For the first pull-out test, the confinement effect on rather strong bond properties ($\tau_u \cong 22.5$ MPa) is analyzed. The pull-out experimental campaign by (Torre-Casanova, Jason, et al. 2013) is simulated numerically by using new the bond-slip model under three different lateral compression (No confinement, 5 MPa and 10 MPa). A steel bar with a 12 mm diameter (d_s) is embedded inside a cubic concrete (V_c) with a length of 180 mm in each dimension. The embedment length (l_e) of the steel bar is 60 mm ($5 \times d_s$) and cover to diameter ratio (c/d_s) is equal to 7. Schematic of the experimental testing system and pull-out specimens are shown in Figure 3.10. The geometric properties of the specimen are presented in Table 3.3 Properties of steel and concrete are given in Table 3.4 and Table 3.5 respectively.

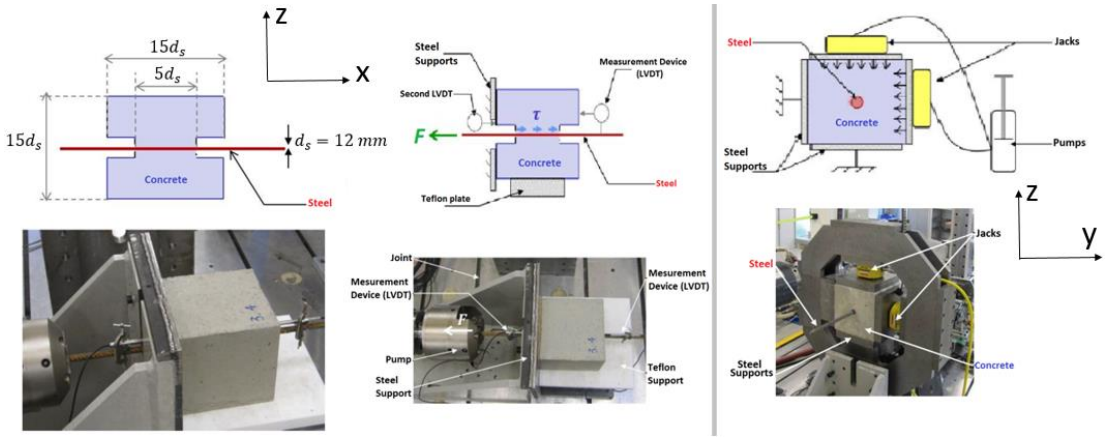

Figure 3.10 Pull-out test setup and specimen geometry (Torre-Casanova, Jason, et al. 2013).

Table 3.3 Geometric properties of (Torre-Casanova, Jason, et al. 2013)'s pull-out specimen.

Steel Bar Diameter d_s (mm)	Dimension of the Specimen V_c (mm^3)	Embedment Length l_e (mm)	Concrete to Steel Ratio c/d_s
12	$180 \times 180 \times 180$	$5 \times d_s$	7

Table 3.4 Concrete properties of (Torre-Casanova, Jason, et al. 2013)'s pull-out tests.

Young Modulus E_c (GPa)	Poisson Ratio ν_c	Compressive Strength f_c (MPa)	Tensile Strength f_t (MPa)
28	0.2	36.6	3.12

Table 3.5 Steel properties of (Torre-Casanova, Jason, et al. 2013)'s pull-out tests.

Young Modulus E_s (GPa)	Poisson Ratio ν_s	Yielding Strength f_y (MPa)	Diameter d_s (mm)
200	0.3	560	12

For the numerical analysis of the pull-out specimen, the steel is represented by truss elements and the concrete is represented by 3D solid elements. The behavior of the concrete is modeled by damage tension-compression (Damage TC) model implemented in Cast3M (Costa, et al. 2004). This is a coupled damage plasticity model, with two damage variables, one in tension and one in compression. This model is regularized in energy in tension with a Hillerborg implementation (Hillerborg 1983).

The mesh of the simulation is arranged to have 5 concrete elements and 10 steel elements along the embedment length (l_e). The mesh geometry of the pull-out specimen and the assumed aleatory tensile concrete strength distribution are presented in Figure 3.11a and 3.11b.

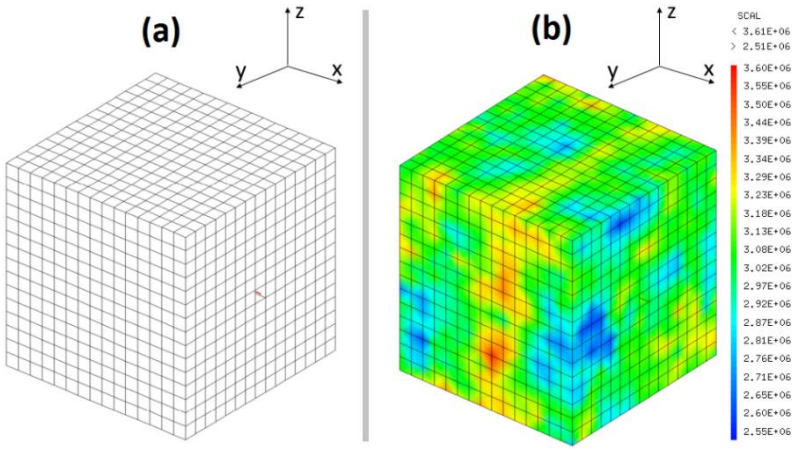

Figure 3.11 (a) Mesh geometry and (b) aleatory strength distribution in the pull-out specimen.

The bottom and left side surfaces are blocked in z and y directions respectively, the front face is blocked in the x-direction (U_x^c) against displacement and lateral pressure is applied on the top and right side surfaces (P_z and P_y) (Figure 3.12a). A displacement (U_x^s) is imposed on one end of the steel bar along x-direction while the other end of the steel bar remains free. The input adhesion law is fitted by inverse analysis to obtain the experimental unconfined response of the pull-out test. It is shown in Figure 3.12b.

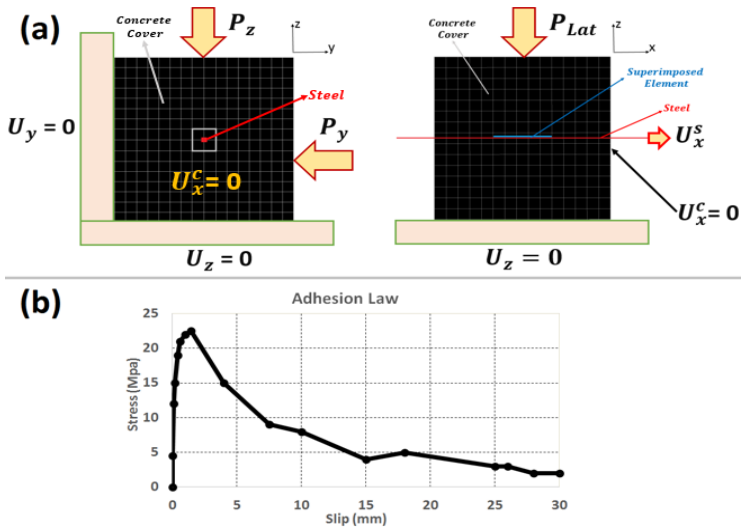

Figure 3.12 (a) Boundary conditions of the simulation, (b) adhesion law of the pull-out specimen.

Numerical Results

The bond stress-slip curves of the pull-out simulations under the three different confining compressions are presented in Figure 3.13. Moreover, the computed distribution of lateral pressure in the interface elements along the embedded steel bar, at the time of the peak on the bond stress-slip curves, is presented in Figure 3.14. One can see that even for the unconfined

case, there is a high lateral pressure (around 7.6 MPa in average), which explains why for the unconfined test, the pull-out response ($\tau_u = 26.6$ MPa in Figure 3.13) is higher than the input model ($\tau_u = 22.5$ MPa in Figure 3.11b). Furthermore, the effect of external confinement (5 or 10 MPa) on the pull-out response is almost null (in experiments and in simulations). Indeed, for this specimen with a high concrete cover to steel diameter ratio ($\frac{c}{d_s} = 7$), even if the lateral pressure increases in the interface elements, in average from 7.6 MPa (unconfined) to 10.6 MPa (5 MPa confining pressure) or to 14.3 MPa (10 MPa confining pressure), the α parameter in Equation (3.2) is small, thus the influence of P_{lat} is small.

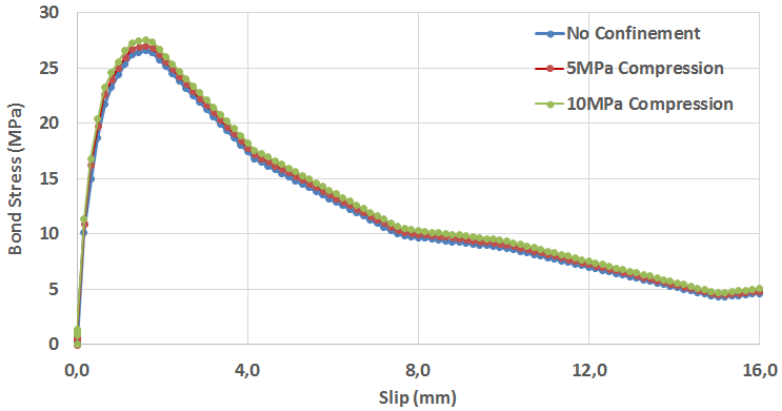

Figure 3.13 Bond stress vs. slip curves of pull-out specimens under lateral compressive stress.

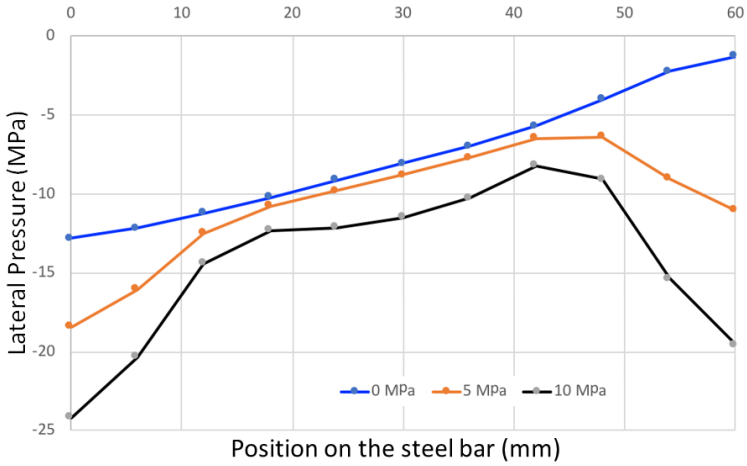

Figure 3.14 Distribution of lateral pressure along the steel bar, at the peak values of the bond stress-slip curves.

The comparison of bond strengths (τ_u) between experimental and numerical results for different lateral pressures (P_{lat}) are given in Table 3.6.

Table 3.6 Influence of the lateral compression on the bond stress.

	Bond Strength τ_u (MPa)	
Lateral Pressure P_{lat} (MPa)	**Experimental**	**Numerical**
0	24.28 ± 2.70	26.60
5	25.50 ± 1.42	27.04
10	28.50 ± 0.18	27.55

The final damage patterns (in the middle cross-section in the z-direction) are presented in Figure 3.15. It can be seen that the damage is localized around the steel, this is typical of a pull-out failure which occurs in case of high c/d_s ratios. Due to the relatively high lateral pressure, the bond strength is also high and the behavior of the interface tends toward a perfect bond.

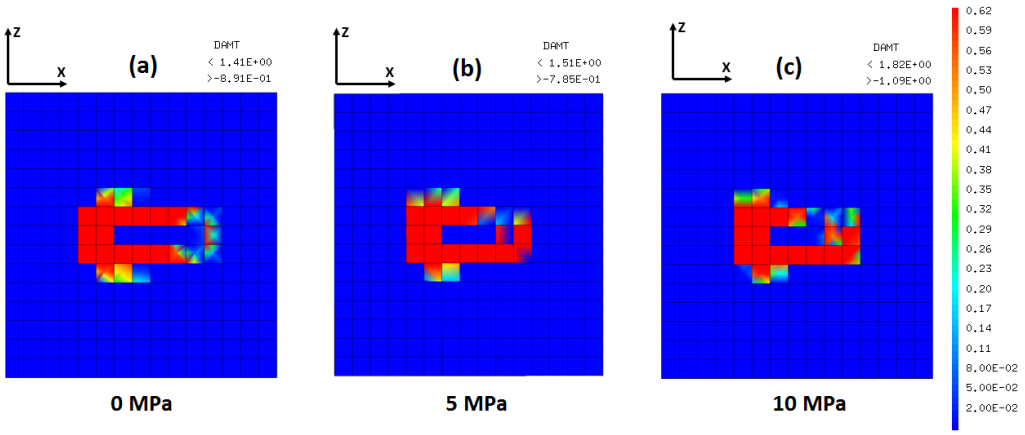

Figure 3.15 Cross-sections of final damage patterns under: (a) 0 MPa (no active confinement), (b) 5 MPa and (c) 10 MPa compression.

Numerical results are close to the experimental ones (Table 3.6). Even though the obtained numerical bond strength values (τ_u) are slightly different than the experimental ones, the general trend of the increase rate over lateral pressure (P_{lat}) is in accordance with the experimental results. It should be considered that there is a huge variance in the experimental results (Torre-Casanova, Jason, et al. 2013).

3.2.2. Pull-Out Test-2: (Shang, et al. 2017)

For the second pull-out test, the experimental campaign of (Shang, et al. 2017) is simulated under four different lateral compressions (No confinement, 8.99 MPa, 14.22 MPa and 20 MPa). Two steel bars diameters (14 mm and 22mm) are considered. They are embedded inside a cubic concrete (V_c) with a length of 150 mm in each dimension. This way, two different cover

concrete to steel ratio (c/d_s) are tested with the new bond-slip model. The schematic of the experimental testing system and pull-out specimens are shown in Figure 3.16a and 3.16b. The geometric properties of the specimen are presented in Table 3.7. Properties of steel and concrete are given in Table 3.8 and Table 3.9 respectively.

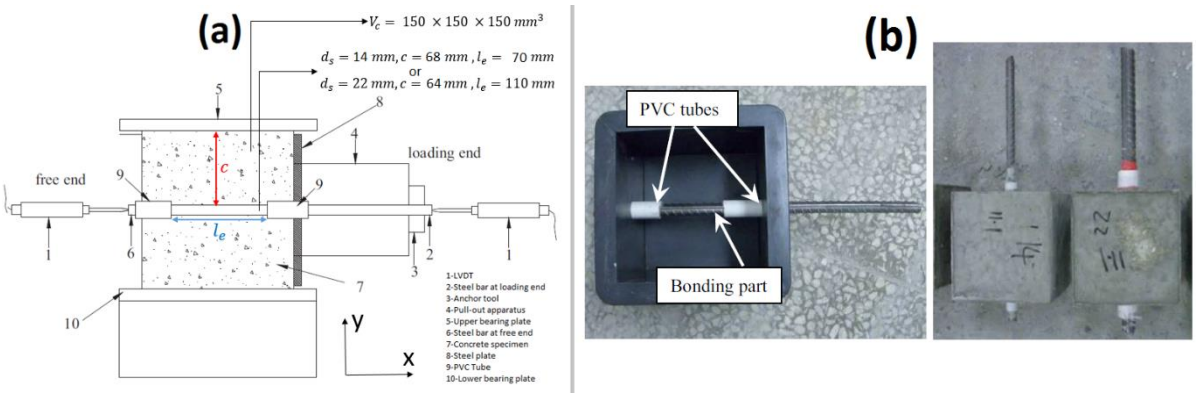

Figure 3.16 (a) Schematic of testing system for pull-out specimen under lateral compressive load. (b) Photo of pull-out specimens (Shang, et al. 2017).

Table 3.7 Geometric properties of (Shang, et al. 2017)'s pull-out specimen.

Steel Bar Diameter d_s (mm)	Dimension of the Specimen V_c (mm^3)	Embedment Length l_e (mm)	Concrete to Steel Ratio c/d_s
14	$150 \times 150 \times 150$	$5 \times d_s$	4.86
22	$150 \times 150 \times 150$	$5 \times d_s$	2.91

Table 3.8 Concrete properties of (Shang, et al. 2017)'s pull-out tests.

Young Modulus E_c (GPa)	Poisson Ratio ν_c	Compressive Strength f_c (MPa)	Tensile Strength f_t (MPa)
27.6	0.2	42.5	3.4

Table 3.9 Steel properties of (Shang, et al. 2017)'s pull-out tests.

Diameter d_s (mm)	Young Modulus E_s (GPa)	Poisson Ratio ν_s	Yielding Strength f_y (MPa)
14	200	0.3	400
22	200	0.3	400

For the numerical analyses of the pull-out specimen, the steel is represented by 1D truss elements and the concrete is represented by 3D solid elements with Damage TC model. In order to obtain the same number of steel (10) and concrete (5) elements along the embedment length (l_e), different mesh densities are used for the different steel bar diameters. The mesh

geometries and the assumed aleatory tensile concrete strength distributions are presented in Figure 3.17a and 3.17b.

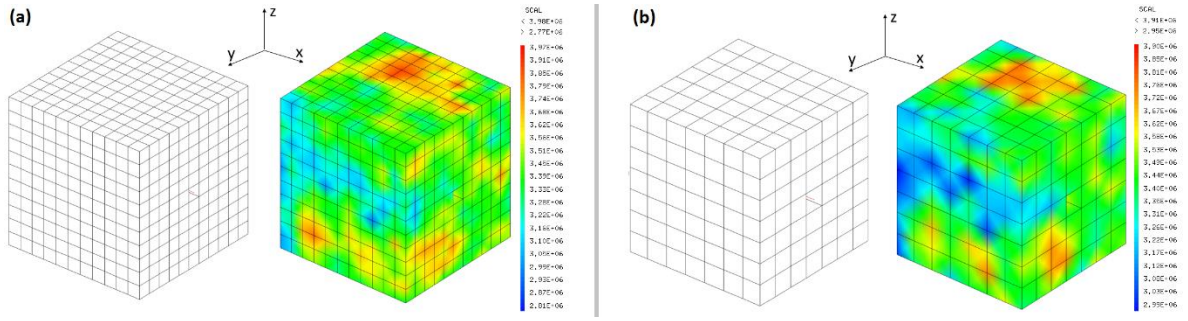

Figure 3.17 Mesh geometry and aleatory strength distribution of the pull-out specimens for: (a) $d_s = 14$ mm and (b) $d_s = 22$ mm.

The bottom face is blocked in the z-direction (U_z), the front face is blocked in the x-direction (U_x^c) against displacement and the lateral pressure is applied only on the top surface (P_{lat}) of the pull-out specimen (Figure 3.18a). A displacement (U_x^s) is imposed on one end of the steel bar along the x-direction while the other end of the steel bar remains free. Figure 3.18b shows the input adhesion laws which are fitted on the experimental results of (Shang, et al. 2017) for the unconfined cases.

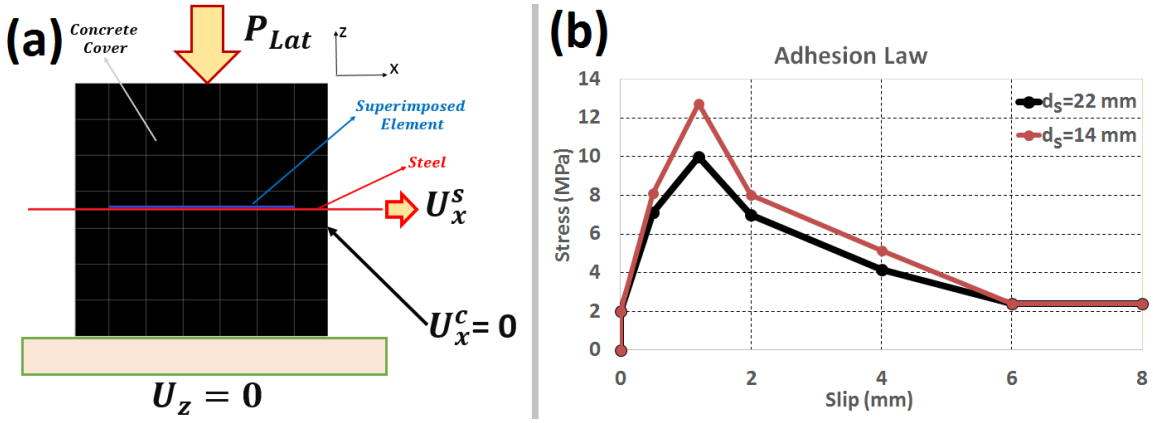

Figure 3.18 (a) Boundary conditions and (b) adhesion laws of the pull-out specimen.

Numerical Results

The bond stress-slip response curves are presented in Figures 3.19 for the four different confining compressions. The comparison of ultimate bond strengths (τ_u) between experimental and numerical results are given in Table 3.10. The computed lateral pressures along the steel at the time of the peak bond stress are presented on Figure 3.20a and 3.20b.

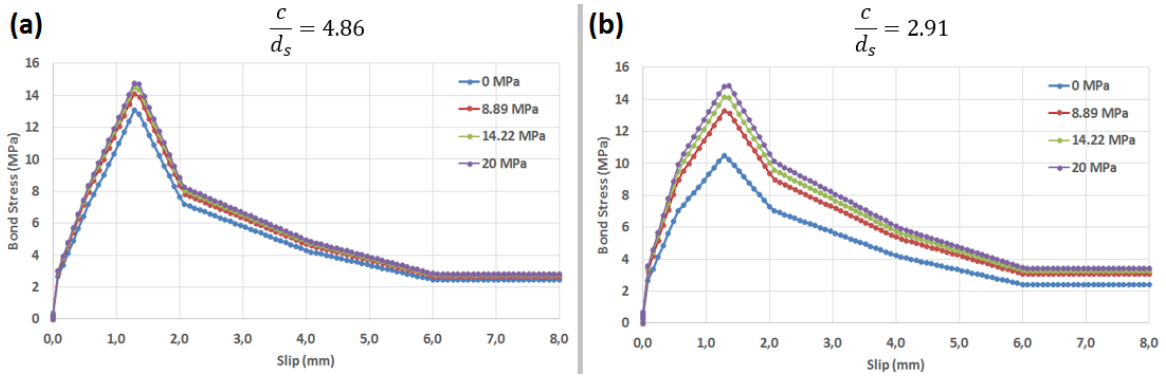

Figure 3.19 Bond stress vs. slip curves of pull-out specimens under lateral compressive stress for (a)$\frac{c}{d_s} = 4.86$ and (b) $\frac{c}{d_s} = 2.91$.

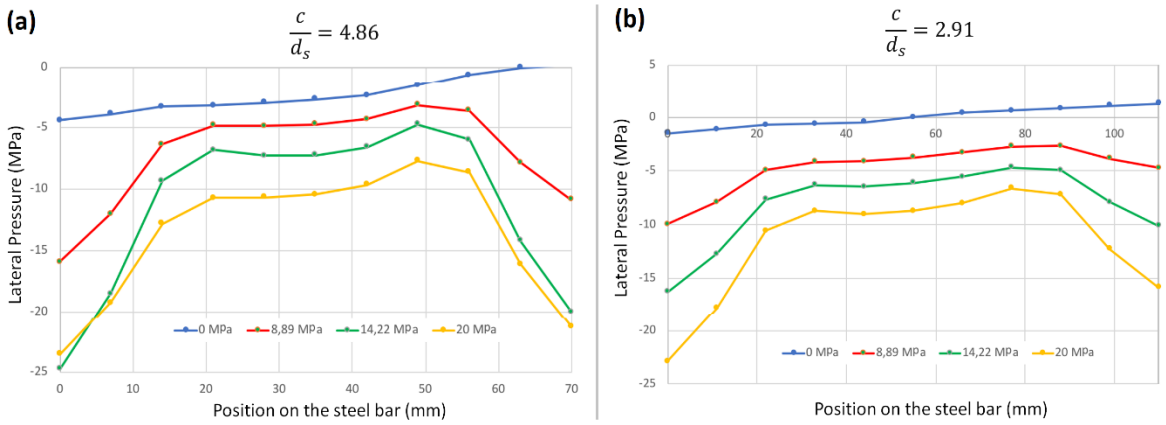

Figure 3.20 Distributions of lateral pressure along the embedded steel at the peak bond stress (a)$\frac{c}{d_s} = 4.86$ and (b) $\frac{c}{d_s} = 2.91$.

For the steel diameter of 22 mm, the concrete cover to steel diameter ratio is small $\frac{c}{d_s} = 2.91$. Since the lateral pressure in the unconfined case is null (Figure 3.20b), the response of the pull-out simulation gives the same bond strength than the input model ($\tau_u = 10$ MPa). When a confining pressure is applied, it influences a lot the lateral pressure computed in the interface elements along the steel, which is in average almost half of the confining pressure (4.8 MPa, 8 MPa and 11.6 MPa for confining pressures of 8.89 MPa, 14.22 MPa and 22 MPa respectively). Combined to a high value for α (near 1) in case of small c/d_s ratio (Figure 3.1), the pull-out response is highly influenced by lateral confinement. This is in accordance with the experimental results (Table 3.10).

For the steel diameter of 14 mm, the c/d_s ratio (4.86) is intermediate between the (Torre-Casanova, Jason, et al. 2013) case one ($\frac{c}{d_s} = 7$) and the 22 mm (Shang, et al. 2017) case one ($\frac{c}{d_s} = 2.91$). Here the lateral pressure in the unconfined case is equal to 2.3 MPa in average (Figure 3.20a), and the pullout simulation gives a value of τ_u equal to 13 MPa, in accordance

with the experimental value. Due to a lower value of the α coefficient, the influence of confinement is lower than in the 22 mm steel diameter case.

Table 3.10 Influence of the lateral compression on the bond stress.

		Bond Strength τ_u(MPa)	
Lateral Pressure P_{lat} (MPa)	**Steel Bar Diameter D_s (mm)**	**Experimental**	**Numerical**
0	14	13.32	13.12
	22	10	10.43
8.89	14	13.53	14.12
	22	13.81	13.34
14.22	14	14.51	14.49
	22	14.21	14.20
20	14	14.40	14.72
	22	14.83	14.85

The final damage patterns in the middle cross-section in the z-direction are presented in Figure 3.21.

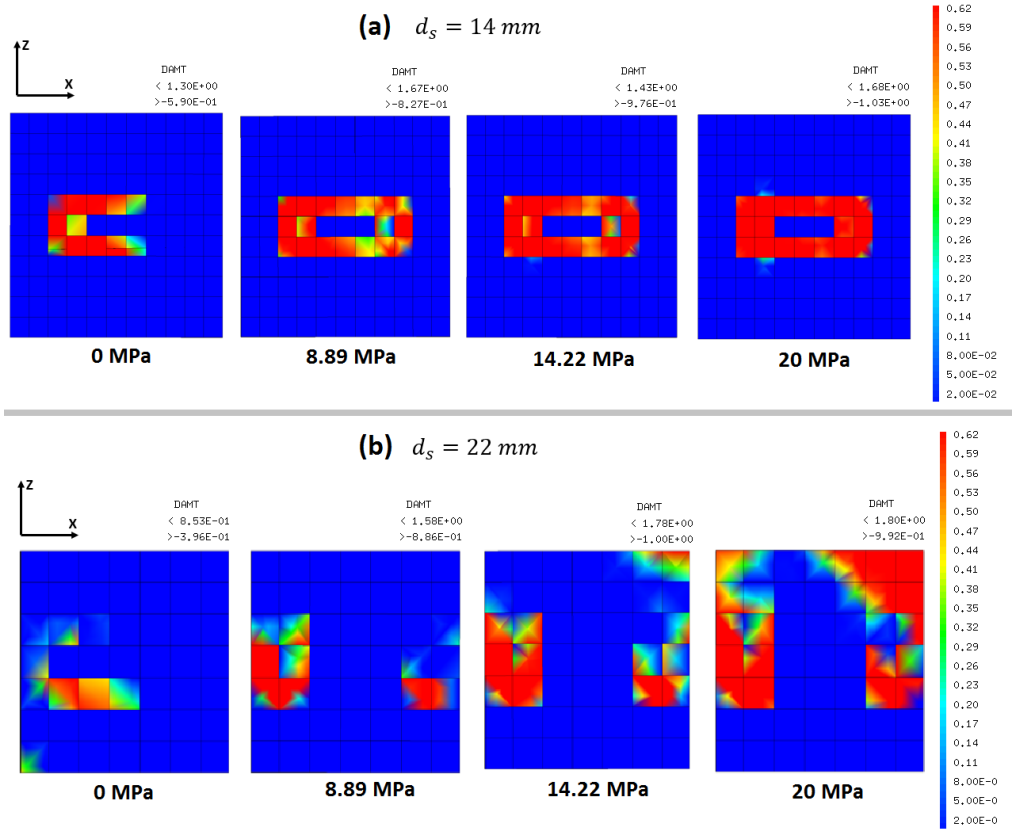

Figure 3.21 Cross-sections of final damage patterns under 0 MPa (no active confinement), 8.99 MPa, 14.22 MPa and 20 MPa lateral compression for: (a) $d_s = 14$ mm, (b) $d_s = 22$ mm.

It can clearly be seen that for $d_s = 14$ mm ($\frac{c}{d_s} = 4.85$) the failure type is pull-out since the damage is localized around the steel. And on the contrary, for $d_s = 22$ mm ($\frac{c}{d_s} = 2.91$) the damage is more spread and tends to show a splitting failure.

As seen in Table 3.10, numerical results are in accordance with experimental test results. The influence of both c/d_s ratio and lateral pressure seems to be well represented in our model.

3.2.3. Pull-Out Test-3: (Xu, Zhimin, et al. 2012)

For the third pull-out test, the experimental campaign of (Xu, Zhimin, et al. 2012) is numerically simulated by using the new bond-slip model under six different lateral compressions proportional to the concrete compressive strength (f_c) which are: no confinement, $0.1f_c$, $0.2f_c, 0.3f_c, 0.4f_c$ and $0.5f_c$. The schematic of the experimental testing system and pull-out specimens are shown in Figure 3.22a and 3.22b. The geometric properties of the specimen are presented in Table 3.11. Properties of steel and concrete are given in Table 3.12 and Table 3.13 respectively.

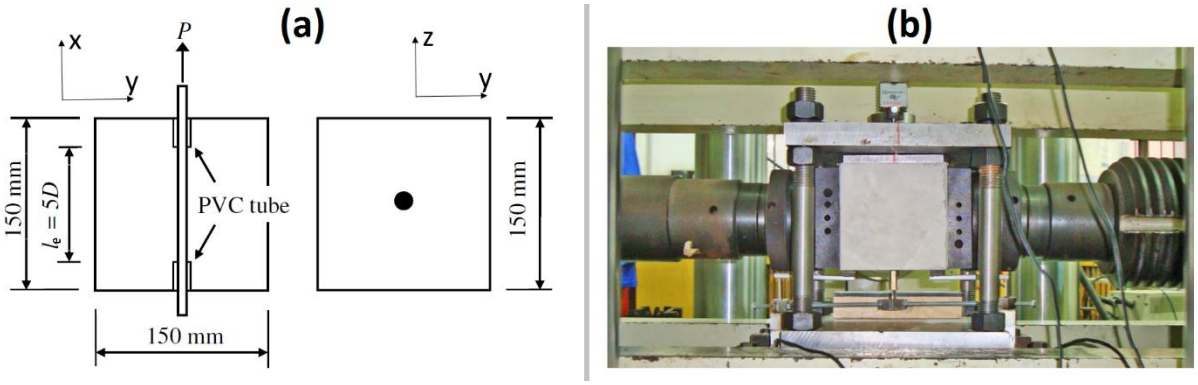

Figure 3.22 (a) Schematic of testing system for pull-out specimen under lateral compressive load. (b) Photo of pull-out specimens (Xu, Zhimin, et al. 2012).

Table 3.11 Geometric properties of (Xu, Zhimin, et al. 2012)' pull-out specimen.

Steel Bar Diameter d_s (mm)	Dimension of the Specimen V_c (mm^3)	Embedment Length l_e (mm)	Concrete to Steel Ratio c/d_s
16	$150 \times 150 \times 150$	$5 \times d_s$	4.18

Table 3.12 Concrete properties of (Xu, Zhimin, et al. 2012)'s pull-out tests.

Young Modulus E_c (GPa)	Poisson Ratio ν_c	Compressive Strength f_c (MPa)	Tensile Strength f_t (MPa)
30.64	0.2	42.5	3.15

Table 3.13 Steel properties of (Xu, Zhimin, et al. 2012)'s pull-out tests.

Diameter d_s (mm)	Young Modulus E_s (GPa)	Poisson Ratio ν_s	Yielding Strength f_y (MPa)	Ultimate Strength f_u (MPa)
16	200	0.3	335	515

Again, for the numerical simulations, the steel is represented by truss elements and the concrete is represented by 3D solid elements with Damage TC model. The mesh of the simulation is arranged to have 5 concrete elements and 10 steel elements along the embedment length (l_e). The mesh geometry of the pull-out simulation and the assumed aleatory tensile concrete strength distribution are presented in Figure 3.23a and 3.23b.

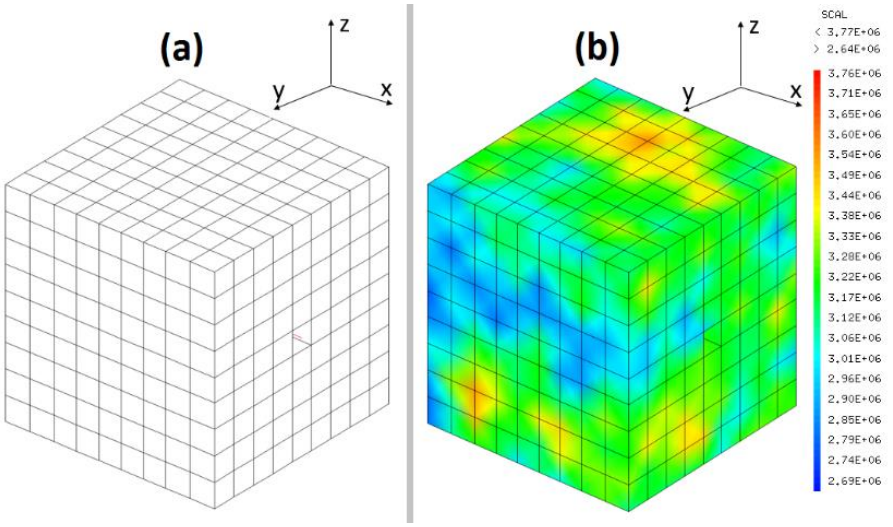

Figure 3.23 (a) Mesh geometry and (b) aleatory strength distribution of the pull-out specimen.

The bottom part is blocked in the z-direction (U_z), the front face is the specimen is blocked in the x-direction (U_x^c) against displacement and lateral pressure is applied on both side surfaces (P_{lat}) of the pull-out specimen as presented in Figure 3.24a. A 12 mm displacement (U_x^s) is imposed on one end of the steel bar along x-direction while the other end of the steel bar remains free. Figure 3.24b shows the input adhesion law which is fitted on the experimental results of (Xu, Zhimin, et al. 2012) for the unconfined case.

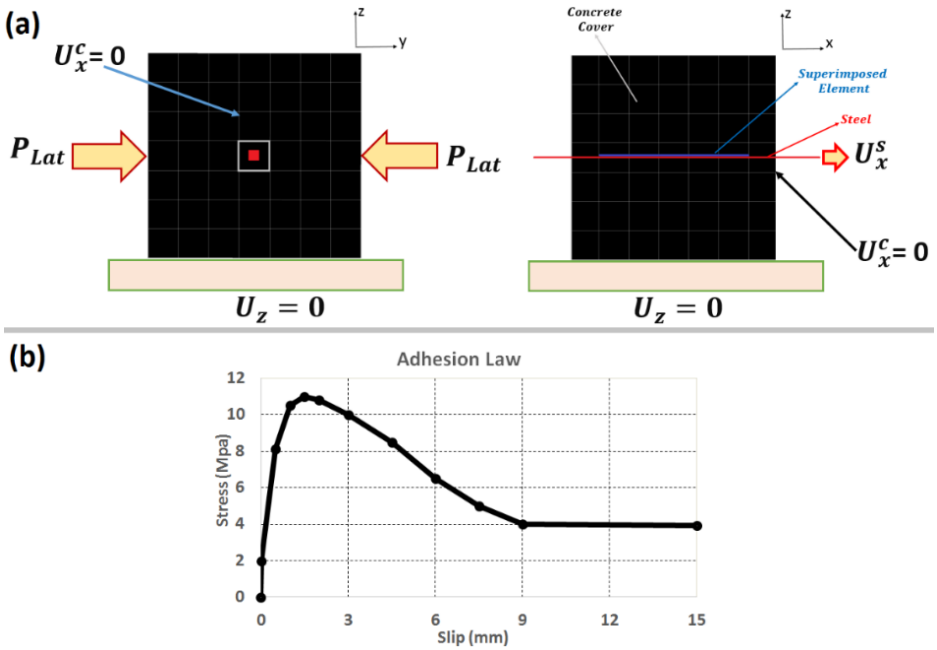

Figure 3.24 (a) Boundary conditions and (b) adhesion law of the pull-out specimen.

Numerical Results

The bond stress-slip response curves of the pull-out simulations under 6 different lateral compressions are presented in Figure 3.25. The comparison of ultimate bond strengths (τ_u) between experimental and numerical results for different lateral pressures (P_{lat}) are given in Table 3.14. The computed lateral pressures along the steel at the time of the peak bond stress are presented on Figure 3.26.

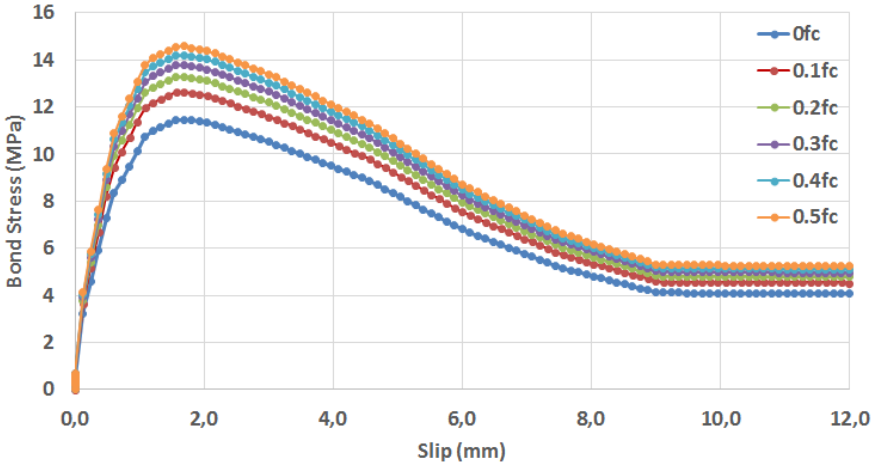

Figure 3.25 Bond stress vs. slip curves of pull-out specimens under lateral compressive stress.

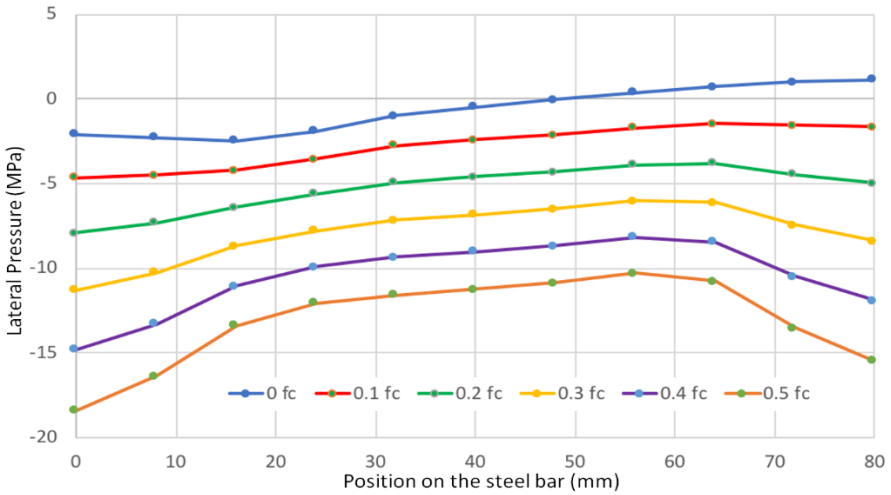

Figure 3.26 Distributions of lateral pressure along the embedded steel at the peak bond stress.

For this (c/d_s), the lateral pressure in the unconfined case is zero in average and the pull-out response in the unconfined case gives the same strength as the input law ($\tau_u = 11.5$ MPa). The confinement pressure, which is well transferred near the steel in lateral pressure, has a significant effect since α has a relatively high value (0.7). The numerical results are in accordance with the experimental ones (Table 4.14).

Table 3.14 Influence of the lateral compression on the bond stress.

	Bond Strength τ_u(MPa)	
Lateral Pressure P_{lat} (MPa)	**Experimental**	**Numerical**
0 $(0 \times f_c)$	10.84 10.10 11.18 12.28	11.47
4.25 $(0.1 \times f_c)$	12.80 12.06	12.64
8.5 $(0.2 \times f_c)$	12.62 12.84 11.45	13.27
12.75 $(0.3 \times f_c)$	12.10 13.28 14.76	13.77
17 $(0.4 \times f_c)$	12.17 12.49 12.46	14.19
21.25 $(0.5 \times f_c)$	14.67 17.74 16.88	14.57

The final damage patterns in the middle cross-section in the z-direction are shown in Figure 3.27.

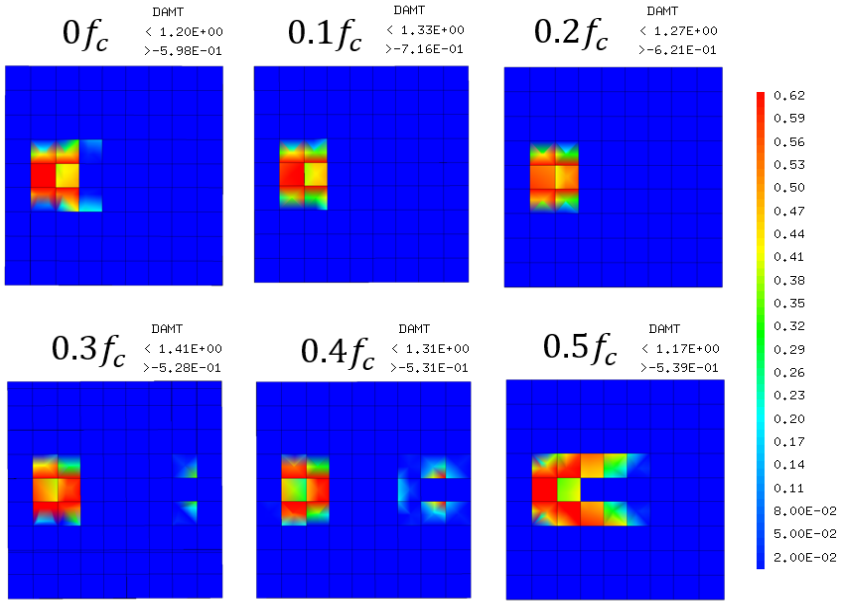

Figure 3.27 Cross-sections of final damage patterns under: $0f_c, 0.1f_c, 0.2f_c, 0.3f_c, 0.4f_c, 0.5f_c$ lateral compression.

The final damage of the concrete cover is increased by increasing lateral compression. The higher the bond strength, the closer the bond behaves as a perfect bond assumption with more homogeneous damage around the steel bar. The damage is concentrated near the free end of the embedded steel, due to the stress concentration.

If all the simulations are considered, the new bond-slip model are provided coherent results with the various experimental pull-out tests ((Xu, Zhimin, et al. 2012), (Torre-Casanova, Jason, et al. 2013) and (Shang, et al. 2017)). The consideration of lateral pressure (P_{lat}), bond properties (adhesion law), concrete properties (f_c and f_t) and concrete to steel ratio (c/d_s) within the new bond-slip model are satisfactory to capture the effect of active confinement on the steel-concrete interface. As a sum up, the proposed formulas (Eq. 3.2 and 3.3) are validated with the experiments.

4. Investigation of the active confinement effect with the new bond-slip model

After validating the new model with various numerical tests, the effect of lateral pressure on local and global structural behaviors are analyzed using the new bond-slip model. The effect

of active confinement on the global and local behavior of the structure is investigated on a tie-rod. For this analysis, a series of numerical tie-rod tests are performed with various external pressure. Thus, the confinement effect on the cracking properties is investigated not only for monotonic loading but also for cyclic loading cases. The new model is then compared with a common industrial assumption so-called perfect bond for the same test cases on the tie-rod.

The tie-rod geometry is presented in Figure 3.28. Yet, the active confinement effect on the tie-rod behavior is tested for 4 different lateral pressure values with no active confinement (0 MPa), 2 MPa, 6 MPa and 10MPa. As presented in Figure 3.28a, the rod is tied on one end (P_0) and the displacement u_x is imposed along the x-direction on the other end (P_3). The lateral pressure is applied on both sides of the concrete beam (P_y and P_z) while the opposite sides of the beam (S_y and S_z) are blocked against the normal displacement (Figure 3.28b). Material properties of the steel and concrete are represented in Table 3.15 and Table 3.16 respectively.

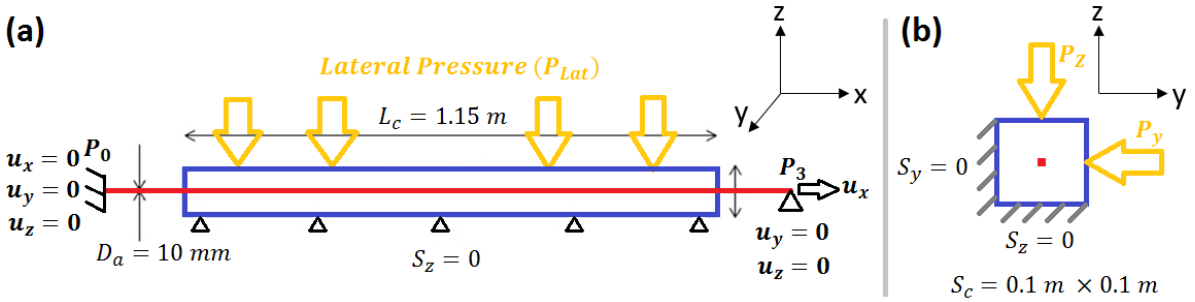

Figure 3.28 Geometry and boundary conditions of the Tie-Rod: (a) Lateral Cross-Section, (b) Vertical Cross-Section.

Table 3.15 Concrete properties of Tie-rod tests.

Young Modulus E_c (GPa)	Poisson Ratio ν_c	Compressive Strength f_c (MPa)	Tensile Strength f_t (MPa)
30.2	0.2	56.9	2.6

Table 3.16 Steel properties of Tie-rod tests.

Young Modulus E_s (GPa)	Poisson Ratio ν_s	Yielding Strength f_y (MPa)	Diameter d_s (mm)
210	0.3	500	10

Calculation of Initial Steel Displacement

In the numerical analysis, the steel rod is represented by 1D truss elements and the concrete is presented by 3D solid elements. When the lateral pressure (P_{lat}) is applied on the structure, due

to the Poisson's ratio of the concrete ν_c, there is a longitudinal strain induced along the x-axis (Figure 3.29):

$$\varepsilon_{xx} = -\nu_c(\varepsilon_{yy} + \varepsilon_{zz}) \tag{3.9}$$

where

$$\varepsilon_{yy} = \varepsilon_{zz} = \frac{P_{lat}}{E_c} \tag{3.10}$$

with E_c is the concrete Young Modulus.

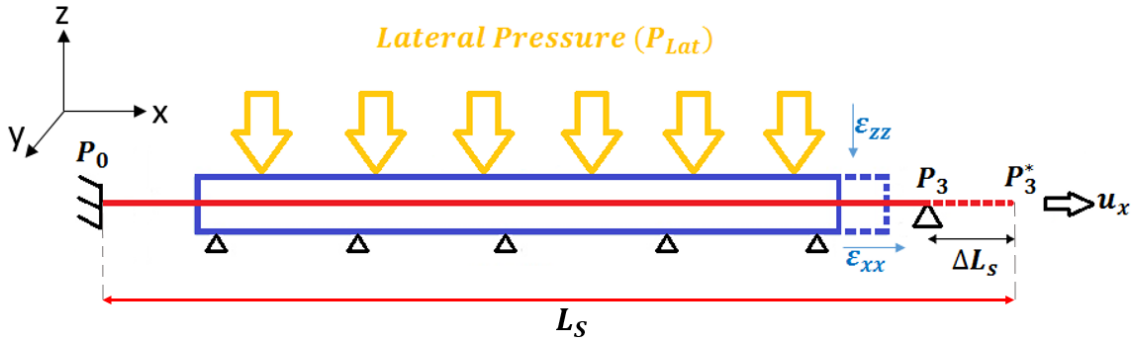

Figure 3.29 Deformation of the tie-rod caused by applied lateral pressure.

On the contrary, the 1D steel elements do not have axial strain under lateral pressure. If nothing is done, the incompatible strains between steel and concrete will cause artificial stresses (tension in the steel, compression and shear in the concrete) which can lead to damage in the concrete, especially when the structure is long, like the tie rod.

To avoid this problem, an initial displacement is imposed to the steel at node (P_3) to impose a strain in the steel equal to the one of the concrete under lateral pressure (Figure 3.29):

$$\Delta L_s = \varepsilon_{xx} L_s = -\nu_c \frac{2P_{lat}}{E_c} \tag{3.11}$$

For compression, $P_{lat} < 0$, and $\Delta L_s > 0$.

This kind of application is not considered in the pull-out test simulations since the embedded length of steel in the concrete was small compared to the tie rod, even if we can observe some perturbations in the lateral pressure at the ends of the embedded steel.

With the application of ΔL_s, there is no stress at the interface between concrete and steel if only the lateral pressure is applied. In the reality, the steel rod has a volume and behave in a 3D way, and

since the Poisson's ratios of steel and concrete are not the same, there are shear stresses at the interface, and the real displacement of the steel may be different of ΔL_s. To test this, a full 3D simulation has been performed. One-quarter of the tie-rod is modeled. Tension-compression damage model (Damage TC) is used for the concrete. Mesh geometry and the aleatory tensile strength distribution for 3D steel rod simulations are presented in Figure 3.30. For the steel-concrete interaction, the perfect bond assumption is used.

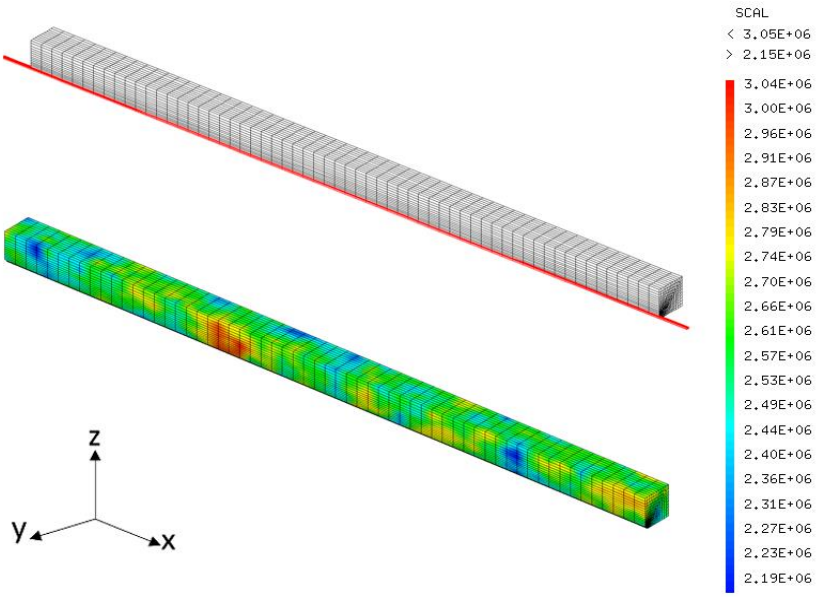

Figure 3.30 Mesh geometry and aleatory strain distribution of 3D steel representation simulation of the tie rod.

The initial displacement values which are calculated from Eq. 3.11 are compared with the numerical results of the 3D steel simulations are presented in Table 3.17.

Table 3.17 Initial displacements for 1D and 3D steel representations.

	Initial Steel Displacement (µm)	
Lateral Pressure P_{lat} (MPa)	**1D Steel**	**3D Steel**
0	0	0
2	32.89	28.74
6	98.68	86.23
10	164.47	143.73

The differences between 1D steel and 3D steel are rather small. In the flowing ΔL_s is imposed at the beginning while applying the lateral pressure. Then an additional displacement is imposed to load the tie rod. To take into account the initial stress in the steel in the behavior law of the steel and avoid

premature yielding, the plastic threshold is shifted according to ΔL_s value. All the force-displacement curves in the following are presented with the true imposed displacement (withoutΔL_s).

4.1. Monotonic loading

The first batch of simulations on the tie-rod is performed under monotonic loading. 2 mm displacement (u_x) is imposed on one end of the steel rod (P_3 point) along the x-direction which is presented in Figure 3.28. The active confinement effect on the structural behavior is tested for four different conditions with: 0 MPa (no confinement), 2 MPa, 6 MPa and 10 MPa lateral compression. The steel-concrete interaction is represented in two manners: bond-slip model and perfect bond hypothesis. The material properties of the steel and concrete are taken as in Table 3.15 and Table 3.16 respectively.

For the numerical analysis of the pull-out specimen, the steel is represented by 1D truss elements and the concrete is represented by 3D solid elements with Damage TC model. The mesh geometries of the tie-rod simulations and the assumed aleatory tensile concrete strength distribution are presented in Figure 3.31.

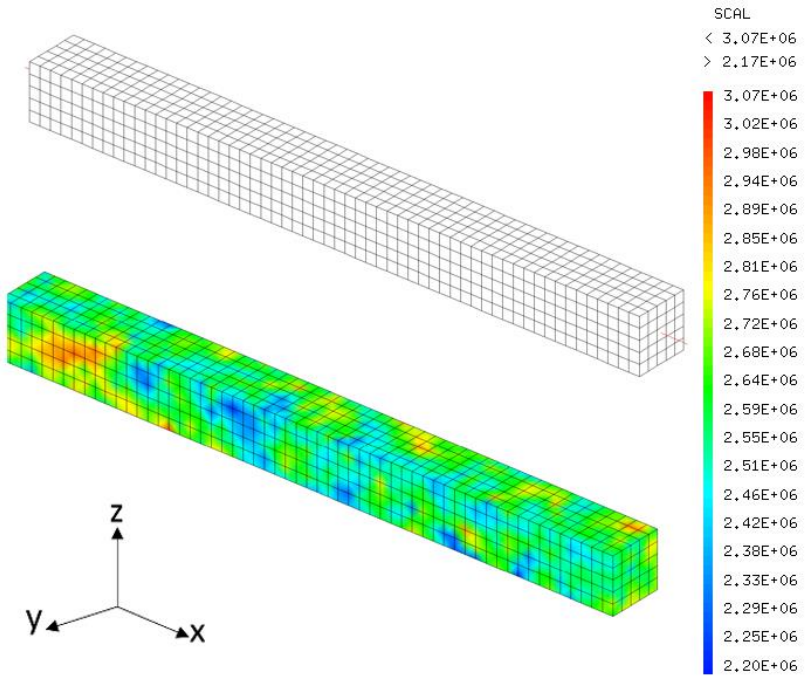

Figure 3.31 Mesh geometry and aleatory strain distribution of the 1D steel representation simulation on the tie rod.

Force-displacement curve and final damage properties of the structure for the perfect bond model simulations are presented in Figure 3.32 and Figure 3.33 respectively.

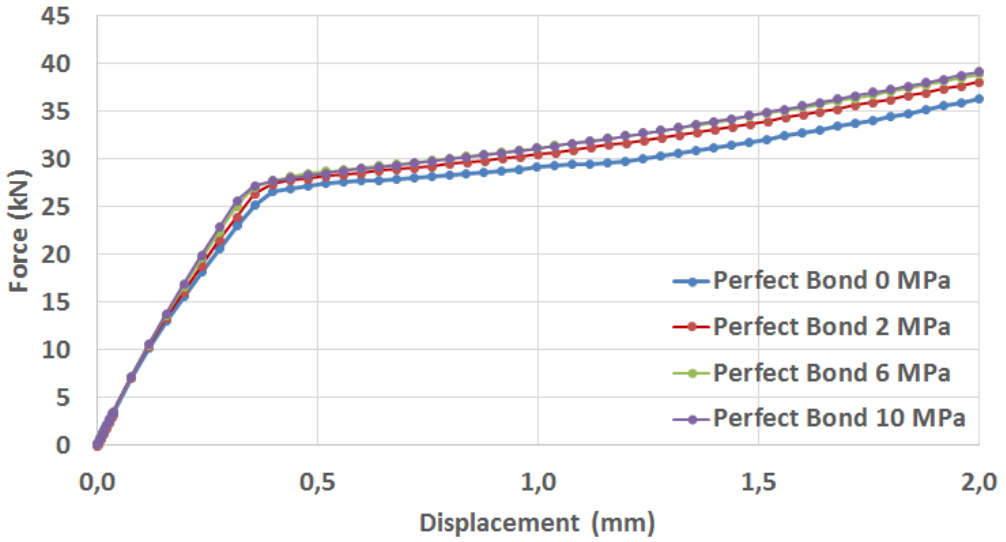

Figure 3.32 Force-displacement curve of the monotonic perfect bond model simulations on the tie-rod.

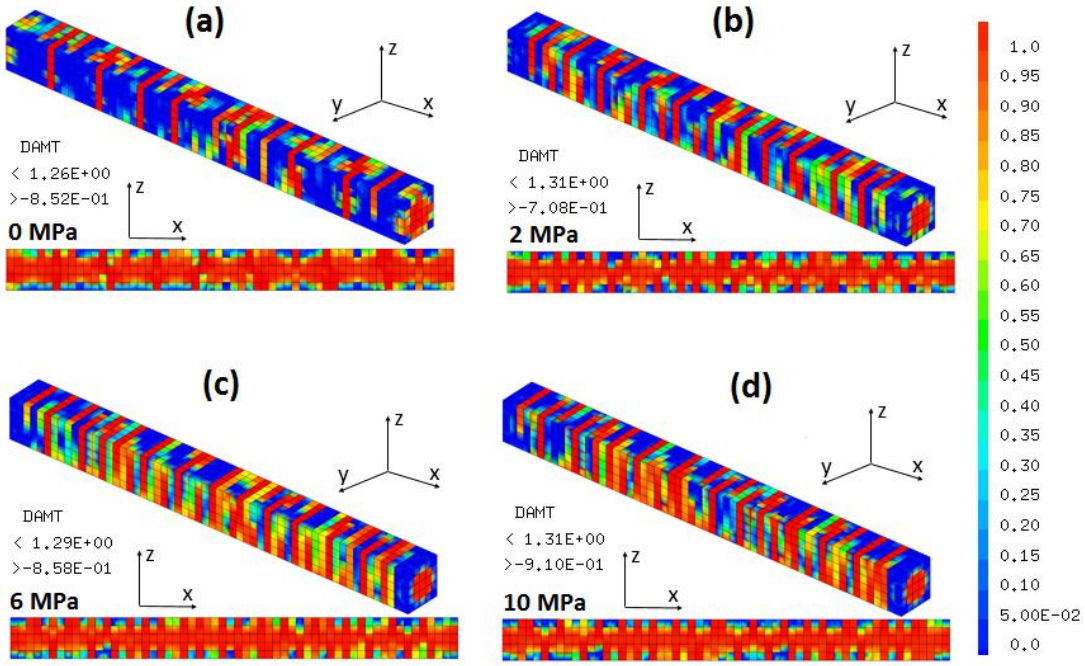

Figure 3.33 Final damage patterns of monotonic perfect bond simulations on the tie-rod under: (a) no confinement, (b) 2 MPa lateral compression, (c) 6 MPa lateral compression and (d) 10 MPa lateral compression.

As it can be seen from Figure 3.32, the force is slightly increased by increasing lateral compression on the structure. This slight increase is originated from the consideration of the confinement effect within the concrete behavior (Damage TC model).

Figure 3.33 represents the final damage patterns of the structure and its cross-section along the y-axis. For all cases, the center of the concrete beam is totally damaged since the same displacement is assumed for both steel and concrete (perfect bond hypothesis). Thus, surface

damage is observed on the surfaces where the lateral pressure has been applied for the cases 2 MPa, 6 MPa and 10 MPa lateral compression.

For the bond-slip model simulations on tie-rod, force-displacement curve, final damage properties and slip between the steel and concrete are presented in Figures 3.34, 3.35 and 3.36 respectively.

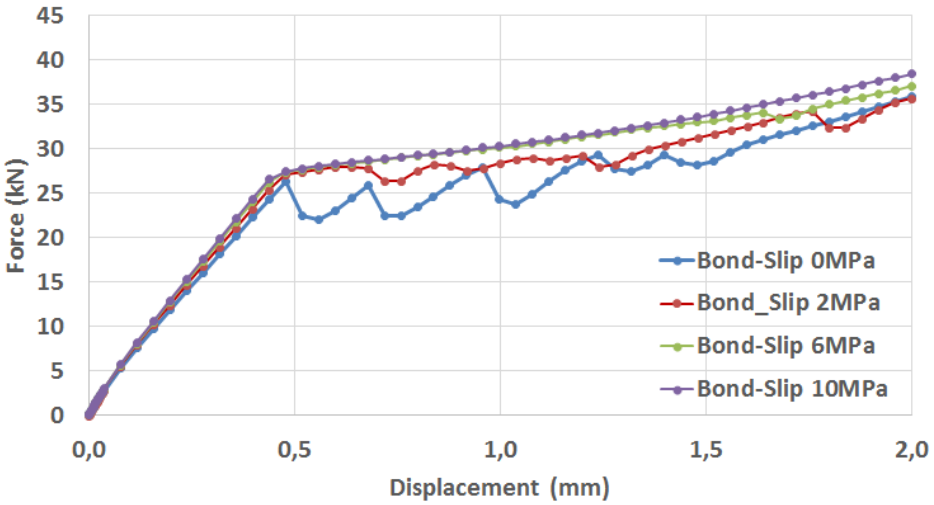

Figure 3.34 Force-displacement curve of the monotonic bond-slip model simulations on tie-rod.

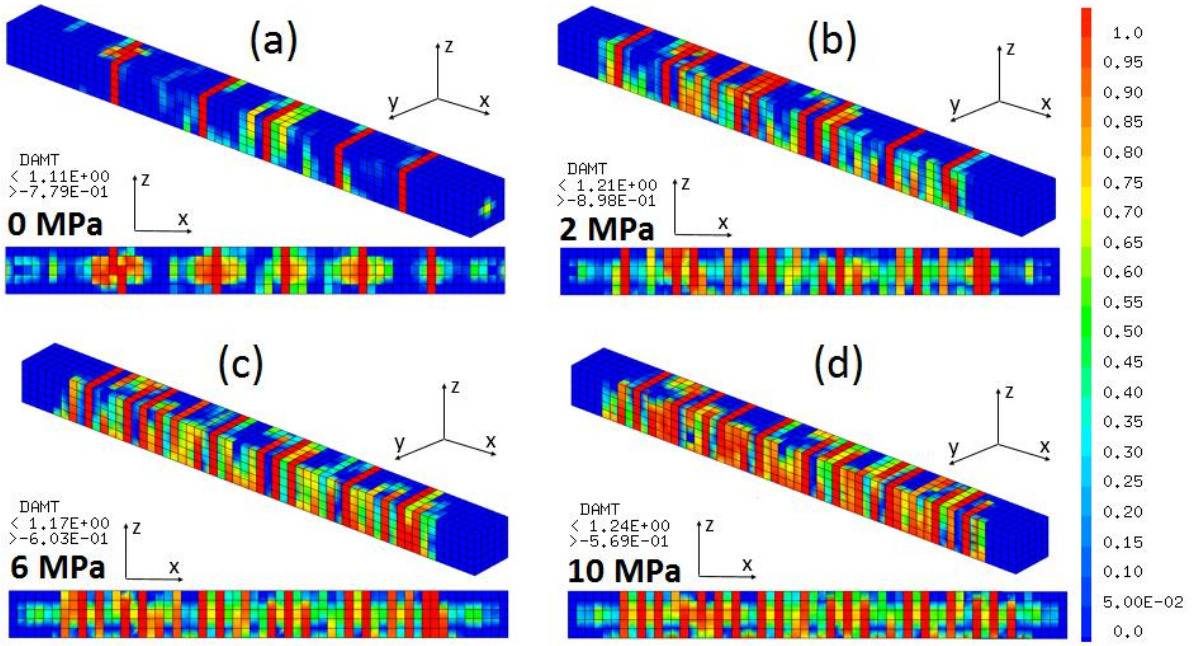

Figure 3.35 Final damage patterns of monotonic bond-slip model simulations on the tie-rods with under: (a) no confinement, (b) 2 MPa lateral compression, (c) 6 MPa lateral compression and (d) 10 MPa lateral compression.

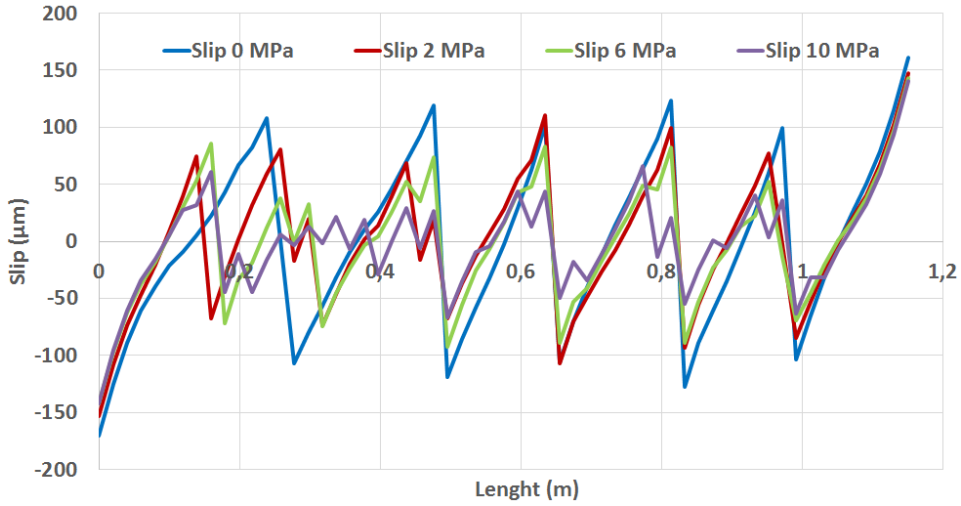

Figure 3.36 Final slip between steel and concrete for monotonic bond-slip model simulations on tie-rod.

As it can be seen from Figure 3.34, the force is increased by increasing lateral compression on the structure as in the perfect bond hypothesis. Moreover, using the bond-slip model also enables to observe force-drops at the cracking instances. In no-confinement case, these drops are more significant compared to other simulations where the lateral pressure exist. The force-displacement curve becomes smoother with increasing lateral pressure. This means that the bond-slip model behavior approaches the perfect bond behavior when the lateral compression increases. For 10 MPa lateral pressure, the general behavior of two simulations with bond-slip model and perfect bond assumption are almost the same.

When the final damage patterns are compared for the bond-slip model simulations which are represented in Figure 3.35, the crack locations are only significant for the no confinement case. With increasing lateral pressure, it is quite difficult to determine the crack locations only by using the damage geometries of concrete cover. This may be caused by the increase in bond strength. The higher the bond strength, the closer the bond behaves as a perfect bond assumption with more homogeneous damage is observed around the steel bar.

The final slip values between steel and concrete are represented in Figure 3.36. The slip sign changes at the crack locations. Only 5 cracks are observed for the no-confinement case, while 6 cracks are observed for 2 MPa and 6 MPa lateral pressure simulations. As mentioned in the previous section, the ultimate bond strength (τ_u) is increasing with increasing lateral compressive stress (P_{lat}). Up to a certain level ($P_{lat} < 6$ MPa), the cracks can be determined easily by the slip sign change along the steel rod. After that ($P_{lat} > 6$ MPa), the mechanical degradation is distributed along the interface and localized cracking cannot be observed

anymore (like in the $P_{lat} = 10$ MPa case). This means the local behavior (cracking properties) is also affected by active confinement which is considered in the new bond-slip model.

4.2. Cyclic loading

For the second series of simulation, an alternative loading is applied in terms of imposed displacement on the tie rod to observe the irreversible behavior of the structure under active confinement. Same geometry, boundary conditions and material properties are chosen as in the previous test series which is presented in Figure 3.28. The material properties of the steel and concrete are taken as in Table 3.15 and Table 3.16 respectively. The mesh geometries of the tie-rod simulations and the assumed aleatory tensile concrete strength distribution are taken as in Figure 3.31. For the numerical analysis of the pull-out specimen, the steel is represented by truss elements and the concrete is represented by 3D solid elements with Damage TC model. The steel-concrete interaction is represented in two manners: bond-slip model and perfect bond hypothesis. Again, the simulations are performed with bond-slip and perfect bond models for various lateral pressure values (no confinement, 2 MPa, 6 MPa and 10 MPa). The results of the two interface models are compared with each other.

Force-displacement curves and final damage patterns of the structure for the perfect bond model simulations are presented in Figures 3.37 and 3.38 respectively.

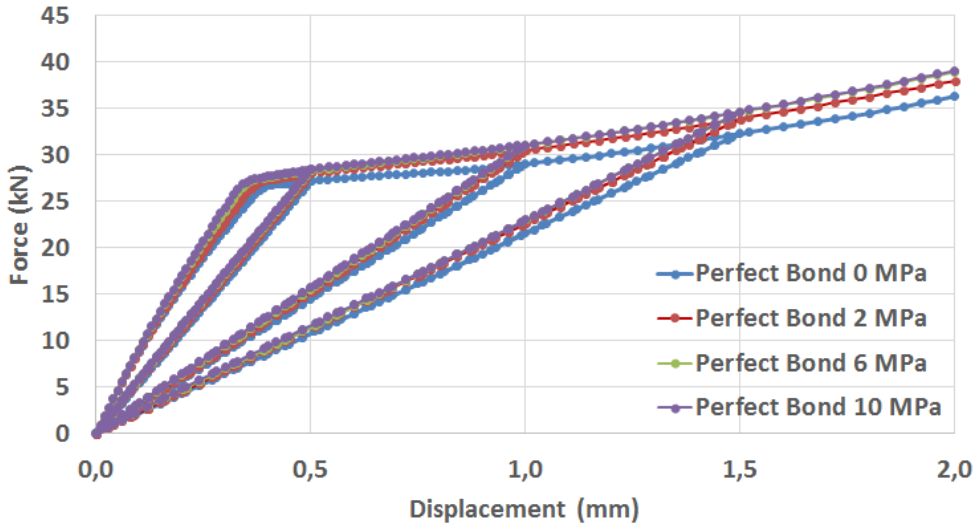

Figure 3.37 Force-displacement curve of the cyclic perfect bond model simulations on tie-rod.

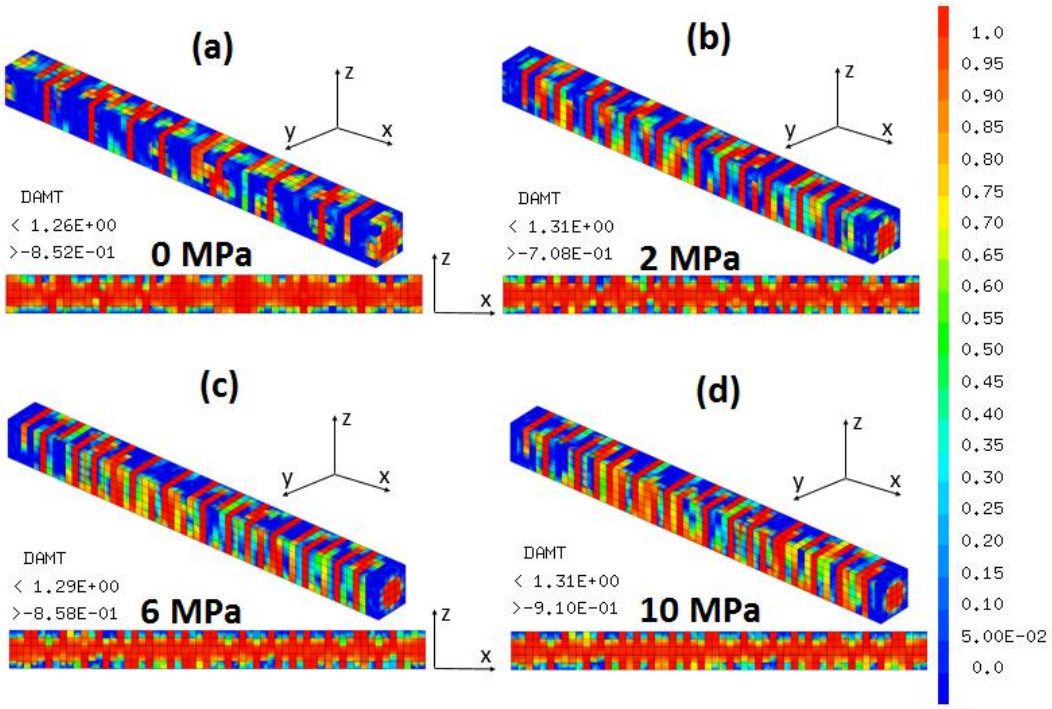

Figure 3.38 Final damage patterns of cyclic perfect bond model simulations on the tie-rods with under: (a) no confinement, (b) 2 MPa lateral compression, (c) 6 MPa lateral compression and (d) 10 MPa lateral compression.

As it can be seen from Figure 3.37, the force is slightly increased by increasing lateral compression on the structure as in the monotonic case due to the concrete behavior in compression. There is no irreversible behavior of the structure (remaining strain for zero stress) when the perfect bond assumption is used.

Figure 3.38 represents the final damage patterns of the structure and its cross-section along the y-axis. For all the cases, the center of the concrete beam is totally damaged like in the monotonic case since the same displacement is assumed for both steel and concrete.

For the bond-slip model simulations on tie-rod under cyclic loading, force-displacement curve, final damage properties, slip between the steel and concrete are presented in Figures 3.39, 3.40 and 3.41 respectively.

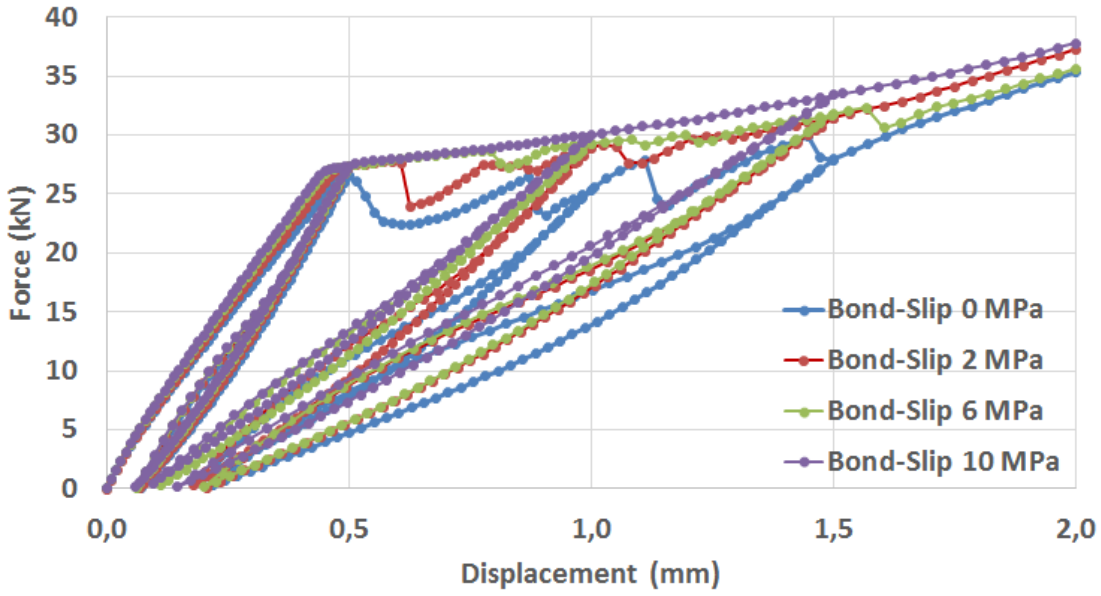

Figure 3.39 Force-displacement curve of the monotonic bond-slip model simulations on tie-rod.

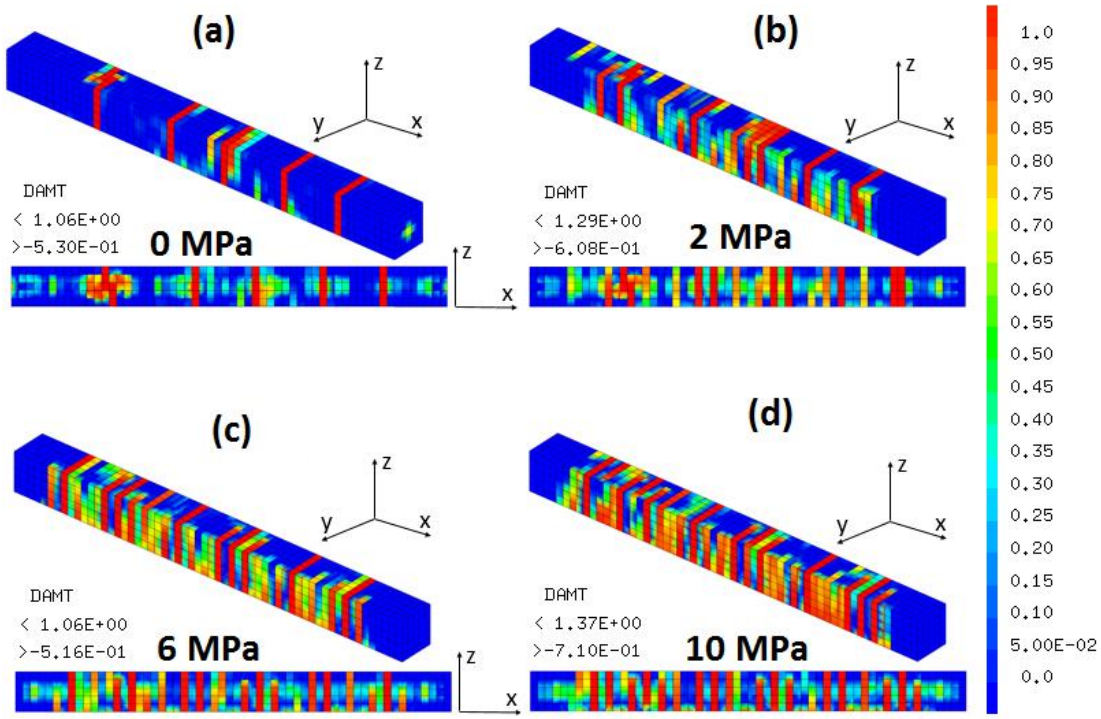

Figure 3.40 Final damage patterns of monotonic bond-slip model simulations on the tie-rods with under: (a) no confinement, (b) 2 MPa lateral compression, (c) 6 MPa lateral compression and (d) 10 MPa lateral compression.

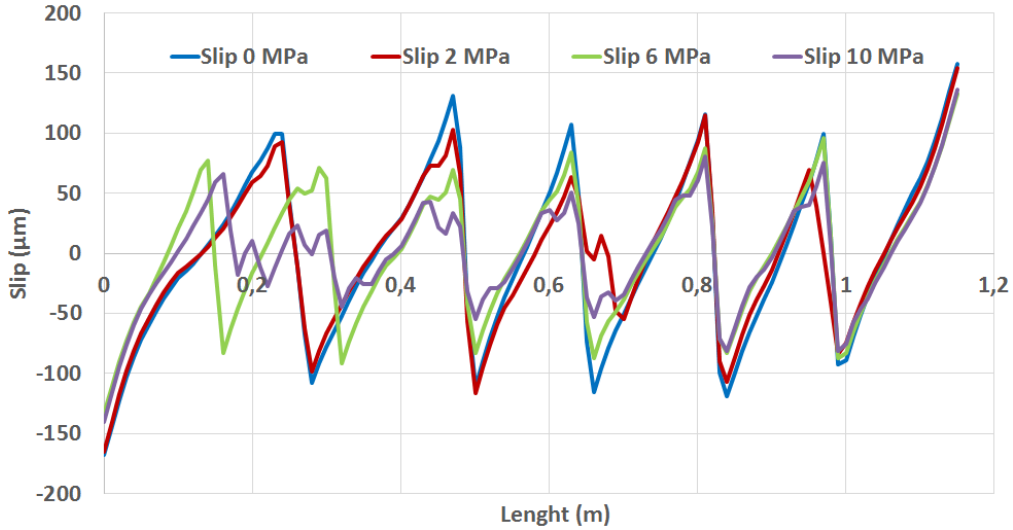

Figure 3.41 Final slip between steel and concrete for cyclic bond-slip model simulations on tie-rod.

As seen in Figure 3.39 there is an irreversible behavior of the structure under active confinement when the bond-slip model is used. The irreversibility of the structural behavior is decreased by increasing lateral compression due to the increase in the bond strength. Again, force drops become smoother by increasing active confinement, as in the monotonic case, since the bond-slip model is nearer the perfect bond.

On the final damage patterns (Figure 3.40) the crack locations are only significant for the no confinement case. With increasing lateral pressure, it is quite difficult to determine the crack locations only from the damage patterns of concrete cover as in the monotonic case. Again, this can be originated from the increase in bond strength. The higher the bond strength, the closer the bond behaves as a perfect bond assumption, with a more homogeneous damage observed around the steel bar.

The final slip between the steel and concrete are rather different from the monotonic case (Figure 3.41). Only 5 cracks are observed in total for no confinement and 2 MPa lateral pressure cases, while 6 cracks are observed for 6 MPa lateral pressure case. This may be originated from the crack closing during the reloading stage of the cyclic load (see below).

To understand the effect of active confinement on the local structural behavior (cracking properties), single loading (point A) and reloading (point B) are applied on the identical tie-rod for no confinement (0 MPa) and lateral pressure under 2 MPa. The force-displacement curve and the slip along the steel at the loading (point A) and reloading (point B) are presented in Figure 3.42 and 3.43.

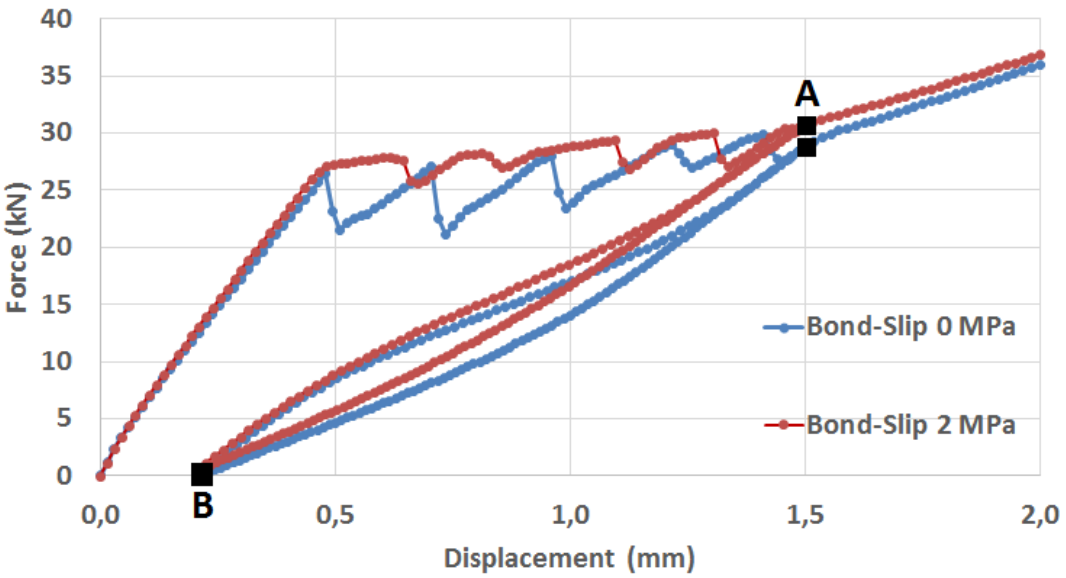

Figure 3.42 Force-displacement curve of the cyclic bond-slip model simulations on tie-rod under 0 MPa and 2 MPa lateral pressure.

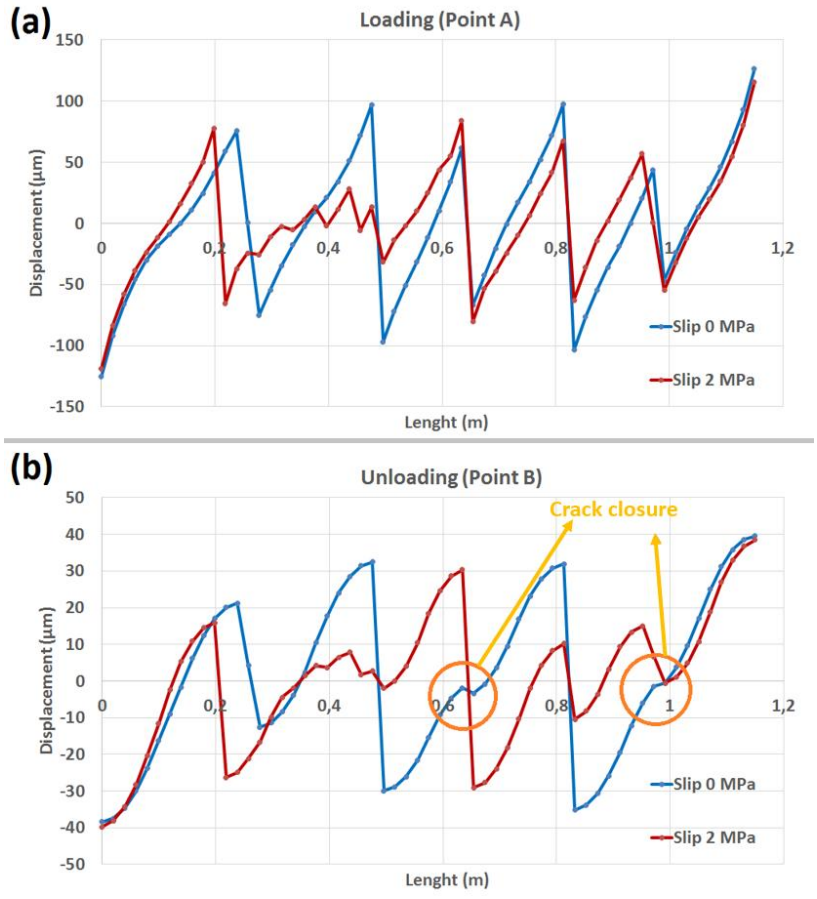

Figure 3.43 Demonstration of crack closure at (a) loading and (b) unloading steps.

As mentioned earlier the change in the slip sign demonstrates the crack locations. At the loading point (A), 5 crack occurrences are observed for no confinement and 2 MPa simulations (Figure 3.43a). At the unloading point (B), the 5 cracks remain (less open) for the 2 MPa case, but only

3 cracks remain for no confinement case (Figure 3.43b). The two closed cracks for the no confinement case can be seen in Figure 3.43b. The increase in the bond strength for 2 MPa simulations is prevented the crack closure unlike in no confinement simulation.

5. Conclusion

In this chapter, the implementation and the validation of the active confinement effect on the new bond-slip model are explained in details.

Firstly, the implementation of the active confinement effect to the bond-slip model is presented with suggested formulations (Eq. 3.2 and 3.3). Afterward, implementation methodology is tested on a single interface element for monotonic and cyclic loading cases under various lateral pressures. The results have shown that the active confinement effect on the steel-concrete interface is implemented correctly into the bond-slip model.

Secondly, four different pull-out specimens from three different experimental campaigns ((Xu, Zhimin, et al. 2012), (Torre-Casanova, Jason, et al. 2013) and (Shang, et al. 2017)) with different embedment lengths, concrete covers, steel diameters, lateral pressures, adhesion laws, material properties (steel and concrete) and bond strength (strong and weak) are tested. Coherent results are obtained between the simulations and the experiments for both test cases. The implemented active confinement formulas (Eq. 3.2 and 3.3) are validated.

Finally, the new bond-slip model is used to examine the active confinement effect on the structural behavior by performing a series of numerical analysis on a tie-rod. Moreover, the results are compared with the perfect bond assumption for 1D steel representations in order to see the significance of the model. The local and global behavior of the tie-rod under various lateral pressures are compared for monotonic and cyclic loading cases.

For the global behavior of the tie-rod, the force drop cannot be observed with the perfect bond model. It is only possible for the bond-slip model. When the lateral compression is increased, the drops become smoother and bond slip model approaches the perfect bond behavior. This is originated from the increased bond strength due to the lateral pressure. No irreversibility is observed with the perfect bond assumption. It is again only possible with the new bond-slip model.

For the local behavior of the tie-rod, discrete cracks are observed in the bond-slip model simulations compared to the perfect bond model simulations. Besides, the position of cracks can be more clearly identify from slip between steel and concrete when it changes its sign. Less slip is observed at high lateral pressure due to the increased bond strength for both monotonic and cyclic cases. Moreover, the new bond-slip model enables to observe the active confinement effect on the crack closure under alternative loads. It has been observed that the increase in lateral compression prevents the crack closure.

As a sum up, the active confinement effect on the global and local structural behavior can be correctly represented for monotonic and cyclic loading cases when the new bond-slip model is used.

Chapter-4:
Investigation on Dowel Action with New Bond-Slip Model for Reinforced Concrete Structures

1. Introduction

In this chapter, the shear behavior of reinforced concrete structures is investigated specifically focusing on the dowel action. As mentioned in the first chapter, the dowel action is not easily presented numerically due to certain difficulties and its effect on the structural behavior is not estimated clearly in the literature. A detailed numerical analysis is needed to represent the dowel action.

The main objective of the section is to evaluate the existing approaches of modeling to capture experimental dowel action. For this reason, different reinforcement models (truss and beam elements) and steel-concrete interface models (bond-slip model and perfect bond model) are compared by reproducing different experimental campaigns.

Firstly, some considerations are exposed to the modeling of steel reinforcement related to dowel action phenomena. A calibration process has been performed on the nonlinear behavior of beam elements. Secondly, the pure dowel action is investigated with a push-off test which can be found in the literature ((Sagaseta and Vollum 2011), (Xiao, Li and Li 2014), (Navarro-Gregori, et al. 2016) etc.). Based on the experimental campaign, the new bond-slip model is compared with the perfect bond hypothesis and experimental results to determine the model efficiency to represent the local and global behavior of the reinforced structures. Moreover, 1D truss and beam element steel representations are compared. Finally, the shear behavior of relatively large structures like deep beams is investigated by using the new bond-slip model. Again, a comparison has been made on different bond and reinforcement models to capture the experimental local and global structural behavior numerically.

2. Steel Model

Before going into any detailed investigation on shear behavior of reinforced concrete structures, a proper calibration process is necessary on the models which will be used. In this section, after some considerations about truss and beam 1D elements, the calibration of the steel beam model is explained in detail.

Since our final goal is to numerically simulate the behavior of industrial large structures, the detailed 3D modeling of reinforcement is not considered, it would lead to too heavy meshing work and computation time. The alternative is to use 1D elements since the reinforcement bars are very slender (high length compared to cross-section). Among classical 1D elements, we can choose truss or beam elements.

Truss elements behave only along their axis, in tension or compression (equivalent to spring), they cannot support transverse shear or bending. They have only translation degrees of freedom and can easily be connected to solid 3D elements which also have no rotational DOFs. In most applications of reinforced concrete structures, truss elements are sufficient to represent the global behavior of steel reinforcement. Indeed, it works mainly in tension-compression. Moreover, the nonlinear behavior of these elements is easy to model. Non-linear forces are directly calculated from the 1D stress-strain law by multiplying by the cross-sectional area.

When considering local particular behavior, like dowel action, truss elements may not be sufficient. The beam elements should be better to recover the transverse shear force and to model the bending of reinforcement through the concrete cracks. There are two issues to pay attention to when using such elements.

First, when beam elements are embedded in a 3D solid elements mesh, one has to be aware that the rotational degrees of freedom of the beam are not connected to the solid elements which have only translation DOFs. Thus, the steel reinforcement is modeled like a multi-supported beam where the supports are the nodes of the steel elements. The contact between steel and concrete along the beam element is not modeled. The transverse displacement due to rotations at the nodes (Figure 4.1) is only related to the beam element flexural rigidity. Moreover, if the reinforcement bar is straight, the rotation around its axis is free and must be prevented with boundary conditions to avoid singularity in the solving matrix.

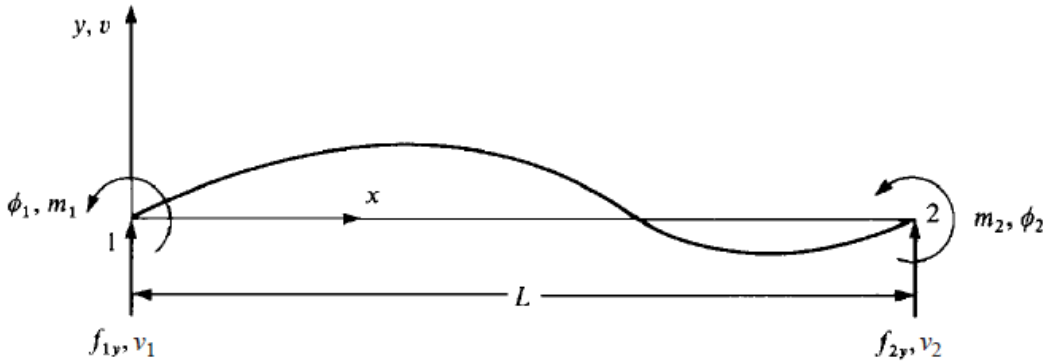

Figure 4.1 Transverse displacement of a beam element (Logan 2012).

The second issue is the nonlinear behavior of the steel beam element. Indeed, the beam can yield in bending. To avoid the use of multifiber elements which have multiple integration points in the cross-section, but increase the computation time, there is a simplified elastic perfectly plastic approach in (Cast3M 2017). It is based on the computation of the axial stress at a point in the cross-section, and by applying the Von Mises criterion at this point. The plastic moment (plateau on the moment-curvature curve) is reached when the stress at this point reaches the yield limit σ_{eq}. The position of the yielding point is given in the input file (it is chosen by the user). The coordinates of this point in the cross-section must be selected carefully to obtain the more realistic nonlinear bending behavior of the beam, depending on the beam cross-section shape.

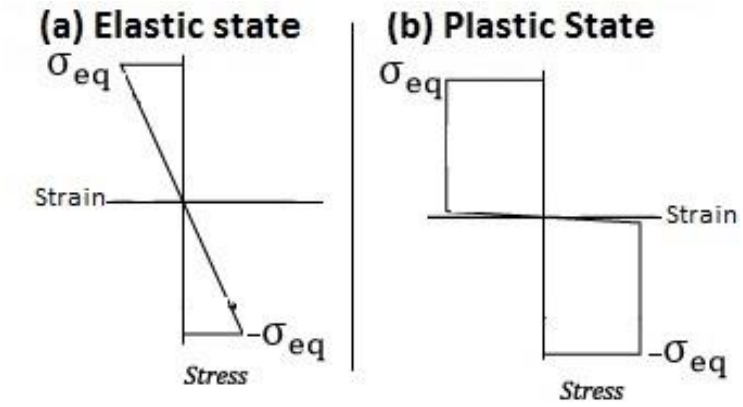

Figure 4.2 Stress diagram of a beam in bending (Codcogs 2016).

For example, in 2D, let's denote y_{pl} the distance between the axis of the beam and the plastic point. In elasticity, when the stress at this point reaches the yield limit, we have (Figure 4.2a):

$$\sigma_{eq} = -\frac{M_{eq}\, y_{pl}}{I_z} \tag{4.1}$$

where M_{eq} is the plastic bending moment (transition from elasticity to plasticity), and I_z the quadratic moment around z-axis. For a bar with a circular cross-section:

$$I_z = \pi \frac{d_s^4}{64} \tag{4.2}$$

For totally yielded cross section (Figure 4.2b):

$$M_{eq} = \int \sigma(y)\, y\, dS \tag{4.3}$$

with, for a positive bending moment:

$$\begin{cases} \text{if } x \geq 0 & \sigma(x) = -\sigma_{eq} \\ \text{if } x < 0 & \sigma(x) = +\sigma_{eq} \end{cases} \tag{4.4}$$

Since the static moment for a half disc is equal to $\frac{d_s^3}{12}$, Eq. 4.5 can be rearranged as:

$$M_{eq} = -2\, \sigma_{eq} \frac{d_s^3}{12} \tag{4.5}$$

Combining Eq. 4.1 and Eq. 4.5, it comes:

$$M_{eq} = -\sigma_{eq} \frac{d_s^3}{6} = -\frac{\sigma_{eq}\, I_z}{y_{pl}} \tag{4.6}$$

and:

$$y_{pl} = \frac{6\, I_z}{d_s^3} = \frac{6}{d_s^3} \times \frac{\pi d_s^4}{64} = \frac{3}{32}\, \pi d_s \tag{4.7}$$

As a conclusion, if x_{pl} is chosen following Eq. 4.7, the plastic moment (limit of elasticity) corresponds to a total plasticization of the section.

Bending Beam Test

A simple bending test is simulated to validate the choice for the "x_{pl}" parameter. Two simulations (one with beam elements and one with multi-fiber element approaches ((Mazars, Ragueneau , et al. 2004) (Kontronis and Mazars 2005)) are performed. The multi-fiber cross-section of the bar is presented in Figure 4.3.

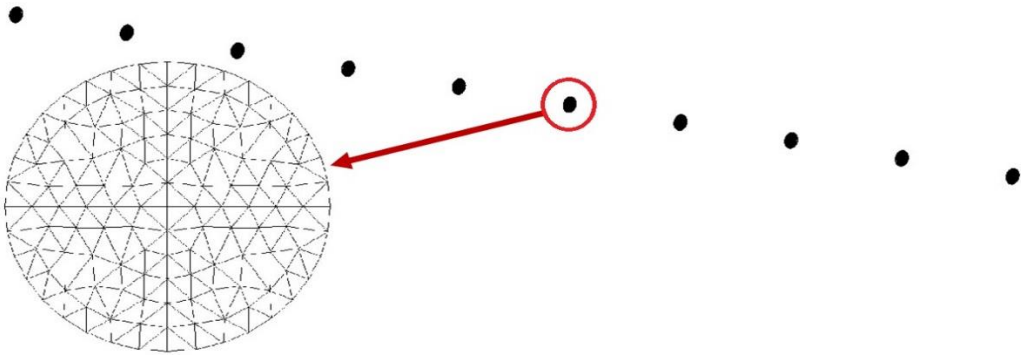

Figure 4.3 Fiber element model of the steel beam.

A 1 m length steel bar with 10 elements is chosen for the reference geometry. The material properties of the steel bar can be found in Table 4.1. One end of the bar is clamped and a 40 cm displacement is applied along the vertical direction on the free end of the bar. Applied boundary conditions are presented in Figure 4.4.

Table 4.1 Steel Properties.

Diameter d_s (mm)	Length of the Steel Bar L (m)	Young Modulus E_s (GPa)	Poisson Ratio ν_s	Yielding Strength f_y(MPa)	Ultimate Strength f_u(MPa)
12	1	200	0.3	440	490

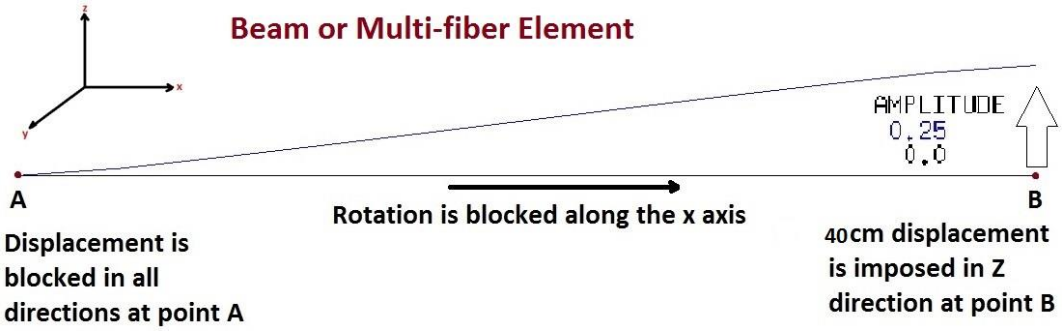

Figure 4.4: Initial and final deformed shapes of the steel beam with boundary conditions.

Force vs. displacement curves of both simulations are given in Figure 4.5.

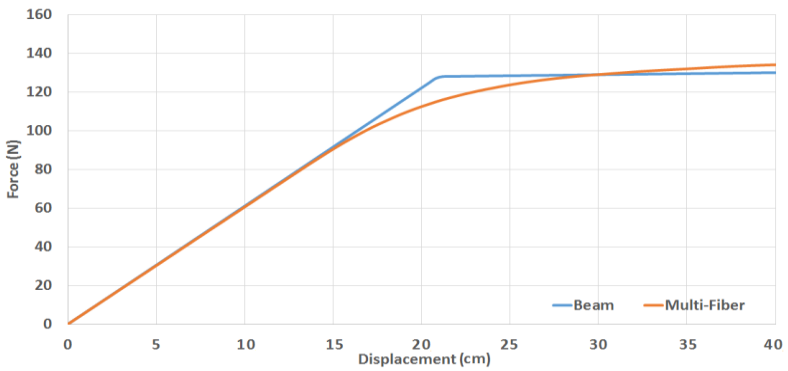

Figure 4.5: Force vs displacement curve of bending steel bar.

The two simulations are giving similar results when the appropriate y_{pl} values are chosen. As a sum up, the beam nonlinear behavior is validated by comparing to the multi-fiber approach.

3. Push-Off Test on an L-Beam

In this section, the pure dowel action is investigated by analyzing an experimental campaign numerically. Different bond and reinforcement models are yet compared with the experimental results to find out the realistic representation of dowel action.

Experimental Test Setup

Pure dowel action can be observed only if the shear cracks are widened to a certain amount. Therefore, a pre-cracked geometry is chosen which eliminates aggregate interlock. As mentioned in the first chapter, L-beam geometry is a good choice for this purpose. It is commonly used in literature ((Walraven and Reinhardt 1981), (Soroushian, et al. 1986), (Lee and Hong 2015) etc.). Experimental push-off test campaign of (Ince, Yalcin and Arslan 2007) on L-beams is used as a reference geometry for this study. The dowel action is investigated for different steel bar angles. The geometrical properties of these test specimens are presented below.

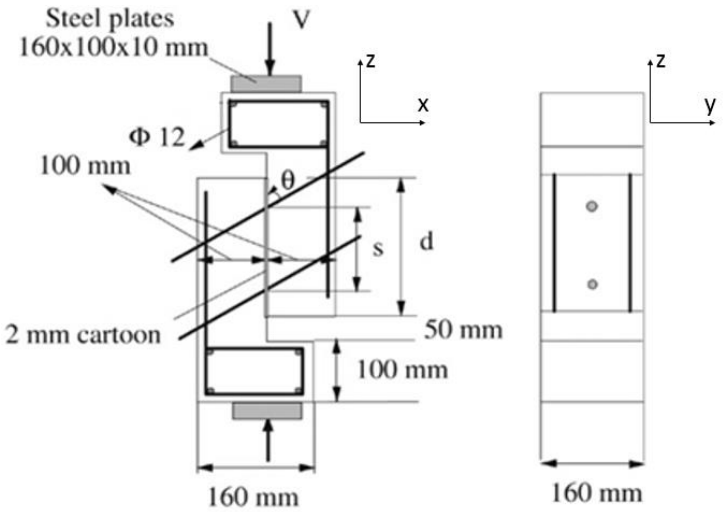

Figure 4.6 Geometric properties of L-beam specimen (Ince, Yalcin and Arslan 2007).

L-beam specimens have 2 mm distance between the two concrete blocks to represent the pre-cracked area. The shear force that is applied along the vertical direction (V) on the top surface, transfers only through dowel action in the cracked section of the structure. This kind of specific geometry makes it possible to observe pure dowel action. Experimental results of the push-off

tests are represented in Table 4.2. Material properties of the concrete and steel are presented in Table 4.3 and 4.4 respectively.

Table 4.2 Geometrical properties of L-beam and experimental results of the Push off test (Ince, Yalcin and Arslan 2007).

$\theta(°)$	$s(mm)$	$d(mm)$	V_u (kN)
45	100	160	1) 45.7 2) 40.6 3) 43.1
90	100	160	1) 35.8 2) 47.6 3) 43.8

where s is the spacing of the transverse reinforcement, d is the specimen size, θ is the elongation angle and V_u is the ultimate force.

Table 4.3 Material Properties of Concrete (Ince, Yalcin and Arslan 2007).

Young Modulus E_c (GPa)	Poisson Ratio ν_c	Compressive Strength F_c (MPa)	Tensile Strength F_t (MPa)
23.64	0.2	25.3	2.53

Table 4.4 Material Properties of Steel (Ince, Yalcin and Arslan 2007).

Diameter D_s (mm)	Young Modulus E_s (GPa)	Poisson Ratio ν_s	Yielding Strength f_y(MPa)
12	200	0.3	476

3.1. Mesh Size Effect

As it is mentioned before, a very restricted area of the reinforced concrete structure is subjected to dowel action (Walraven and Reinhardt 1981). Therefore, the mesh properties for the numerical illustrations should be determined very carefully to represent dowel action correctly in this restricted area. Before going into a deeper investigation, mesh size effect is investigated in order to see the mesh dependency of the numerical calculation. That way, a proper mesh can be determined for the realistic presentation of the chosen geometry (L-beams). Besides, 1D beam element representation for the steel is compared with 3D representation for different mesh sizes to evaluate the reinforcement model.

The defined boundary conditions and the reinforcement layout of L-beams are shown in Figure 4.7a and 4.7b. A 5 mm displacement (U_z) is imposed on the upper surface of the L-beam, at

the same time as the displacement on other directions (U_y and U_y) is blocked to avoid the separation of the concrete blocks. The bottom surface is blocked against any displacement (U_x, U_y, U_z). Moreover, the rotation of the dowel bars on the x-axis (R_x) are blocked for the beam element steel representation. The dowel bars (DW1 and DW2) are represented by 1D beam or 3D elements, reinforcement (V_R) is represented by 1D truss elements, concrete (V_c) is represented by 3D solid elements (Figure 4.7b). The Perfect bond hypothesis is used for the interface. Both steel and concrete are assumed as totally elastic materials in order to avoid any other complex parameters which could affect the numerical results, whereas we want to focus only on the influence of mesh density.

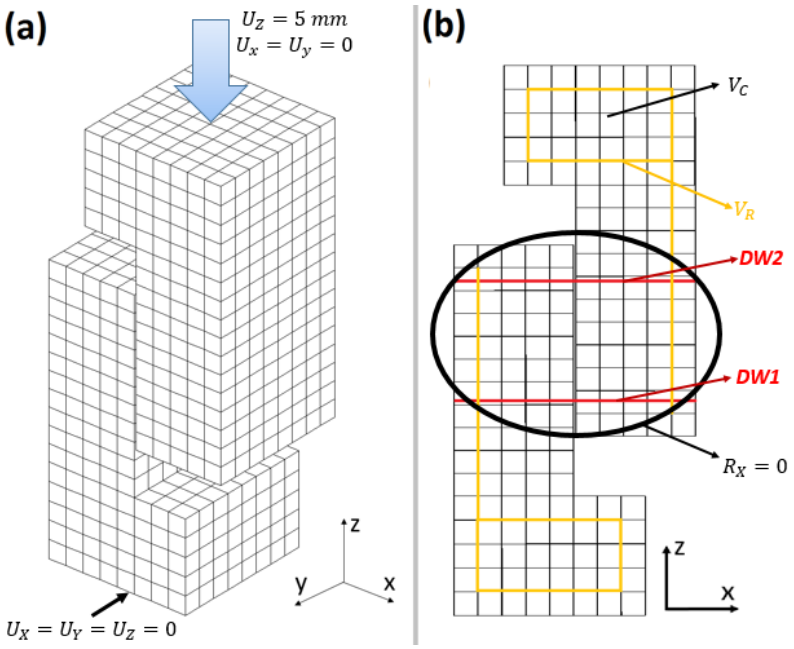

Figure 4.7 (a) Boundary conditions of the simulation. (b) Location of steel bars.

From the experimental push-off campaign of (Ince, Yalcin and Arslan 2007), only 90° dowel bar angle with the vertical direction is chosen for the size effect simulations. In order to compare 1D (beam) and 3D steel representations, three different mesh densities are chosen for steel and concrete. These three mesh densities are categorized as coarse, medium and fine meshes. The mesh properties of the 1D steel simulations can be found in Table 4.5 and mesh geometries are presented in Figure 4.8.

Table 4.5 Mesh properties of 1D steel simulations.

Mesh Name:	*Coarse*	*Medium*	*Fine*
Mesh Density:	0.06	0.04	0.02
Number of concrete elements:	84	240	1520
Number of reinforcement elements:	52	80	164
Number of dowel bar elements:	10	14	22

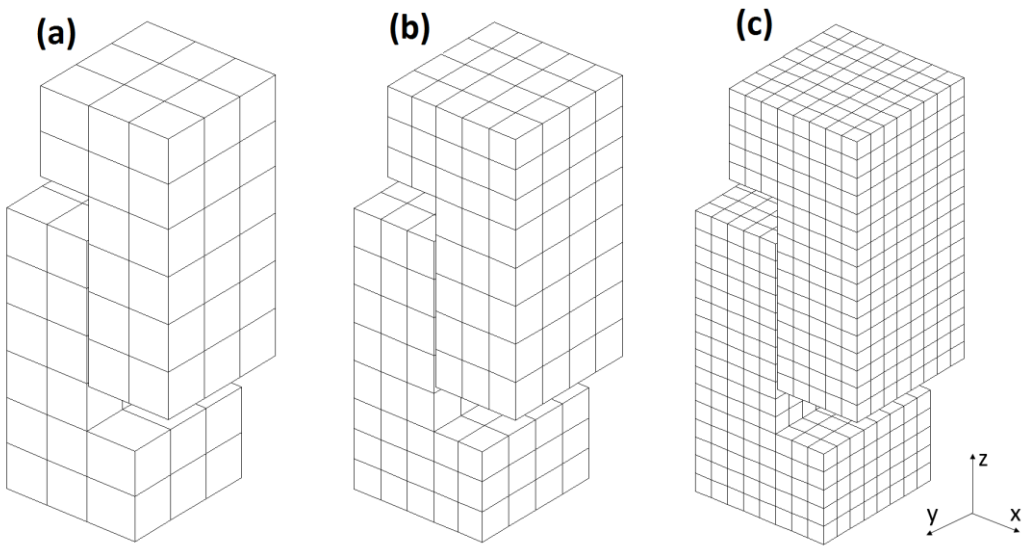

Figure 4.8 Mesh sizes: (a) coarse mesh, (b) medium mesh, (c) fine mesh for 1D steel representation (Case 1 and 2).

For the 1D steel simulations, two different cases are investigated. In case 1, the same mesh densities are defined for both steel and concrete representation. In case 2, a steel node is added between two concrete blocks in order to investigate the behavior of the cracked area. The representation of case 2 can be seen in Figure 4.9. Both cases (case 1 and 2) are simulated with coarse, medium and fine meshes.

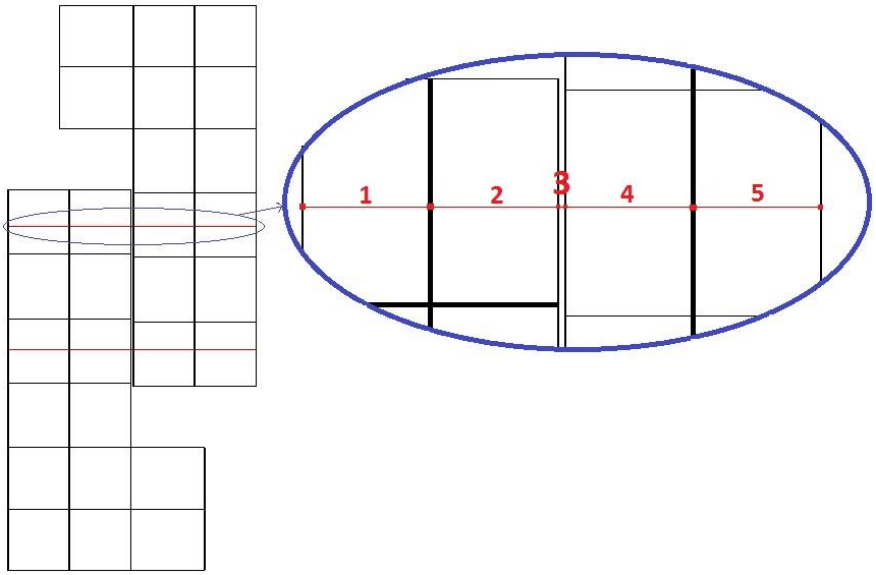

Figure 4.9 Representation of the external node between the concrete blocks (Case 2).

Case 3 represents the 3D steel simulations with different mesh sizes (coarse, medium and fine). The mesh properties of the 3D steel simulations can be found in Table 4.6 and mesh geometries are presented in Figure 4.10.

Table 4.6 Mesh properties of 3D steel simulations.

Mesh Name:	***Coarse***	***Medium***	***Fine***
Mesh Density:	0.06	0.04	0.02
Number of concrete elements:	1608	2484	4320
Number of reinforcement elements:	52	80	164
Number of dowel bar elements:	1080	1512	2376

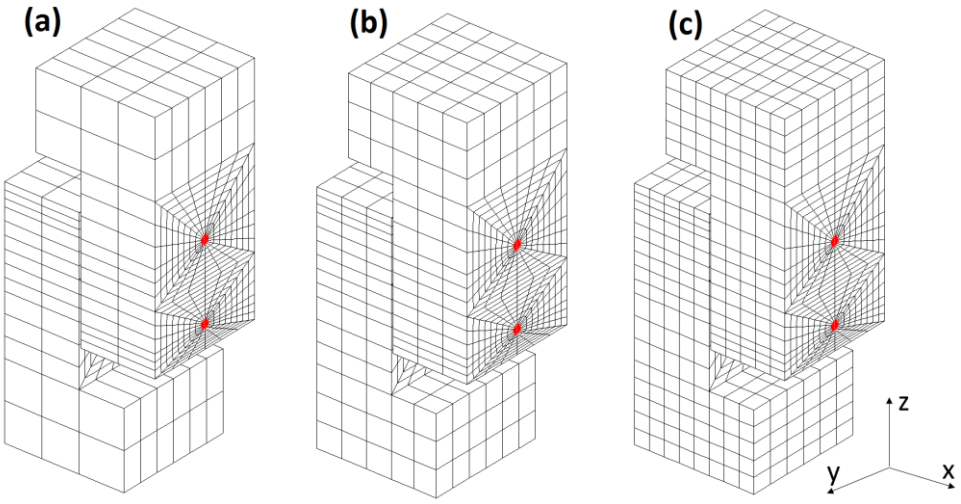

Figure 4.10 Meshes for 3D steel representation (case 3): (a) coarse, (b) medium, (c) fine.

Force values after loading for different mesh densities are given in Table 4.7.

Table 4.7 Force values of all mesh sizes of L beams.

	Displacement (mm)	$Force_{coarse}$ **(kN)**	$Force_{medium}$ **(kN)**	$Force_{fine}$ **(kN)**
Case 1 :	5	145.5	588.2	806.6
Case 2 :	5	937.7	718.5	806.6
Case 3 :	5	1016	916.7	897.3

According to the numerical analysis with different mesh densities, the results of the 3D steel model which are quite stable for different mesh densities are chosen as the reference case. On the other hand, a huge variability is observed for the beam element simulations in both cases 1 and 2. It has been found that the numerical presentation of dowel action is excessively sensitive to the mesh definition of the geometry. Since the dowel action occurs in a very restricted space, the mesh properties of steel and concrete cover around the crack affect the numerical calculations. As the crack supposed to be small, the mesh density should be chosen also as fine, in order to avoid a huge error margin in the analyze of dowel action in numerical applications. More importantly, defining an exclusive node between the crack surfaces (case 2) provides an accurate analysis of the behavior in the pre-cracked section and decreases the mesh dependency.

Even in elasticity, the results are very sensitive to the mesh size and it seems the convergence is not reached. Nevertheless, for the fine mesh, the three cases give results closer to each other. Moreover, adding a beam node in the cracked zone, outside the concrete (case 2) seems to better capture the double bending of the steel bar. This node is added for all the L-beam simulations in the following simulations.

3.2. Numerical analysis of Dowel Action on L-Beams

The experimental test of (Ince, Yalcin and Arslan 2007) which was explained in detail previously, is modeled for different reinforcement bar inclination angles (45° and 90°, counted from the vertical) in order to observe the pure dowel action in numerical applications. Based on the previous test study, fine mesh density (Figure 4.8c) is used with an external steel node between concrete blocks. The same boundary conditions are applied as in Figure 4.7 for all simulations. The material properties of steel and concrete are taken as in Table 4.3 and 4.4. The

concrete is taken as 3D solid elements with Mazars damage criteria (Mazars 1986) for all the simulations. Elastoplastic behavior is assumed for the reinforcement and dowel bars. 1D truss and beam element steel representations are compared to understand the significance of the reinforcement model to observe dowel action numerically. Moreover, for the steel-concrete interface, perfect bond hypothesis and new bond-slip model are used separately to evaluate the model's efficiency under shear loading. The numerical results are compared with the experimental ones in order to understand suitable models for the steel and bond. Simulation properties are given in Table 4.8 and the mesh geometries of 45° and 90° dowel bar angels are presented in Figure 4.11.

Table 4.8 Simulation properties for push-off tests.

Simulation Name	**Bar inclination Angle $\boldsymbol{\theta}$(°)**	***Concrete Model***	**Steel Model**	**Interface Model**
45-Truss-Perfect	45	3D Solid Elements	1D Truss Elements	Perfect Bond Assumption
45-Truss-Bond	45	3D Solid Elements	1D Truss Elements	Bond-slip Model
45-Beam-Perfect	45	3D Solid Elements	1D Beam Elements	Perfect Bond Assumption
45-Beam-Bond	45	3D Solid Elements	1D Beam Elements	Bond-slip Model
90-Truss-Perfect	90	3D Solid Elements	1D Truss Elements	Perfect Bond Assumption
90-Truss-Bond	90	3D Solid Elements	1D Truss Elements	Bond-slip Model
90-Beam-Perfect	90	3D Solid Elements	1D Beam Elements	Perfect Bond Assumption
90-Beam-Bond	90	3D Solid Elements	1D Beam Elements	Bond-slip Model

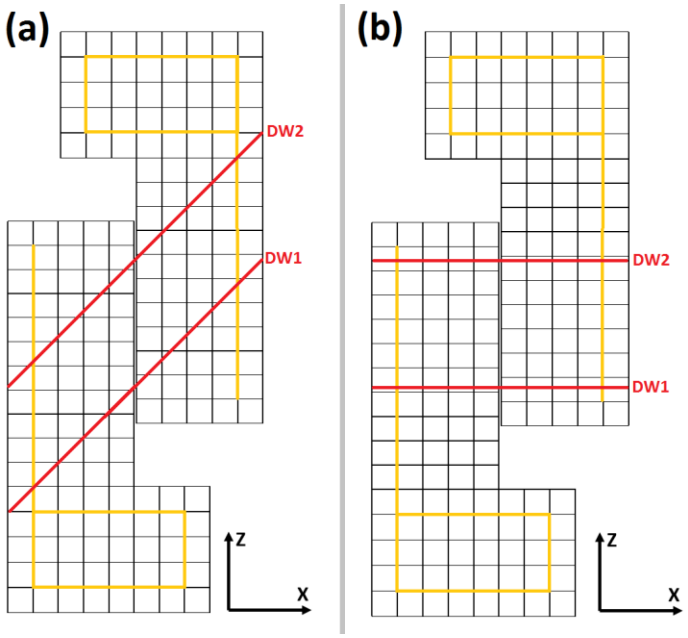

Figure 4.11 Mesh geometries and reinforcement layout of (a) 45° and (b) 90° dowel bars.

Effect of Reinforcement Model

The first analysis is performed on the reinforcement model. There is no convergence for the truss element reinforcement simulation with 90° bar inclination angle because of the one-directional behavior of steel. The applied load is perpendicular to the reinforcement, and it is impossible to withstand the transverse force with truss elements.

With truss elements for steel reinforcement, the dowel action is observed only for 45° inclination angle simulations, where a part of the axial force in the reinforcement acts in the direction of the applied load (Z direction in Figure 4.11a). However, a part of the applied load is transversal to the reinforcement and is not being countered by truss elements. This is why the ultimate forces obtained in 45-Truss-Perfect and 45-Truss-Bond simulations are very small compared to experimental results (Table 4.9 and Figure 4.12).

Table 4.9 Comparison of the results for 45° dowel bars.

Simulation Name	$\boldsymbol{Inclination\ Angle\ \theta(°)}$	$\boldsymbol{Ultimate\ Force\ V_U\ (kN)}$
45-Truss-Perfect	45	9.52
45-Beam-Perfect	45	40.86
45-Truss-Bond	45	9.54
45-Beam-Bond	45	47.62
Experimental 45°	45	1) 45.70 2) 40.60 3) 43.10

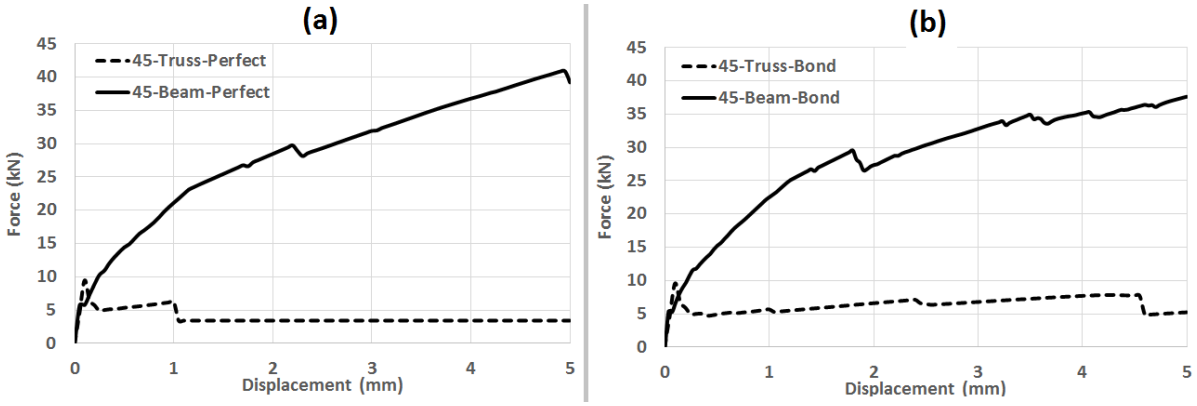

Figure 4.12 Force vs displacement curves of 45° beam and truss element representations with (a) perfect bond model, (b) bond-slip model.

On the contrary, using beam elements for the dowel steel lead to ultimate forces near the experimental ones (Table 4.9 and Figure 4.12). In the particular configuration of the L-Beam push-off test, the bending of the steel bar in the gap between the concrete blocks plays a primordial role. The reason is that this gap is relatively wide (2 mm) compared to a classical crack opening (less than 0.5 mm).

Effect of Inclination Angle

From the results of the previous section, only the beam element steel model results are presented here for different dowel bar angles. Comparison of the numerical results with the experimental ones for 45° and 90° dowel bar angles can be found in Table 4.10 and the force-displacement curves are presented in Figure 4.13.

Table 4.10 Comparison of results of 45° and 90° dowel bar angles for push-off tests.

Simulation Name	$\boldsymbol{Inclination\ Angle\ \theta(°)}$	$\boldsymbol{Ultimate\ Force\ V_u\ (kN)}$
45-Beam-Perfect	45	40.86
45-Beam-Bond	45	37.62
Experimental 45°	45	1) 45.70 2) 40.60 3) 43.10
90-Beam-Perfect	90	44.69
90-Beam-Bond	90	43.97
Experimental 90°	90	1) 35.80 2) 47.60 3) 43.80

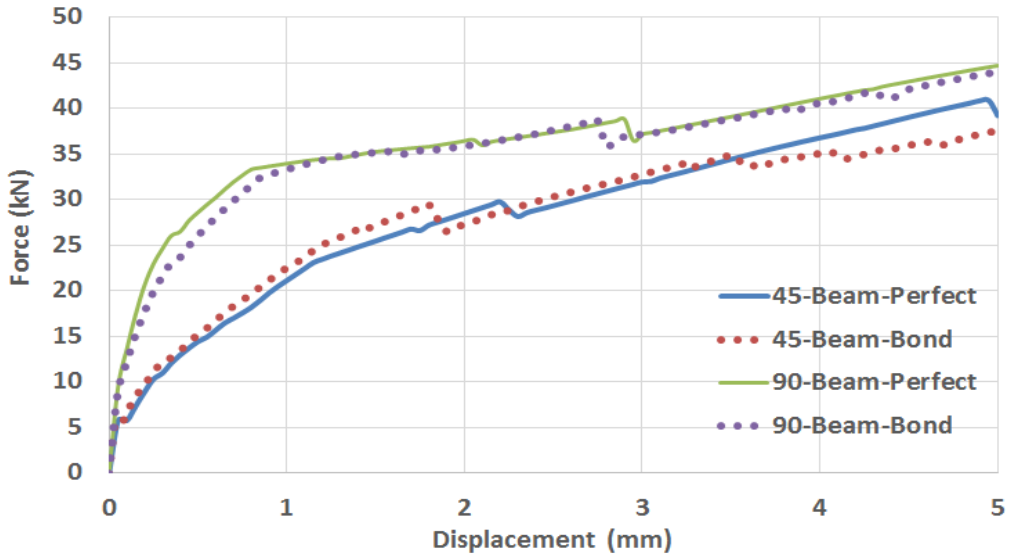

Figure 4.13 Force vs displacement curves of L-beams for different angles with bond-slip and perfect bond models.

The numerical results of L-beams with different inclination angles (90°and 45°) with beam element steel models show that the beam element representation of reinforcement is convenient to present the pure dowel action. The general force values of both bond models are in coherence with the experimental campaign (Table 4.10). However, there is some dispersion on the experimental results.

The bond slip effect is small, probably because of the damage of the concrete around the steel bars (Figure 4.14). Nevertheless, this little effect seems to be greater for the 45-Beam-Bond simulation ($\frac{40.86-37.62}{40.86} \rightarrow 7.9\%$) compared to the 90-Beam-Bond simulation ($\frac{44.69-43.97}{44.69} \rightarrow$ 1.6%). Indeed, the slip along the 45° inclined bars is greater than along the 90° bars (Figure 4.15). This is due to the fact that the applied force has a part acting tangentially to the reinforcement bars in the case of 45° angle, and it activates more the interface element. Nevertheless, there is also a slip in the 90° angle case (Figure 4.15), which shows that even perpendicular to the applied load, the reinforcement bar acts not only in bending but also in tension.

The simulations with different dowel angles show that the ultimate force is decreasing with a decreasing inclination angle. The more the dowel perpendicular to the crack, the more efficient dowel action.

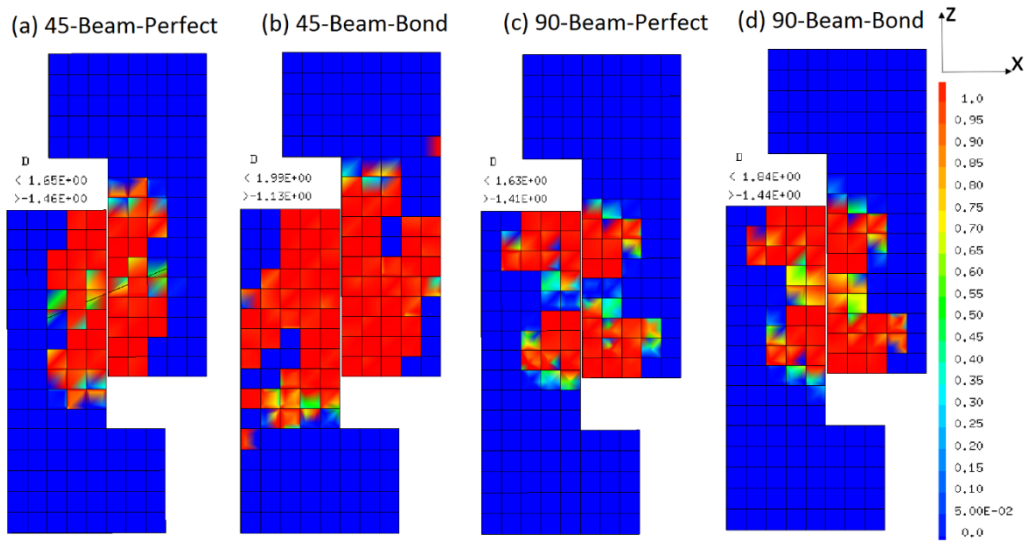

Figure 4.14 Cross-sections of final damage patterns: (a) perfect bond model with 45° elongation angle, (b) perfect bond model with 90° elongation angle, (c) bond-slip model with 45° elongation angle, (d) bond-slip with 90° elongation angle simulations.

As presented in Figure 4.14, the concrete damage is observed around the dowel bars close to the pre-cracked location. Depending on the dowel bar angle, the distribution of damage in the concrete blocks is different. Thus, more damage is observed for the 45° simulations. The reason is that in the 45° case, the steel bars act not only in dowel near the crack but also as classical reinforcement in reinforced concrete since a part of the applied force is transferred along the axis of the bars. Furthermore, more damage is observed for the bond-slip model simulations than the perfect bond simulations in the case of 45° inclination angles. The reason is the same as before, there is a redistribution of forces along the steel which takes a part of the applied force.

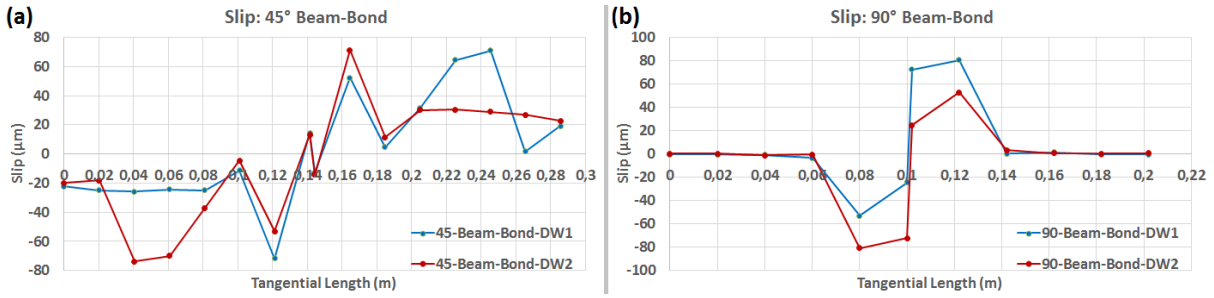

Figure 4.15 Final slip along the dowel bars for: (a) dowel bars with 45° angle, (b) dowel bars with 90° angle.

According to Figure 4.15, it can be seen that slip is more distributed along dowel bars (DW1 and DW2) in 45° simulations than the 90° simulations. This is coherent with the previous explanations above. Moreover, for both cases (45° and 90°), the slip of the bottom (DW1) and

top (DW2) dowel bars are not identical. It is quite logical to obtain more slip closer to the loading and supporting points.

As a sum up, according to the obtained results on the L-beam push-off simulations, the following conclusion may be drawn:

- Extreme mesh dependency is observed in the simulations. To capture the dowel action, steel mesh should be chosen properly near the crack location.
- The reinforcement model is extremely important to represent the dowel action when the crack is widely open. The chosen model has to consider the bending behavior of the steel bar at the crack locations. In this regard, 1D truss element steel fails to represent pure dowel action.
- In order to represent dowel action, steel representation is more important than the interface and concrete models. To obtain the realistic results, the considered reinforcement model should be chosen very carefully to capture the bending of the steel bar.
- Even though the bond-slip model represents the cracking properties better than the perfect bond assumption, it gives similar global results for the push-off tests.
- Dowel action does exist and can be represented numerically if the proper models are used and proper meshing is made.

4. Bending Test on a Continuous Deep Beam

In order to have a deeper understanding of the validity of the new bond-slip model, dowel action applications at the structural scale are investigated in this section.

As mentioned in Chapter 1, continuous deep beams are generally used to investigate the shear behavior of reinforced concrete structures in the literature ((Ashour 1997), (Yao and Teng 2007), (Adhikary, Li and Fujikake 2013) etc.). Experimental four-point bending test on continuous deep beams (Zhang and Tan 2007) is chosen for this specific study after a sufficient literature research to see the role of dowel action in the shear transfer and compare the effect of dowel action with the other transfer components.

In numerical analysis, it is quite common to use truss element representation of steel for the industrial application. Therefore, truss and beam element approaches are compared once again

to understand the difference between them on a relatively larger structure. Moreover, the perfect bond hypothesis is again compared with the bond-slip model and the experimental results to find out a proper representation of shear behavior numerically. Continuous deep beams with horizontal reinforcement (without web reinforcement) are studied in order to focus mainly on dowel action. The chosen beam geometries for the numerical analysis are presented in detail in the next section.

Experimental Test Setup

Four-point bending tests on a continuous deep beam from the experimental study of (Zhang and Tan 2007) are chosen for the reference geometry. A deep beam with horizontal reinforcement is analyzed to observe the dowel action. Experimental test setup (Figure 4.16), reinforcement layout (Figure 4.17), specimen details (Table 4.11), material properties (Table 4.12 and 4.13), experimental results (Table 4.14) and crack distribution after loading (Figure 4.18) are respectively presented as following.

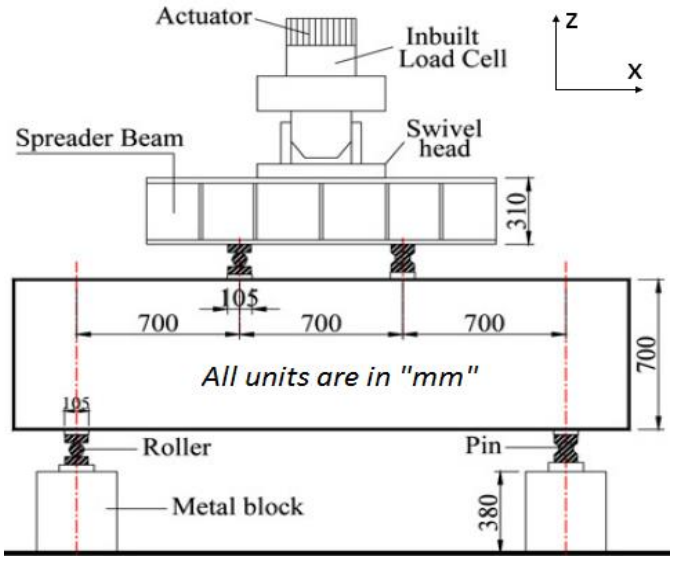

Figure 4.16 Experimental test setup of continuous deep beam (Zhang and Tan 2007).

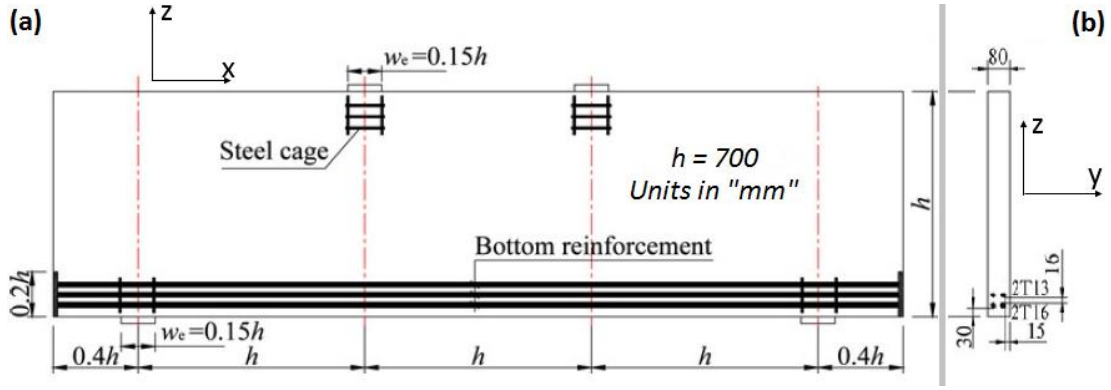

Figure 4.17: (a) Reinforcement layout of the specimen. (b) Cross section of the beam (Zhang and Tan 2007).

Table 4.11 Details of the specimen (Zhang and Tan 2007).

Beam Width B (mm)	**Overall Height H (mm)**	**Effective Depth D (mm)**	**Reinforcement Ratio ρ_s(%)**
80	700	650	1.28
Width of Loading & Support Plate W (mm)		**Bottom Reinforcement A_s (mm)**	
105		668	

Table 4.12 Concrete Properties (Zhang and Tan 2007).

Young Modulus E_c (GPa)	**Poisson Ratio ν_c**	**Compressive Strength F_c (MPa)**	**Tensile Strength F_t (MPa)**
23.4	0.2	24.8	2.55

Table 4.13 Steel Properties (Zhang and Tan 2007).

Types of Reinforcement	**Diameter d_s (mm)**	**Young Modulus E_s (GPa)**	**Poisson Ratio ν_s**	**Yielding Strength f_y(MPa)**	**Ultimate Strength f_u(MPa)**
T8	8	210	0.3	500	500
T13	13	190	0.3	520	611
T16	16	194	0.3	499	648

Table 4.14 Experimental Results (Zhang and Tan 2007).

Failure Load V_n (kN)	**Initial Cracking Load V_{cr} (kN)**	**Initial Diagonal Cracking Load V_d (kN)**	**Serviceability Load V_{ser} (kN)**	**Failure Mode**
311	70	160	160	Shear Compression

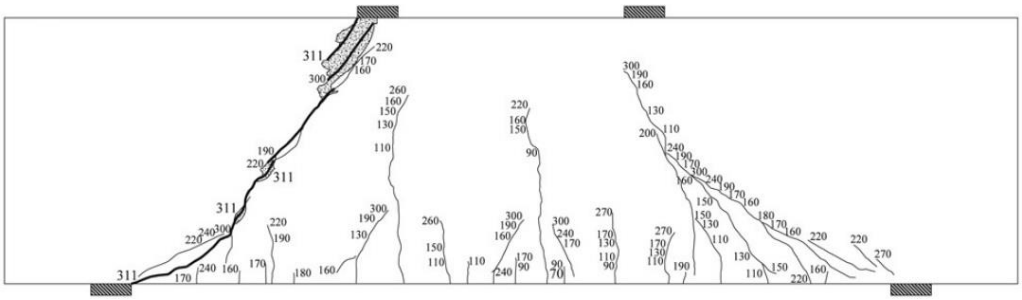

Figure 4.18: Crack Pattern of the specimen at the end of the loading (Zhang and Tan 2007).

Simulation Properties

Different models are used for the numerical analysis in order to analyze the proper representation of the structural behavior under shear loading. Due to the symmetry in the four-point bending test, the simulation is made for the ¼ geometry of the whole specimen. The series of simulations are focused on the reinforcement model and also the steel-concrete interface representation. The horizontal steel bars are modeled with elastoplastic 1D beam or truss element models. The new bond-slip model or perfect bond assumption of the steel-concrete interface are used in the simulations. 3D solid elements are used for concrete. The behavior of the concrete is represented by non-local Mazars damage model (Giry, Dufour and Mazars 2011). Steel and concrete properties are represented in Tables 4.12 and 4.13. Thus, the mesh geometry and boundary conditions are presented in Figure 4.19. The simulation properties are presented in Table 4.15.

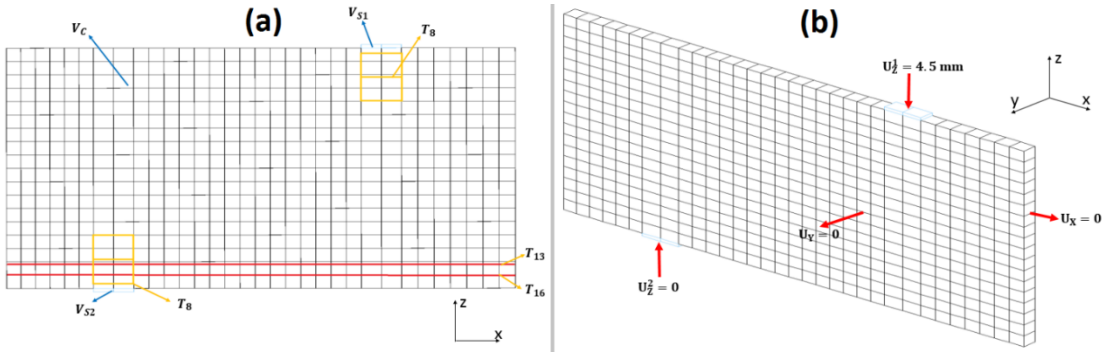

Figure 4.19 (a) Mesh geometry, (b) boundary conditions of the continuous deep beam.

Table 4.15 Simulation Properties

Simulation Name:	Truss-Perfect	Truss-Bond	Beam-Perfect	Beam-Bond
Concrete:	3D Solid Elements	3D Solid Elements	3D Solid Elements	3D Solid Elements
Reinforcement:	1D Truss Elements	1D Truss Elements	1D Beam Elements	1D Beam Elements
Steel-Concrete Interface:	Perfect Bond Assumption	Perfect Bond Assumption	Bond-Slip Model	Bond-Slip Model

Numerical Results

Figure 4.20 shows the force-displacement curves comparison between experimental and numerical results for the four different simulations. In order to show the effect of shear cracks in the numerical simulations, Figures 4.21 and 4.22 give the damage shapes at the maximum applied forces along with the experimental cracked pattern. Figure 4.23 shows the tangential slip between steel and concrete along the interface elements of the reinforcement for "Truss-Bond" and "Beam-Bond" simulations. It should be remarked that there is no slip between steel and concrete in case of the perfect bond ("Truss-Perfect" and "Beam-Perfect" simulations) since the same displacement is assumed in reinforcement and concrete. Finally, the magnified deformed shapes at the end of the four simulations are presented in Figure 4.25 to analyze the mechanisms that lead to the ruin and/or the end of convergence in the simulations.

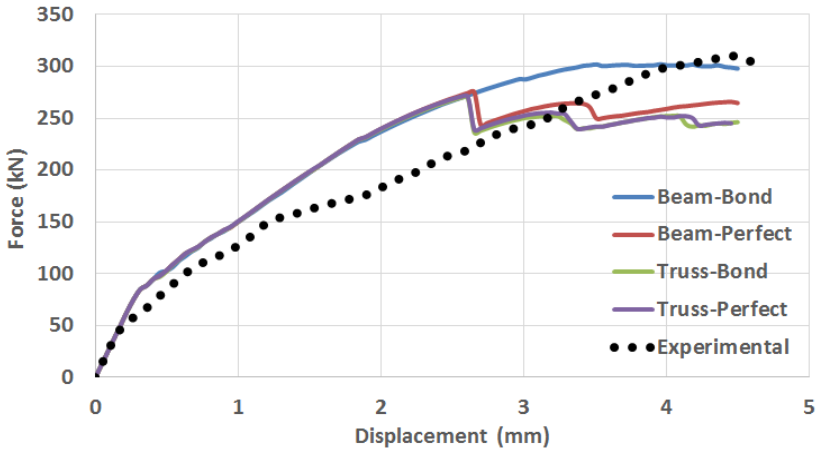

Figure 4.20 Force-displacement curves of numerical and experimental results.

Concerning the global behavior, it can be seen in Figure 4.20 that the simulation curves are close to the experimental one. But for three simulations ("Truss-Perfect", "Truss-Bond" and "Beam-Perfect") there is a force drop along with an apparition of a shear crack between the support and the loading point (Figures 4.20). The drop is about at the same level for "Truss-Perfect" and "Truss-Bond" simulations. For the "Beam-Perfect" simulation, the simulation goes a little further because of the bending stiffness of beam elements which delays the damage evolution in the concrete under shear. But there is still a premature shear crack in the simulation with the perfect bond assumption. On the contrary, the combination of the bond-slip model for the steel-concrete interface and beam element approach for the reinforcement model ("Beam-bond" simulation) can go further in the force-displacement graph compared to the other simulations and gives yet coherent results with the experimental ones. The use of the new bond-slip model with 1D beam elements is suitable for these kinds of numerical applications.

Table 4.16 Comparison of the results

Test Name	Initial Cracking Load V_{cr} (kN)	Failure Load V_n (kN)	Failure Mode
Truss-Perfect	75.88	270.63	Shear
Truss-Bond	75.84	269.61	Shear
Beam-Perfect	75.89	275.15	Shear
Beam-Bond	75.90	302.17	Shear
Experimental	70	311	Shear

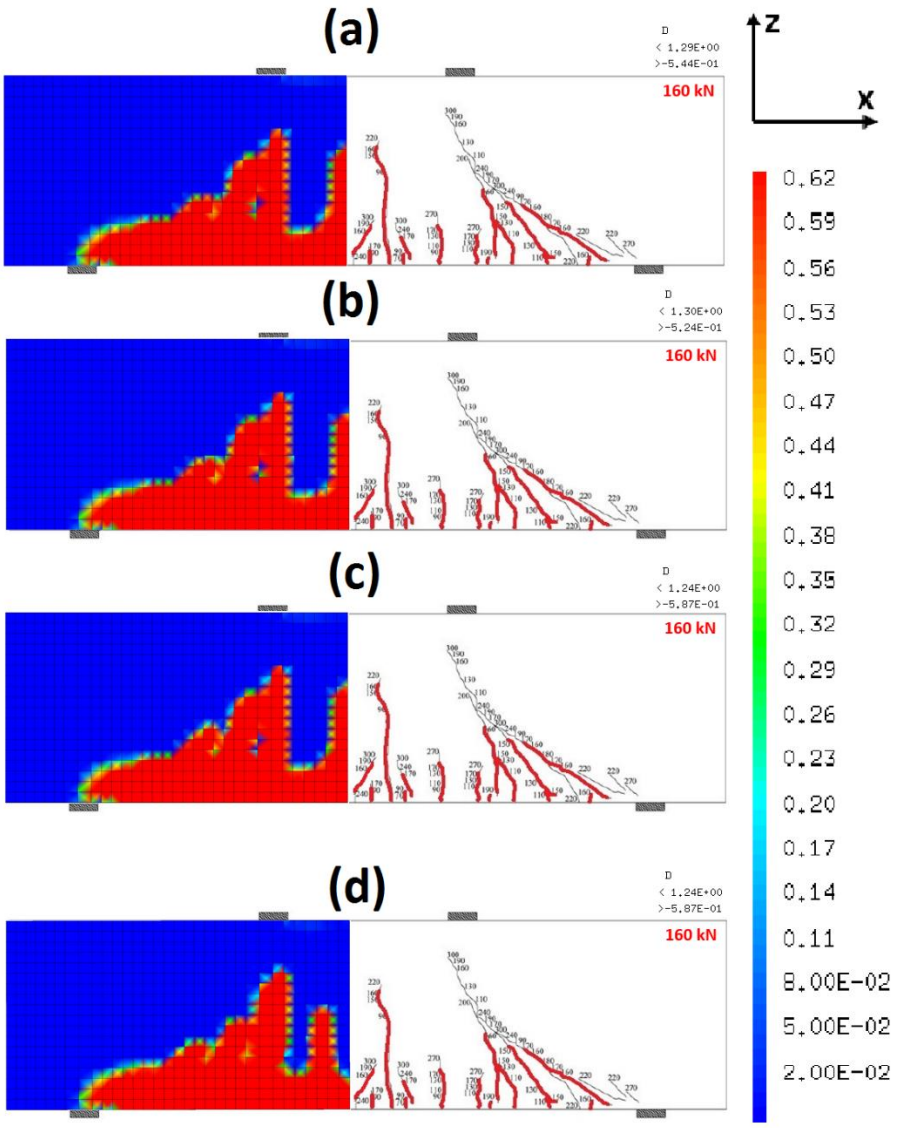

Figure 4.21 Damage patterns under 160 kN load of (a) truss-perfect, (b) truss-bond, (c) beam-perfect, (d) beam-bond simulations compared to experimental crack pattern.

According to Figure 4.21, the crack patterns of all 4 simulations give similar results to the experimental ones. The crack is initialized from the mid-span of the continuous deep beam and propagates through the upper support. Under the load 160 kN, no significant difference is observed between the different steel and bond models.

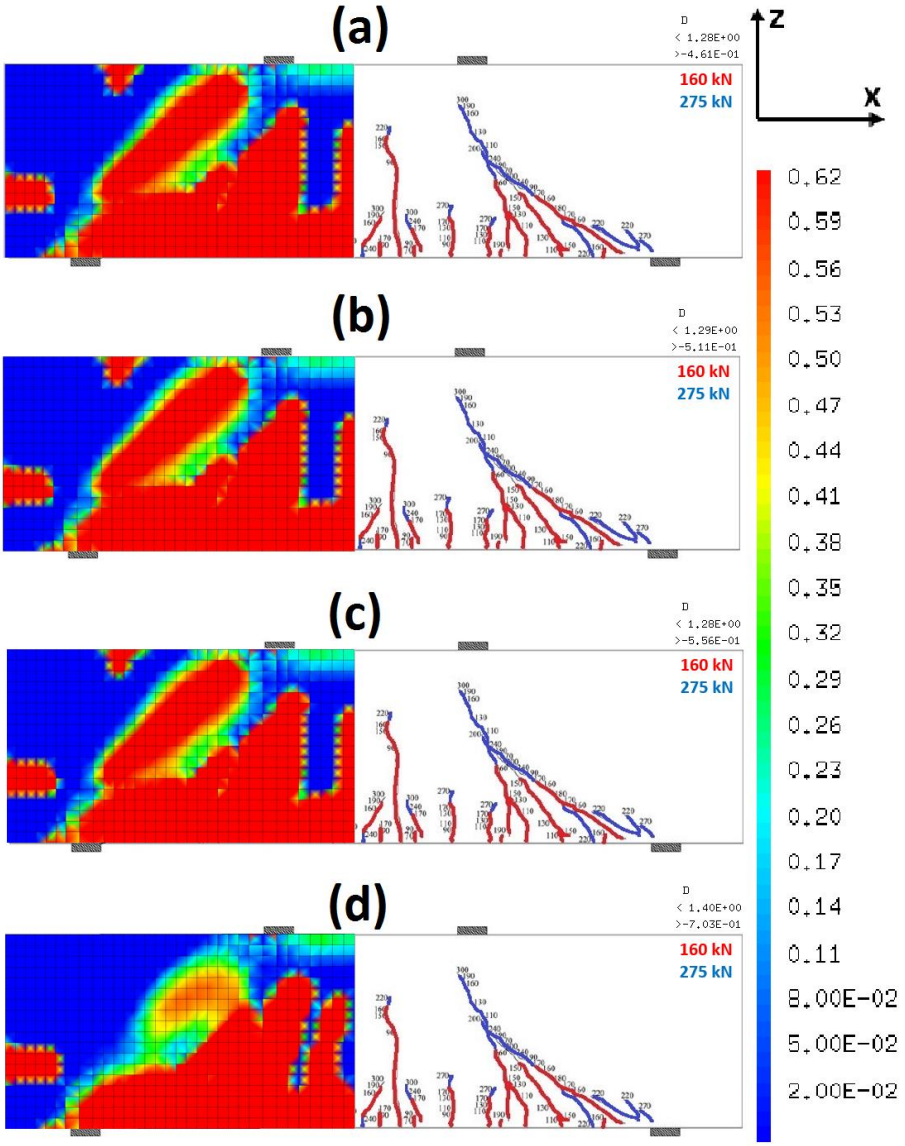

Figure 4.22 Damage patterns under 275 kN load of (a) Truss-Perfect, (b) Truss-Bond, (c) Beam-Perfect, (d) Beam-Bond simulations compared to experimental crack pattern.

The quick growth of damage can be seen between Figures 4.21 and 4.22. When Figure 4.22 is considered, a shear crack can be observed for all three simulations of "Truss-Perfect" (Figure 4.22a), "Truss-Bond" (Figure 4.22b) and "Beam-Perfect" (Figure 4.22c) under 275 kN loading. On the other hand, the shear crack is not observed for the "Beam-Bond" simulation (Figure 4.22d) where the slip is considered. This later one causes a relaxation of stresses on the concrete structure and delays the shear crack occurrence between the supports. A shear crack occurs in "Beam-Bond" simulation afterward (under 305 kN of loading) which is yet agreeable with the experimental failure load (V_n) of 311 kN (Table 4.16). The combination of beam element steel representation and bond-slip model steel-concrete interface representation gives coherent results not only globally (force-displacement curve) but also locally (crack pattern).

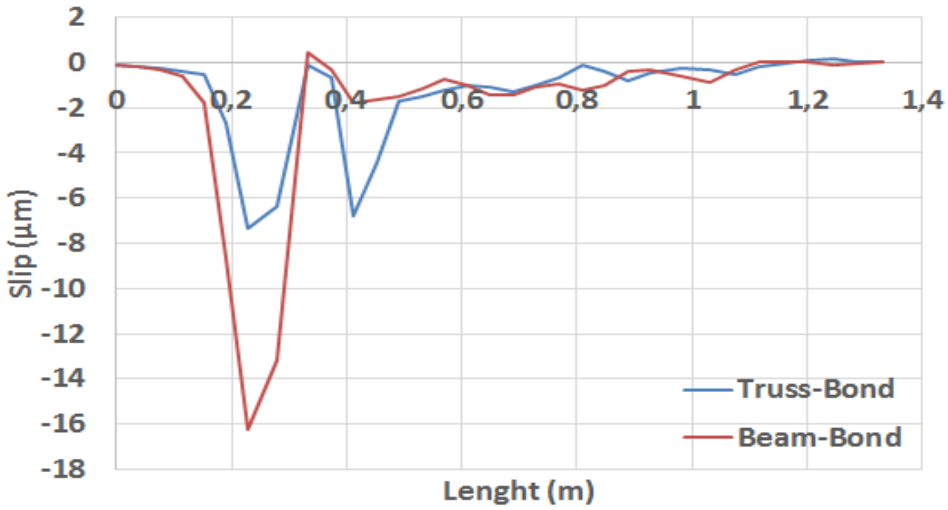

Figure 4.23 Final slip between steel and concrete along the bottom horizontal steel bars.

It can be seen from Figure 4.23 that the maximum slip is always observed near the bottom support. This slip is due to the stress concentration and the starting of shear crack. According to the input adhesion law, sliding and nonlinear behavior is observed for the interface at the support location. Due to the slip, less bond stress is observed in the bond-slip model simulations than the perfect bond hypothesis. This means less stress is transferred from the interface to the concrete cover around the support compared to the perfect bond. This may cause the early shear crack occurrence in the perfect bond simulations.

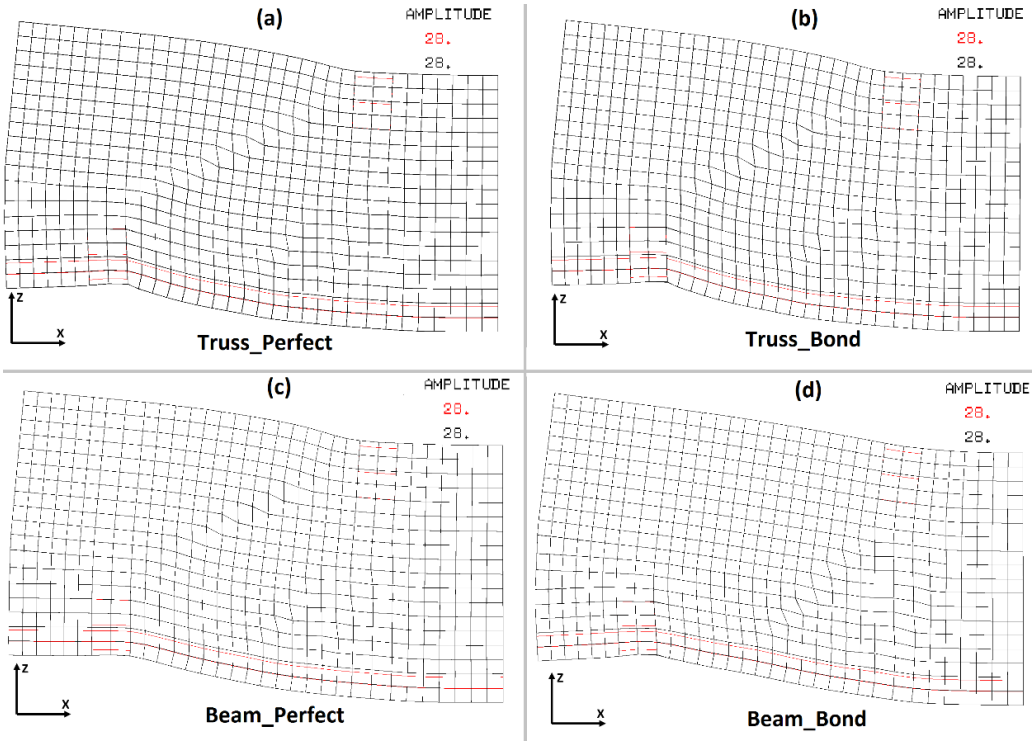

Figure 4.24 Deformed shapes at the end of simulation of (a) beam-bond, (b) beam-perfect, (c) truss-bond and (d) truss-perfect simulations.

There is a close interaction between damage in concrete and bond slip behavior. Indeed, it is observed that the simulation “Beam-Bond” go further before shear crack appearing. The sliding introduces some relaxations and the stress distributions are different, especially near the support where the shear crack starts. All these observations reveal the extreme dependence of the behavior on boundary conditions in such simulations. Mesh density, concrete damage model, symmetry properties, the location of the applied force, blockage methodology of the bottom support, material properties and the exact location of the cage reinforcement around the supports may cause the stress concentration on the supports and lead to a sudden failure of the support in such finite element analyses.

As a sum up, a four-point bending deep beam is modeled with truss element or beam element approaches using bond-slip or perfect bond interface models. Results revealed that the truss element representation of the reinforcement is not totally sufficient to reflect the global behavior after the shear crack occurrence due to its lack of ability to consider transverse behavior response of the steel when a shear load is applied. The stress drop is quite smaller in beam element representation of the steel bars with the perfect bond model compared to the truss element approach. However, the general behavior does not totally represent the reality in “Truss-Perfect”, “Truss-Bond” and “Beam-Perfect” simulations when they are compared with the experimental results. Since the bond-slip model is considering different displacements on both steel and concrete materials, it better represents the shear transfer mechanism after the shear crack occurrence.

5. Conclusion

In this chapter, the shear behavior of the reinforced concrete structures is investigated by focusing on dowel action. The finite element analyses are performed with the proposed bond-slip model for the steel-concrete interface and compared with the experimental values. 1D reinforcement models (truss and beam) are also examined within the scope of this study. The numerical analyses are performed on L-beams and continuous deep beams to investigate dowel action and the total shear behavior of the reinforced concrete structures. The following conclusions may be drawn.

Firstly, calibration of the reinforcement model is made before investigating the dowel action on relatively larger structures. The processes showed that the beam element modeling of steel

bars gives coherent results compared to a multi-fiber approach if the proper distances are defined for the plasticity computation according to the diameter of the bar.

Mesh density is affecting the accuracy of the numerical results for the dowel action analysis. Since dowel action occurs in a very limited space compared, a smaller mesh density better represents this mechanical behavior. Defining explicit nodes for steel between the two sides of the crack may represent the mechanical behavior of the cracked area in a more appropriate way. The mesh density has thus a vital importance.

The numerical analysis which are performed on L-beams reveal that the dowel action does exist and could be observed in numerical simulations in case of significant crack openings by only using a correct existing methodology. On one hand, the truss element approach on reinforcement is not adequate to represent mechanical behavior of reinforced concrete structures under shear loading after the occurrence of dowel action. On the other hand, the beam element approach on the reinforcement gives convenient results compared to the experimental ones.

The numerical analysis which is performed on continuous deep beams (structural scale) reveals that truss and beam element methods are working well until the dowel action is taken part. All the deep beam simulations have coherent results with the experiment in the first few millimeters of displacement. It is possible to go further in the iteration of the numerical analysis by using the beam element approach. The reason may be the dowel action. Truss element cannot represent the mechanical behavior of reinforced concrete under shear loading correctly after the crack opened a certain amount (where dowel action occurs).

Finally, the bond-slip model represents the global (force-displacement relation) and the local behavior (crack pattern) of the reinforced concrete structures under shear loading better than the perfect bond assumption model.

General Conclusion and Perspectives

A bond-slip model was initially proposed by (Casanova, Jason and Davenne 2012) to represent the effects of steel-concrete bond behavior in reinforced concrete structures associated to a Finite Element Model (Cast3M 2017). Subsequently, this method was particularly adapted to the simulation of 'small' structures like a single wall by (Mang, Jason and Davenne 2015). The aim of this study was to improve the initial bond-slip model to be more efficient and more representative. The adapted methodology can be summarized as in the Figure I.

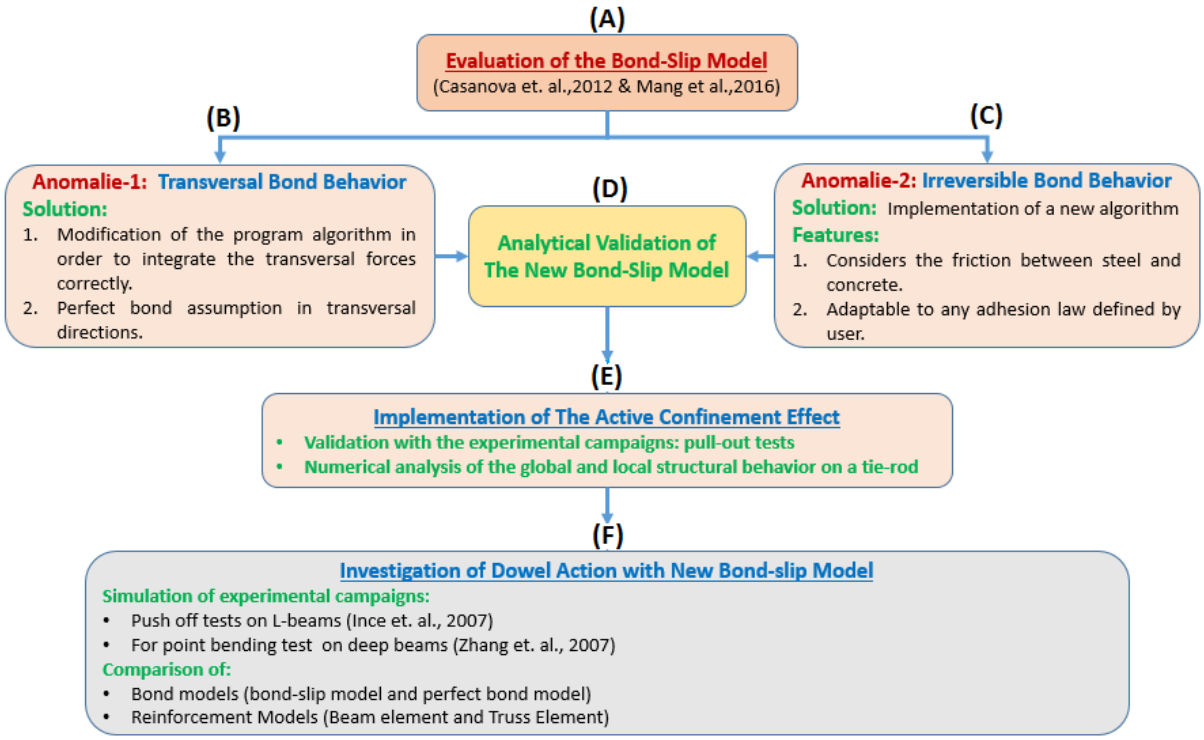

Figure I Adapted methodology during the study.

The first step was to evaluate the initial bond-slip model (Figure I.A). After the evaluation, two major anomalies are found within the model:

- Miscalculation of the transverse forces on the interface element,
- Insufficient representation of the irreversible bond behavior.

Firstly, transversal behavior of the bond-slip model is studied by performing several simulations. Simple geometries like a single interface element are chosen for the simulations in order to focus only on the bond behavior. The simulation results revealed that the forces are calculated incorrectly in normal directions of the interface element. This abnormality is

regulated by implementing the proper calculation methodology to the source code. This methodology enables the use of the bond-slip model in numerical applications (Figure I.B).

Secondly, the irreversible behavior of the steel-concrete bond is studied. After a series of simulations on a single interface element, it has been denoted that the existing cyclic model does not satisfy the real behavior of the bond under alternating loads when different adhesion laws are defined by the user for steel-concrete interface. Admittedly, the friction between steel and concrete elements is not considered in calculations of the existing model. Afterwards, a completely new irreversible bond model is introduced in order to represent the bond behavior properly. This new irreversible model considers the friction between the steel and concrete. It is also adaptable to different adhesion laws which can be defined by the user. The new model is tested on an interface element for different friction stresses, alternative loads and adhesion laws (Figure I.C).

After the modifications in the bond-slip model related with transversal and cyclic bond behaviors, an analytical validation has been performed on the tangential behavior. For the validation, the analytical solution proposed by (Casanova, Jason and Davenne 2012) and (Mang 2016) are compared with the numerical solution for a tie-rod test. The numerical results are found to be coherent to analytical ones. Thus, several rigidity values are tested for the interface on the same tie-rod test case in order to find out the optimal values for the bond-slip model simulations. The bond-slip model simulation results with different stiffness values are also compared with the perfect bond model. It has been seen that if the rigidity on the interface is taken sufficiently high for the bond-slip model simulations, the same results are obtained as in the perfect bond model simulations. The modified model is validated in the tangential direction (Figure I.D).

Subsequently, the confinement effect on the bond properties are investigated. After a detailed analysis of the literature, a formulation is proposed to modify the adhesion law under lateral pressure. The formulations are implemented into the bond-slip model in a proper way. Afterwards, the new bond-slip model is tested on a single interface element for monotonic and alternative loading cases under various lateral pressures. Moreover, constant and increasing lateral compression and tension values are tested on the single interface element. The results have shown that the modification of the bond law provided correctly within the model. Thus, irreversible bond behavior under external pressure is correctly represented with the new bond-slip model.

Onwards, several experimental pull-out test are numerically performed in order to validate the new bond-slip model. Different embedment lengths, concrete covers, steel diameters, lateral pressures, adhesion laws, material properties (steel and concrete) and bond strength (strong and weak) are tested numerically in order to validate the new bond-slip model. Coherent results are obtained between the simulations and the experiments for both test cases. The implemented active confinement formulas are validated.

Later on, the new bond-slip model is used to examine the active confinement effect on the structural behavior by performing a series of numerical analysis on a tie-rod for monotonic and alternative loading. Moreover, the results are compared with the perfect bond assumption for 1D and 3D steel representations in order to see the significance of the model. According to the results, force drops are observed in the force-displacement curve with the bond-slip model simulations at instants of crack occurrence where this cannot be seen with the other simulations. In bond-slip model simulations, the damage is relatively more concentrated on the crack locations. Thus, the position of cracks can be more clearly identify from slip between steel and concrete when it changes its sign. Less slip is observed for increasing lateral pressure due to the increasing bond strength for both monotonic and cyclic cases. Moreover, the new bond-slip model enables to observe the active confinement effect on the crack closure under alternative loads. The active confinement effect on the reinforced concrete structures through the steel-concrete interface can be observed for monotonic and cyclic loading cases when the new bond-slip model is used (Figure I.E).

In the last step, the shear behavior of the reinforced concrete structures is investigated with the new bond-slip model specifically focusing on the dowel action phenomenon. The experimental campaigns of a push-off test and a four-point bending test are reproduced with the bond-slip model and the perfect bond model. Two types of reinforcement representations are used (truss and beam element) within the numerical analysis.

According to the numerical analysis performed on L shape beams (push off tests), the following conclusions may be drawn:

- The initial bond-slip model was used only with truss element steel in the previous numerical analysis of (Torre-Casanova 2013) and (Mang 2016). With this study, the new bond-slip model is used successfully with the beam element steel representation.

- Dowel action does exist and can be represented numerically when the proper reinforcement model is used (beam element).
- Concrete mesh density affects the accuracy of the numerical results for the dowel action analysis. Since dowel action occurs in very limited space compared to the whole geometry after crack opening, a smaller mesh density represents the mechanical behavior of the area better. Defining explicit nodes for steel between the two sides of a crack may represents the mechanical behavior of the cracked area in a more proper way.
- Truss element steel representation fails to reproduce the mechanical behavior of reinforced concrete under shear loading correctly after crack opened a certain amount (where dowel action occurs). Namely, it has been concluded that the truss element approach is not adequate to represent the pure dowel action behavior since it does not consider the bending of the steel bar.
- The beam element approach on the reinforcement gives convenient results compared to the truss element ones. It is necessary to use beam element approach in numerical applications to represent the pure dowel action.

According to the numerical analysis performed on continuous deep beams (four-point bending tests), the following conclusions may be drawn:

- A premature shear crack is observed for the perfect bond simulations compared to the experimental results.
- After the shear crack occurrence only the bond-slip model simulation can reproduce the experimental observations on global and local scales. This may be originated from the relaxation of the stresses due the slip between the steel and the concrete. The new bond-slip model is successful to capture the pre-peak behavior under shear load.
- The use of beam element still is necessary for the correct representation of shear behavior. Even with the bond-slip model simulations, less slip is observed for the truss element representation compared to beam element representation.

In both numerical analysis, an extreme dependence is observed on the initial conditions of:

- Mesh density,
- Concrete damage model,
- Symmetry properties,

- Location of the applied force,
- Blockage methodology of the supports,
- Material properties of steel and concrete,
- The layout of reinforcement and the supports.

In short, it can be concluded that the new bond-slip model represents global (force-displacement relation) and local behavior (crack pattern) of the reinforced concrete structures under shear loading better than the perfect bond assumption model (Figure I.F).

Even if the developed model seems to produce appropriate results, several points may need to be investigated deeper to improve the current model:

- Further investigation of the normal directional interface behavior might be useful to capture the post-peak behavior of the reinforced concrete structures in order to represent pure dowel action within the model.
- The implemented new irreversible bond-slip model is tested for laboratory scale simulations (Tie-rod). The application of the model is thus needed for the industrial scale simulations to evaluate the model's efficiency and its effect on local and global structural behavior for cyclic loads.
- In this phase, the effect of confinement on the bond properties can be observed realistically. On the other hand, the effect on the global structural behavior is not extremely significant according to the performed numerical tests. A further analysis may need to be performed with comparing different types of experimental campaigns to clarify the confinement effect on the global structural behavior.
- The concrete cover is considered for the active confinement effect on the bond behavior within the new bond-slip model. On the other hand the consideration of the passive confinement itself for the ribbed bars within the model might be useful to capture the whole confinement behavior (active and passive).
- The new bond-slip model is producing convenient results in accordance with the truss and beam element steel models. It may be useful to modify the model to be able to use on the 3D steel representation.
- Further large scale simulations are still necessary to completely generalize the model for real scale industrial applications.

References

Abed, F., H. El-Chabib, and M. AlHamaydeh. 2012. "Shear characteristics of GFRP-reinforced concrete deep beams without web reinforcement." *Journal of Reinforced Plastics and Composites* 31 (16): 1063–1073.

Abrams, Duff A. 1913. *Tests of bond between concrete and steel.* Technical, Urbana/Illinois: Bulletin No. 71 - Engineering Experimental Station University of Illinois.

Adhikary, Satadru Das , Bing Li, and Kazunori Fujikake. 2013. "Strength and behavior in shear of reinforced concrete deep beams under dynamic loading conditions." *Nuclear Engineering and Design* 259: 14-28.

Al-Nahlawi, Khaled A. , and James K. Wight. 1992. "Beam Analysis Using Concrete Tensile Strength in Truss Models." *ACI Structural Journal* May-June: 284-289.

Ashour, Ashraf. 1997. "Tests of Reinforced Concrete Continuous Deep Beams." *ACI Structural Journal* 94 (S01).

Baktheer, A., and R. Chudoba. 2018. "Modeling of bond fatigue in reinforced concrete based on cumulative measure of slip." *Computational Modeling of Concrete Structures: EURO-C* (CRC Taylor & Francais Group) (ISBN 978-1-138-74117-1:): 767-776.

Baumann, Theodor, and Hubert Rüsch. 1970. *Schubversuche mit indirekter Krafteinleitung : Versuche zum Studium der Verdübelungswirkung der Biegezugbewehrung eines Stahlbetonbalkens.* Technical, Berlin/Germany: Heft / Deutscher Ausschuss für Stahlbeton Vol: 210.

Bazant, Z. P. 1984. "Size effect in blunt fracture: Concrete, rock and metal." *ASCE Journal Engineering Mechanics* 110: 518-535.

Bazant, Zdanek P., and M. C. Burrow. 1980. "Confinement effect in flexural ductilty of concrete: three-dimensional analysis." *Materials and Structures* 13: 296-308.

Brisotto, D. S., E. Bittencourt, and V. M. R. Bessa. 2012. "Simulating bond failure reinforced concrete by a plasticity model." *Computers and Structures* 106-107: 81-90.

Casanova, Anaelle, Ludovic Jason, and Luc Davenne. 2012. "Bond slip model for simulation of reinforced concrete structures." *Engineering Structures* (Engineering Structures) 39 (66-78): 66-78.

Cast3M. 2017. *http://www-cast3m.cea.fr/index.php.*

Clément, Jean Luc. 1987. *Interface acier - béton et comportement des structures en béton-armé :*. Technical, Paris/France: Thèse de l'Université Paris 6.

Codcogs. 2016. *http://www.codecogs.com/library/engineering/materials/plastic-theory-of-bending.php.*

Costa, C., P. Pegon, A. Arêde, and J. Castro. 2004. *Inplementation of the damage model in tension and compression with plasticity in Cast3M.* Technical, JRC report.

Daoud, A. 2003. *Etude expérimentale de la liaison entre l'acier et le béton autoplçant - contribution à la modélisation numérique de l'interface.* Technical, Toulouse France: Thèse de l'INSA de Toulouse.

Darwin, D., J. Zuo, M. L. Tholen, and E. K. Idun. 1996. "Development Length Criteria for Conventional and High Relative Rib Area Reinforcing Bars." *ACI Structural Journal* 93(3): 347-369.

De Nardin, Silvana , and Ana Lucia H. C. El Debs. 2007. "Shear transfer mechanisms in composite columns: An experimental study." *Steel and Composite Structures* 7 (5): 377-390.

Dehghani, E., F. Daneshjoo, A. A. Aghakouchak, and N. Khaji. 2012. "A new bond-slip model for adhesive in CFRP–steel composite systems." *Engineering Structures* 34: 447–454.

Dominguez, N., D. Brancherie, L. Davenne, and A. Ibrahimbegovic. 2005. "Prediction of crack pattern distribution in reinforced concrete by coupling a strong discontinuity model of concrete cracking and a bond slip of reinforcement model." *Engineering Computations* 22: 558-582.

Dulacska, Helen. 1972. *Dowel Action of Reinforcement Crossing Cracks in Concrete.* Technical, Journal Proceedings, Volume: 69, Issue: 12.

El-Ariss, Bilal. 2007. "Behavior of beams with dowel action." *Engineering Structures* 29: 899-903.

Eligehausen, R., E. P. Popov, and V. V. Bertero. 1983. *Local bond stress-slip relationship of deformed bars under generalized excitations.* Technical, Berkeley CA.: Earthquake Engineering Research Center.

Esfahani, M. Reza, and B. Vijaya Rangan. 2000. "Infuence of transverse reinforcement on bond strength of tensile splices." *Cement & Concrete Composites* 22: 159-163.

Eurocode 2. 2007. *Eurocode 2.* NF-EN-1992: Calcul des Structures en béton.

Fawzia, Sabrina, Xiao-Ling Zhao, and Riadh Al-Mahaidi. 2010. "Bond–slip models for double strap joints strengthened by CFRP." *Composite Structures* 92: 2137–2145.

Flippou, F. C., E. P. Popov, and V. V. Bertero. 1983. *Effects of bond deterioration on hysteretic behavior of reinforced concrete joints.* Technical Report, California/Berkeley: EARTHQUAKE ENGINEERING RESEARCH CENTER / REPORT NO: UCB/EERC-83/19.

Frantzeskakis, C., and J. N. Theillout. 1989. "Nonlinear finite element analysis of reinforced concrete structures with a particular stategy following the cracking process." *Computers & Structures* 31: 395-412.

Galvez, J. C., J. M. Benitez, B. Tork, M. J. Casati, and D. A. Cendon. 2009. "Splitting failure of precast prestressed concrete during the release of the prestressing force." *Engineering Failure Analysis* 16: 2618-2634.

Gambarova, P. G., G.P. Rosati, and B. Zasso. 1989. "Steel-to-concrete bond after concrete splitting: Test Results." *Materials and Structures* 22: 35-47.

Gan, Youai. 2000. *Bond stress and slip modeling in nonlinear finite element analysis of reinforced concrete structures.* Technical, Toronto/Canada: Thesis - Department of Civil Engineering - University of Toronto.

Giry, Cédric , Frédéric Dufour, and Jacky Mazars. 2011. "Stress-based nonlocal damage model." *International Journal of Solids and Structures* 48: 3431–3443.

Grassl, Peter, Morgan Johansson, and Joosef Leppanen. 2018. "On the Numerical Modelling of Bond for the Failure Analysis of Reinforced Concrete." *Engineering Fracture Mechanics* (Engineering Fracture Mechanics) 189 (13–26): Vol-189: 13–26.

Hadi, Muhammad N. S. 2008. "Bond of High Strength Concrete with High Strength Reinforcing Steel." *Open Civil Engineering* (The Open Civil Engineering Journal) 2 (143-147): 08(2):143-7.

Hassan, A.A.A., K.M.A. Hossain, and M. Lachemi. 2010. "Strength, cracking and deflection performance of large-scale self-consolidating concrete beams subjected to shear failure." *Engineering Structures* 32.

He, Jun, and Guijun Xian. 2017. "Bond-slip behavior of fiber reinforced polymer strips-steel interface." *Construction and Building Materials* 155: 250-258.

He, X.G., and A.K.H. Kwan. 2001. "Modeling Dowel Action of Reinforcement Bars for Finite Element Analysis of Concrete Structures." *Computers and Structures* 79: 595-604.

Hillerborg, Arne. 1983. "Analysis of one single crack." *Fracture Mechanics of Concrete* 223-249.

Houde, J., and M. S. A. Mirza. 1974. "A finite element analysis of shear strength of reinforced concrete beams." *ACI Special Publication* 42 (1): 103-128.

Husain, Husain M., Nazar K. Oukaili, and Hakim S. Muhammed. 2009. "Dowel action between two concretes." *Journal of Engineering* (2) 15: 3583-3605.

Ince, Ragip, Erhan Yalcin, and Abdulsamet Arslan. 2007. "Size-dependent response of the dowel action in RC members." *Engineering Structures* (Engineering Structures) 29 (955-961): (29) 955–961.

Ince, Ragip, Erhan Yalcin, ve Abdulsamet Arslan. 2003. *Betonarme Kirislerde Pecin Etkisinde Boyut Tesirinin Fraktal Modeli.* Technical, Gaziantep/Turkey: XIII. Ulusal Mekanik Kongresi.

Jelic, I., M. N. Pavlovic, and M. D. Kotsovos. 1999. "A study of dowel action in reinforced concrete beams." *Concrete Research* 51(2): 131-141.

Jendele, Libor, and Jan Cervenka. 2006. "Finite element modelling of reinforcement with bond." *Computers and Structures* 84: 1780–1791.

Jin, Liu, Dong Li, and Xiuli Du. 2016. "Mechanical behavior and size effect of moderate high-strength RC colums under monotonic and cyclic axial compression." *Engineering Structures* 124: 269-285.

Johansson, M. 2003. "Composite action in connection regions of concrete filled steel tube columns." *Steel and Composite Structures* 3(1): 47-64.

Júlio, E.N.B.S., D. Dias-da-Costa , F.A.B. Branco, and J.M.V. Alfaiate. 2010. "Accuracy of design code expressions for estimating longitudinal shear strength of strengthening concrete overlays." (Engineering Structures) 32 (2387-2393).

Karatas, M., K. Turk, and Z. C. Ulucan. 2010. "Investigation of bond between lap-spliced steel bar and self-compacting concrete: The role of silica fume." *Canadian Journal of Civil Engineering* 37(3): 420-428.

Kazakoff, E. E. 1974. *Dowel action in reinforced concrete construction.* Phd Theis at Department of Civil Engineering / University of British Columbia.

Khafallah, S., and M. Ouchenane. 2007. "Numerical simulation of bond for pull-out tests: the direct problem." *Asian Journal of Civil Engineering* 8: 491-505.

Kim, J., and Y. Park. 1996. "prediction of shear strength of reinforced concrete beam without web reinforcement." *ACI Mater* 93(3): 213-222.

Kontronis, Panagiotis, and Jacky Mazars. 2005. "Simplified modelling strategies to simulate the dynamic behavior of R/C walls." *Earthquate Engineering* 9(2): 285-306.

Kwan, A. K. H., and P. L. Ng. 2012. "Modelling dowel action of discrete reinforcing bars for finite element analysis of concrete structures." *Computers and Concrete* (1) 12: 19-36.

Lee, Ji-hyung , and Sung-gul Hong. 2015. "Shear Transfer Strength Evaluation for Ultra-High Performance Fiber Reinforced Concrete." *International Conference Data Mining, Civil and Mechanical Engineering Feb. 1-2, 2015.* Bali (Indonesia).

Li, Pengda, and Yu-Fei Wu. 2016. "Stress-strain behavior of actively and passively confined concrete under cyclic axial loading." *Composite Structures* 149: 369-384.

Lim, Jian C., and Togay Ozbakkaloglu. 2014. "Stress-strain model for normal and light weight concretes under uniaxial and triaxial compression." *Construction and Building Materials* 71 (492-509): 492-509.

Lin, Hongwei, Yuxi Zhao , Joško Ozbolt, and Reinhardt Hans-Wolf. 2017. "The bond behavior between concrete and corroded steel bar under repeated loading." *Engineering Structures* (Engineering Structures) 140 (390–405): Vol-140: 390–405.

Lindorf, A., L. Lemnitzer, and M. Curbach. 2009. "Experimental investigations on bond behavior of reinforced concrete under transverse tension and repeated loading." *Engineering Structures* 31(7): 1469-1476.

Logan, D. L. 2012. *A First Course in the Finite Element Method (Fifth Edition).* Stanford California / USA: CL Engineering .

Lowes, Laura N., Jack P. Moehle, and Sanjay Govindjee. 2004. "Concrete-steel bond model for use in finite element modeling of reinforced concrete structures." *ACI Structural Journal* July-August: 501-511.

Lua, X.Z. , J.G. Teng, L.P. Yea, and J.J. Jiang. 2005. "Bond–slip models for FRP sheets/plates bonded to concrete." *Engineering Structures* 27: 920–937.

Lundgren, Karin. 2002. *Three-Dimensional Modelling of Bond in Reinforced Concrete.* Technical, Göteborg, Sweden: Ph.D. Thesis, Department of Civil Engineering, Chalmers University of Technology.

Magnusson, J. . 2000. *Bond and anchorage pf ribbed bars in high strenght concrete.* Technical, Gotebourg Sweden: Division of Concrete Structures / Chalmers Universty of Technology.

Malvar, R. J. 1991. *Bond of reinforcement under controlled confinement.* Technical, California/USA: Naval Civil Engineering Laboratory Pori Hueneme .

Mang, Chetra. 2016. *Modélisation de la liaison acier-béton dans le calcul de structures en béton armé.* PhD thesis, CEA Saclay, Saclay/France: CEA.

Mang, Chetra, Ludovic Jason, and Luc Davenne. 2015. "A new bond slip model for reinforced concrete structures validation by modelling a reinforced concrete tie." *Engineering Computations* (Engineering Computations) 32 (7) (1934-1958): 1934-1958.

Martin-Pérez, B. , and S.J. Pantazopoulou. 2001. "Effect of bond, aggregate interlock and dowel action on the shearstrength degradation of reinforced concrete." *Engineering Structures* 23: 214–227.

Mazars, Jacky. 1986. "A Description of Micro and Macroscale Damage of Concrete Structures." *Engineering Fracture Mechanics* (Engineering Fracture Mechanics) 25 (729-737): Vol. 25: 729-737.

Mazars, Jacky, F. Ragueneau , G. Casaux, A. Colombo, and P. Kotronis. 2004. "Numerical modelling for earthquake engineering: the case of lightly RC structural walls." *International Journal for Numerical and Analytical Methods in Geomechanics* 857-874.

Moretti, M., and T. P. Tassios. 2007. "Behaviour of short columns subjected to cyclic shear displacements: Experimental Results." *Engineering Structures* 29: 2018-2029.

Morita, Shiro, and Tetsuzo Kaku. 1974. *Local bond stress-slip relationship under repeated loading.* Technical, IABSE reports of the working commissions.

Navarro-Gregori, Juan, Eduardo J. Mezquida-Alcaraz, Pedro Serna-Ros, and Javier Echegaray-Oviedo. 2016. "Experimental study on the steel-fibre contribution to concrete shear behavior." *Construction and Building Materials* 112: 100–111.

Ngo, D., and A. C. Scordelis. 1967. "Finite element anaylsis of reinforced concrete beams." *ACI Journal* (ACI Journal) (TITLE NO. 64-14): TITLE NO. 64-14.

Nogueira, C. G., W. S. Venturini, and H. B. Coda. 2013. "Material and geometric nonlinear anaysis of reinforced concrete frame structures considering the influence of shear strength complementary mechanisms." *Solids and Structures* 10: 953-980.

Oliver, J., D. L. Linero, A. E. Huepse, and O. L. Manzoli. 2008. "Two dimensional modeling of material failure in reinforced concrete by means of a continuum strong discontinuity approach." *Computer Methods in Applied Mechanics and Engineering* 197: 332-348.

Orangun, C. O., J. O. Jirsa, and J. E. Breen. 1977. "The Strength of Anchored Bars:Re-evaluation of test data on development length and splices." *ACI Structural Journal* 74(3): 114-122.

Park, Robert, and Thomas Paulay. 1975. "Reinforced Concrete Structures." Book.

Rao, G. Appa , K. Pandurangan, and F. Sultana. 2007. "Studies on the pull out strength of ribbed bars in high strength concrete." *Proc. of FraMCoS-6* 1: 295-301.

Reinhardt, H. W. , J. Blaauwendraad, and E. Vos. 1984. "Prediction of bond between steel and concrete by numerical analysis." *Matrriaux and Constructions* 17: 311-320.

Rezazadeh, Mohammadali, Valter Carvelli, and Ana Veljkovic. 2017. "Modelling bond of GFRP rebar and concrete." *Construction and Building Materials* 153: 102–116.

Robins, P. J., and I. G. Standish. 1982. *The effect of lateral pressure on the bond of round reinforcing bars in concrete.* Technic, Loughborough University England: Internal Journal of Adhesion and Adhesives.

Sagaseta, J., and R. L. Vollum. 2011. "Influence of aggregate fracture on shear transfer through cracks in reinforced concrete." *Magazine of Concrete Research* 63(2): 119–137.

Santos, José, and António Abel Henriques. 2015. "New finite element to model bond–slip with steel strain effect for the analysis of reinforced concrete structures." *Engineering Structures* 86: 72–83.

Sanz, B., and J. Planas. 2018. "Simulation of interface behavior between steel and concrete to study loss of bond due to reinforcement corosion." *Conference Paper: EURO-C Computational Modeling of Concrete and Concrete Structures* (Taylor & Francis Group London) (ISBN-978-1-138-74177-1).

Sanz, B., J. Planas, and J. M. Sancho. 2013. "An experimental and numerical study of the pattern of cracking of concrete due to steel reinforcement corrosion." *Engineering Fracture Mechanics* 114: 26–41.

Shang, H., F. Cui, P. Zhang, T. Zhao, and G. Ren. 2017. "Bond behavior of steel bar embedded in recycled coarse aggrate concrete under lateral compression load." *Construction and Building Materials* 150: 529-537.

Slater, W. A., F. E. Richart, and G. G. Scofield. 1920. *Test of bond resistance between concrete and steel.* Technical, Washington DC, USA: Tecnologic Papers of the Bureau of Standarts.

Soroushian, P., K. Obaseki, M. C. Royjas, and J. Sim. 1986. "Analysis of dowel bars acting against concrete core." *ACI Journal* 83(4): 642-689.

Sorousian, P. 1987. "Behavior of the bars in dowel action against concrete cover." *ACI Structural Journal* 84(2): 170-6.

Soylev, Tayfun A., and Raoul François. 2005. "Effects of bar-placement conditions on steel-concrete bond." *Materials and Structures* 39: 211-220.

Sulaiman, Muhd Fauzy , Faisal Amsyar Redzuan, Chau Khun Ma, Abdullah Zawawi Awang, and Wahid Omar. 2017. "Bond Between SSTT Confined Concrete and Ribbed Steel Reinforcement Bar." *Transactions on Science and Technology* 4 (3): 194 - 201.

Sulaiman, Muhd Fauzy, Chau-Khun Ma, Nazirah Mohd Apadi, Sofrie Chin, Abdullah Zawawi Awang, Saiful Amri Mansur, and Wahid Omar. 2017. "Review on Bond and Anchorage of Confined High-strength Concrete." *Structures* 11: 97-109.

Tepfers, Ralejs. 1973. *A theory of bond applied to overlapped tensile reinforcement splicesfor deformed bars.* Technical, Goteborg/Sweden: Division of Concrete Structures, Chalmers University of Technology.

Torre-Casanova, Anaelle. 2013. *Prise en Compte de la Liaison Acier-Béton pour le Calcul de Structures Industrrielles.* PhD Thesis, CEA Saclay, Saclay/France: CEA.

Torre-Casanova, Anaelle, Ludovic Jason, Luc Davenne, and X Pinelli. 2013. "Confinement effects on the steel-concrete bond strength and pull-out failure." *Engineering Fracture Mechanics* 97: 92-104.

Tudjono, Sri , Aditya Sage Pamungkas, and Ay Lie Han. 2014. "Modelling the relationship of the flexural rigidity factor and reinforcement ratio by numerical simulation." *Procedia Engineering* 95: 241 – 251.

Uijl, Joop den, and Agnieszka Bigaj-van Vliet. 1996. "A bond model for ribbed bars based on concrete confinement." (Heron) 41 (3).

Venderame, G., P. Ricci, G. De Carlo, and G. Manfredi. 2009. "Cyclic bond behavior of of plain bars. I: Experimental investigation." *Construction Building Materials* 23(12): 3499-3511.

Verderame, G. M., G. De Carlo, P. Ricci, and G. Fabroccino. 2009. "Cyclic bond behavior of of plain bars. II: Analytical Investigation." *Constrating Building Materials* 23(12): 3412-3522.

Vintzeleou, E. N., and T. P. Tassios. 1987. "Behavior of dowels under cyclic deformations." *ACI Structural Journal* 84 (1): 18-30.

Viwathanatepa , S., P. Popov, and V. V. Bertero. 1979. *Effects of generalized loadings on bond of reinfocing bars embedded in confined concrete blocks.* Technical, California/Berkeley: Earthquake Engineering Research Center UCB/EERC-79/22.

Walraven, J. C. , and H. W. Reinhardt. 1981. *Theory and experiments on the mechanical behavior of cracks in plain and reinforced concrete subjected to shear loading.* Technical Report, Delft/Netherlands: HERON Vol. 26 No:1.

Wang, Hai-Tao , and Gang Wu. 2018. "Bond-slip models for CFRP plates externally bonded to steel substrates." *Composite Structures* 184: 1204–1214.

Wu, Zhimin, Xue Zhang, Yu Hu, and Qingbin Li. 2014. "Bond Behavior of plain round bars embedded in concrete subjected to biaxial lateral tensile-compressive stresses." *Structural Engineering* 140(4) (04013089): 140(4): 04013089.

Xia, Jun, Yulin Xiao, Kevin R. Mackie, Munaf Al-Ramahee, and Amir Mirmiran. 2015. "Dowel action and shear strenght contribution of high strength rebar embedded in ultra-high performance fiber reinforced concrete." *Engineering Structures* 83: 223-232.

Xia, S.H. , and J.G. Teng. 2005. "Behavior of FRP-to-steel bonded joints." *Proceedings of the International Symposium on Bond Behaviour of FRP in Structures.* Hong Kong, China: International Institute for FRP in Construction.

Xiao, Jianzhuang, Zhiwei Li, and Jiabin Li. 2014. "Shear transfer across a crack in high-strength concrete after elevated temperatures." *Construction and Building Materials* 71: 472–483.

Xu, Feng, Wu Zhimin, Jianjun Zheng, Yu Hu, and Qingbin Li. 2012. "Experimental study on the bond behavior of reinforcing bars in concrete subjected to lateral pressure." *Metarials in Civil Engineering* 24(1): 125-133.

Xu, Feng, Zhi-min Wu, Jian-jun Zheng, Yu Hu, and Quing-bin Li. 2014. "Bond behavior of plain round bars in concrete under complex lateral pressures." *ACI Structural Journal* 111-S02 (1): Title No. 111-S02.

Xu, Tengfei, Arnaud Castel, R. Ian Gilbert, and Angus Murray. 2016. "Modeling the tensile steel reinforcement strain in RC-beams subjected to cycles of loading and unloading." *Engineering Structures* 126: 92-105.

Yang, H, Z Deng, Y Qin, and Y Lv. 2015. "A Study on the Bond Behavior of Corroded Reinforced Concrete Containing Recycled Aggragetes." *Advence in Materials Science and Engineering.*

Yao, J., and J. G. Teng. 2007. "Plate end debonding in FRP-plated RC beams—I: Experiments." *Engineering Structures* 29: 2457-2471.

Yong, Y. K., M. G. Nour, and E. G. Nawy. 1988. "Behavior of Laterally Confined High-Strength Concrete under Axial Loads." *Engineering Structrues* 114(2): 332-51.

Zhang, Ning , and Kang-Hai Tan. 2007. "Size effect in RC deep beams Experimental investigation and STM verification." *Engineering Structures* 29: 3241–3254.

Zhang, Xue, Wei Dong, Jian-jun Zheng, Zhimin Wu, Yu Hu, and Qing-bin Li. 2014. "Bond behavior of plain round bars embedded in concrete subjected to lateral tension." *Construction and Building Materials* 54: 17-26.

Zhang, Xue, Zhimin Wu, Jianjun Zheng, Wei Dong, and Abdelhamid Bouchair. 2016. "Ultimate bond strength of plain round bars embedded in concrete supjected to uniform lateral tension." *Construction and Building Materials* 117: 163-170.